

Structural and Functional Studies of Proteins in the Class Ib Ribonucleotide Reductase System

Thesis for the degree of *Philosophiae Doctor*

By

Marta Hammerstad



Department of Biosciences

The Faculty of Mathematics and Natural Sciences

University of Oslo

Norway

2014

© **Marta Hammerstad, 2014**

*Series of dissertations submitted to the
Faculty of Mathematics and Natural Sciences, University of Oslo
No. 1527*

ISSN 1501-7710

All rights reserved. No part of this publication may be reproduced or transmitted, in any form or by any means, without permission.

Cover: Inger Sandved Anfinsen.
Printed in Norway: AIT Oslo AS.

Produced in co-operation with Akademia Publishing.
The thesis is produced by Akademia Publishing merely in connection with the thesis defence. Kindly direct all inquiries regarding the thesis to the copyright holder or the unit which grants the doctorate.

TABLE OF CONTENTS

ACKNOWLEDGEMENTS	I
ABBREVIATIONS	III
LIST OF PAPERS	V
INTRODUCTION	1
Metal ions and redox chemistry in biology	1
Ribonucleotide reductase	4
Classification of RNRs.....	5
Class I RNRs	7
The class Ib RNR system	12
Radical transfer from R2 to R1	15
Thioredoxin	17
Thiol-redox diversity.....	17
The thioredoxin-like fold and active site motif.....	19
Mechanism of electron transfer in thioredoxin	20
AIMS OF STUDY	25
SYMMARY OF PAPERS	27
MY CONTRIBUTIONS TO PAPERS I-III	31
DISCUSSION	33
A short introduction to biophysical techniques	34
X-ray protein crystallography	34
Electron paramagnetic resonance spectroscopy	35
Resonance Raman spectroscopy	36

The RNR class Ib R2F subunit	37
<i>M. tuberculosis</i> has two active R2F subunits	38
Spectroscopic characterization of R2F-1	38
<i>B. cereus</i> NrdF and the NrdI-NrdF crystal complex	40
Flexibility of the metal ion coordination environment	42
Assembly of the class Ib holoenzyme.....	43
<i>B. cereus</i> BC3987 – a small thioredoxin	45
Cysteine p <i>K</i> _a values can be adjusted through hydrogen bonding	45
FUTURE PERSPECTIVES	49
REFERENCES	51

ACKNOWLEDGEMENTS

The work presented in this thesis was carried out from 2010 to 2014 at the Department of Biosciences (previously Department of Molecular Biosciences), University of Oslo, as part of a four-year position including 25% teaching. The position was financially supported by a *Ph. D.* fellowship from the University of Oslo.

First and foremost, I would like to thank my main supervisor, Prof. K. Kristoffer Andersson, for giving me the opportunity to perform my *Ph. D.* studies in his research group. In addition to introducing me to the field of ribonucleotide reductase, I would like to thank you for your encouragement, support, discussions and for always taking the time to help and advise me. Also, I highly appreciate your love to the field and your wanderlust, giving me the chance to attend courses and conferences around the world.

I would also like to thank my co-supervisors in the metalloprotein group, Hans-Petter Hersleth and Åsmund K. Røhr. Thank you for the enormous amount of support and guidance you have given me. You have both been my life-savers in several occasions. Hans-Petter – thanks for putting up with all my questions and being a helpful and wonderful office-mate. There are no boring days at work when you are around.

In addition, I am thankful to all the resulting present and former members of the metalloprotein group, and my colleagues at the department for creating a friendly, inspiring and fun atmosphere. In particular, I would like to thank Marie (for all our M&M moments), Niels, Giorgio, Espen, Ane, Inger, Camilla, and Bie.

Thanks to Bjørn for letting me use equipment at Rikshospitalet, and for your assistance.

Furthermore, I would like to thank Prof. Martin Högbom and Prof. Astrid Gräslund for giving me the opportunity to stay six months in your laboratories at Stockholm University. My stay in Stockholm at the Department of Biochemistry and Biophysics was an educational and exiting period, making great impact on my work and scientific experience. I am grateful to all the incredible people I got to know in your laboratories, as well as the resulting people in the C4-corridor, for all our discussions during the “fika” breaks, and for making me feel like home. Thanks to MLS^{UiO} and the National graduate school in structural biology, BioStruct, for the financial support allowing me to stay in Stockholm.

Finally, I would like to thank all my dear friends within and outside the academia for all your support and for bringing so much joy into my life. Above all, I would like to express my deepest gratitude to my family and my parents, especially Mamuš and Kjell, my father Aasmund, and my brother Erik, for their love and constant support throughout the years. Last, but not least, thank you Jo Annar, for continuously distracting me from my work, for making me laugh and for all your love. You are amazing.

Marta Hammerstad

Oslo, April 2014

ABBREVIATIONS

AdoMet/SAM	S-adenosyl methionine
α_2	RNR large subunit, homodimeric
β_2	RNR small subunit, homodimeric
dNDP	Deoxyribonucleotide diphosphate
dNTP	Deoxyribonucleotide triphosphate
EPR	Electron paramagnetic resonance
FAD	Flavin adenine dinucleotide
FMN	Flavin mononucleotide
Gor	Glutathione reductase
Grx	Glutaredoxin
GSH	Glutathione
HF-EPR	High field/high frequency EPR
ITC	Isothermal titration calorimetry
NADH	Nicotinamide adenine dinucleotide
NADPH	Nicotinamide adenine dinucleotide phosphate
NrdA/R1	Class Ia RNR large subunit
NrdB/R2	Class Ia RNR small subunit
NrdE/R1E	Class Ib RNR large subunit
NrdF/R2F	Class Ib RNR small subunit
PDB	Protein data bank
PDI	Protein disulfide isomerase
QM/MM	Quantum mechanics/molecular mechanics
rRaman	Resonance Raman
S•	Thiyl radical
Trx	Thioredoxin
TrxR	Thioredoxin reductase
Y•	Tyrosyl radical
Å	Ångström (10^{-10} meters)

LIST OF PAPERS

This thesis is based on the following Papers I-III, which will be referred to in the text by their Roman numerals:

- I. Hammerstad, M., Røhr, Å. K., Andersen, N. H., Gräslund, A., Högbom, M., and Andersson, K. K. (2014) The class Ib ribonucleotide reductase from *Mycobacterium tuberculosis* has two active R2F subunits. *J. Biol. Inorg. Chem.* DOI: 10.1007/s00775-014-1121-x
- II. Hammerstad, M., Hersleth, H. -P., Tomter, A. B., Røhr, Å. K., and Andersson, K. K. (2014) Crystal structure of *Bacillus cereus* class Ib ribonucleotide reductase diron NrdF in complex with NrdI. *ACS Chem. Biol.* **9** (2), 526–537
- III. Røhr, Å. K., Hammerstad, M., and Andersson, K. K. (2013) Tuning of thioredoxin redox properties by intramolecular hydrogen bonds. *PLoS One* **8** (7), e69411

Papers not included in thesis:

Tomter, A. B., Zoppellaro, G., Andersen, N. H., Hersleth, H. -P., Hammerstad, M., Røhr, Å. K., Sandvik, G. K., Strand, K. R., Nilsson, G. E., Bell, C. B., Barra, A. L., Blasco, E., Le Pape, L., Solomon E. I., and Andersson, K. K. (2013) Ribonucleotide reductase class I with different radical generating clusters. *Coord. Chem. Rev.* **257**, 3-26

Skråmo, S., Hersleth, H. -P., Hammerstad, M., Andersson, K. K., and Røhr, Å. K. (2014) Cloning, expression, purification, crystallisation and preliminary X-Ray diffraction analysis of a ferredoxin/ flavodoxin-NADP(H) oxidoreductase (Bc0385) from *Bacillus cereus*. *Acta Crystallogr. Sect. F Struct. Biol. Cryst. Commun.* **70** (6), 777-780

INTRODUCTION

All organisms rely on electron transport to facilitate molecular transformations and for fundamental processes essential for life. Proteins involved in reduction-oxidation (redox) reactions generally contain redox active cofactors such as metal ions, hemes, flavins, disulfides, iron-sulfur (Fe-S) clusters or NADPH, which are all used in electron transfer reactions. Combined biochemical and biophysical approaches are important and widely used to understand these fascinating mechanisms.

Metal ions and redox chemistry in biology

The importance of inorganic compounds and metal ions in biological processes is indisputable. Metal ions play a central role in many challenging chemical reactions and in energy metabolism (1). It is estimated that 30-50% of all proteins require the presence of metal ions for their biological activity (2). Metalloproteins utilize metal ions as structural features, for fast information transfer, participation in catalysis by orienting substrates for reactions, functioning as Lewis acids in formation, degradation and metabolism of organic compounds, in signaling pathways, and in redox reactions (3). Several important biocatalytic processes, such as nitrogen fixation, methane biogenesis and oxidation, oxygen storage, and formation, utilization and degradation of metabolites, involve the presence of metalloenzymes. Many proteins coordinate the metal ions directly through charged or polar side chains, while others contain metals covalently incorporated in prosthetic groups, such as the protoporphyrins in heme proteins, and Fe-S clusters in Fe-S proteins. The metal ions included in the protein scaffold are cations characterized by different oxidation states, as well as experiencing different coordination environments. Transition metals, such as iron, manganese and copper are often found in the active site of enzymes that activate or transport oxygen (4). Molecular oxygen plays a key role in many important biological processes. The ground state of molecular oxygen is the relatively unreactive triplet state ($S=1$) with two unpaired electrons. This makes spontaneous reactions between carbon compounds and molecular oxygen kinetically slow. To overcome this restriction, many proteins make use of transition metal ions, radicals, or organic

cofactors to activate oxygen. Transition metals, for example, are not limited to one spin state, and may accept or donate electrons involved in the reaction, enabling enzymes to catalyze their reaction by converting oxygen to reactive states, through rearrangement of electrons in the partially filled transition metal ions d-orbitals (5,6). As an example, some classes of ribonucleotide reductase (RNR) proteins use their metallocofactor to activate oxygen and generate a stable radical on a nearby tyrosine residue.

Iron is one of the most abundant and versatile metals found in proteins, and it is present throughout most living systems. It may be assembled into heme proteins, iron-sulfur clusters or non-heme mono- or dinuclear cofactors. In heme proteins, iron functions in storage and transport of oxygen, as in myoglobin and hemoglobin, respectively; in cytochromes as electron carriers (7); in heme-containing dioxygenases, involved in tryptophan regulation (8); in heme monooxygenases, incorporating a hydroxyl group into substrates, or in heme peroxidases, where the heme group participates in the oxidation of different substrates, e.g. cytochrome c peroxidase where also a Trp radical is generated (9). Additionally, iron is an important detoxifying agent in catalase and superoxide dismutase. Non-heme diiron carboxylate/iron-oxygen proteins catalyze a wide range of redox reactions (10,11). Some members of this family of proteins are the radical-forming R2 subunits of ribonucleotide reductases (RNRs) (see below) (12), methane monooxygenase hydroxylase (13), and iron storage proteins, such as ferritins (14).

Iron has the ability to exist in several oxidation states, mainly Fe^{II} (ferrous iron) and Fe^{III} (ferric iron) in biology, but also as $\text{Fe}^{\text{IV}}=\text{O}$ (ferryl). In reactions catalyzed by iron-containing enzymes, iron normally undergoes changes in oxidation state during the catalytic cycle (15). Another important transition metal able to reach the same oxidation states as iron, manganese, is also used by several metalloenzymes, such as the oxygen-evolving complex in photosystem II (16). The ability to incorporate different metallocofactors has also been shown to be widespread in some enzymes, such as in two RNR subclasses (Figure 1), where one subclass can utilize either a dinuclear iron- or manganese cofactor (17,18), while another subclass has been found to use a heterodinuclear iron-manganese cofactor (19,20).

Metalloprotein redox chemistry is crucial in a wide variety of enzymes throughout nature. However, electron transfer through redox centers that do not contain metal ions is also an important part of redox transitions in cells. These redox centers can also be linked to metallocofactors in redox networks. This includes organic coenzymes such as flavin -

and nicotinamide coenzymes, tetrahydrobiopterins, chlorophylls, vitamin B₁₂ coenzymes, S-adenosyl methionine (AdoMet or SAM), as well as thiol-disulfide exchanging enzymes, which all play crucial roles in various redox reactions (21).

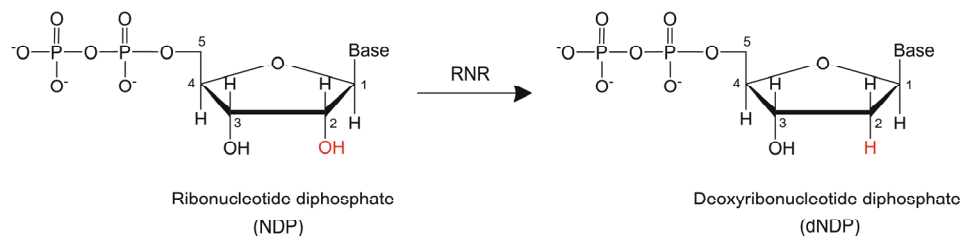
The cofactor of flavoproteins is derived from riboflavin, consisting of an isoalloxazine ring system serving in reversible electron transfer. Flavoproteins are capable of both one- and two-electron transfer processes, catalyzing a versatility of reactions, such as reduction of hydroperoxides, hydroxylation of aromatic compounds, participation in light-initiated reactions as well as in programmed cell death (22). While some protein-bound flavins serve as unspecific electron donors in several redox pathways, certain flavoproteins participate in distinct pathways, such as the flavin mononucleotide cofactor (FMN) containing flavodoxin NrdI, which has been suggested to serve as a specific electron donor for the class Ib RNR small subunit (23). The large Complex I of the electron-transport chain in the inner mitochondrial membrane is an example of a system utilizing several redox centers. Complex I passes electrons in a multistep path from the nicotinamide coenzyme NADH to ubiquinone, through a FMN cofactor and a series of Fe-S clusters (21,24). Thioredoxin reductase (TrxR) is another example of a system containing multiple redox centers. This dimeric flavoenzyme containing a flavin adenine dinucleotide (FAD) cofactor catalyzes the NADPH-dependent reduction of thioredoxins (Trxs) through a reversible thiol-disulfide exchange reaction (25). Trx-like proteins are required as hydrogen atom donors for the active site in the catalytic subunit of RNR (26,27).

Ribonucleotide reductase

Even though RNRs have been studied elaborately and extensively for many decades, more detailed electronic and structural knowledge regarding the metal binding site is still needed. A deeper understanding of the structures and interaction pathways among the different proteins involved in the RNR system would also provide important functional insight in the nature of this fascinating enzyme.

The reduction of ribonucleotides to deoxyribonucleotides was first suggested by Jean Brachet in 1933 (28). However, the first evidence for this reaction performed through isotope experiments, emerged almost 20 years later by Peter Reichard and co-workers (29). These findings led Reichard to the initial discovery of RNR (30,31), and opened an exciting and fascinating field of research (32) for molecular biologists, biochemists and biophysicists, which has now lasted for more than 50 years.

RNRs catalyze the reduction of ribonucleotides to their corresponding deoxynucleoside 5'-di- or triphosphates (dNDPs or dNTPs) (33,34) (Scheme 1).



Scheme 1. The reduction of ribonucleotides to their corresponding deoxyribonucleotides by RNR.

This enzyme plays an important role in nucleotide metabolism, being responsible for the *de novo* synthesis of all four DNA precursors, hence being crucial in all DNA-based living organisms. The proposed reaction of ribonucleotide reduction, explained with a reaction mechanism involving an active site thiyl radical (S^\bullet) being responsible for hydrogen abstraction (35), where one carbon bound hydroxyl group of ribose could be directly replaced by a hydrogen atom, was first discovered in RNR. All RNRs share a common catalytic mechanism involving the activation of a ribonucleotide by abstraction of the 3'-hydrogen atom of ribose by a transient S^\bullet in the catalytic subunit, leading to the exchange

of the hydroxyl group on the 2'-carbon of the ribose ring with a hydrogen atom (36). RNRs are divided into three main classes, differing in how they generate the S•, and are discussed in more detail below. An overview of the current perception of all RNR classes, including substrates, radical initiators, and *in vivo* reductants is shown in Figure 1. The RNR system involves a fascinating variety of interacting proteins and redox cofactors, such as non-heme diiron proteins, thiol-disulfide oxidoreductases, flavoproteins, NADPH-dependent proteins, AdoMet, a vitamin B₁₂ cofactor and a 4Fe-4S cluster. Due to their importance in proliferating cells, RNRs are potential drug targets for cancer treatment, for antiviral agents and for novel antibiotics in the fight against pathogenic bacteria.

Classification of RNRs

All RNRs are believed to have the same evolutionary origin, with a similar S• based reaction mechanism and a conserved ten-stranded α/β barrel fold of the catalytic subunit enclosing the S• (Figure 2) (37,38). However, the RNRs have been divided into three different classes based on allosteric regulation, oxygen dependency, sequence similarity and the cofactor utilized to generate the S• (12,39,40).

Class I RNRs are oxygen-dependent RNRs, generating a stable tyrosyl radical (Y•) (classes Ia and Ib) using a dinuclear metal cofactor in a small, radical-generating subunit, from where the Y• is shuttled to the catalytic subunit for every turnover. Class Ia RNR is the only class encoded in eukaryotes, but exists also in bacteria and viruses. Consisting of only one subunit, the prokaryotic class II RNRs (encoded by the *nrdJ* or *nrdZ* genes) generate their radical from the homolytic cleavage of the carbon-cobalt bond in the vitamin B₁₂ cofactor (adenosylcobalamin) (41). In this reaction, Co^{III} is reduced to Co^{II}, and a deoxyadenosyl radical is formed. The cofactor binds in the α/β barrel fold close to the substrate binding site and the cysteine that is oxidized to S• (42). Both of these classes operate in the presence of oxygen, class I being strictly aerobic, whereas class II having two independent pathways for radical generation, one being oxygen-dependent (41). Class III RNRs (belonging to the radical SAM superfamily) (encoded by the *nrdD-nrdG* genes) are anaerobic and use a 4Fe-4S cluster to homolytically cleave AdoMet, generating a glycy radical via a deoxyadenosyl radical, in the separate cluster containing activase. This glycy radical, which is very sensitive to oxygen, is responsible for S• generation in the active site (34,43).

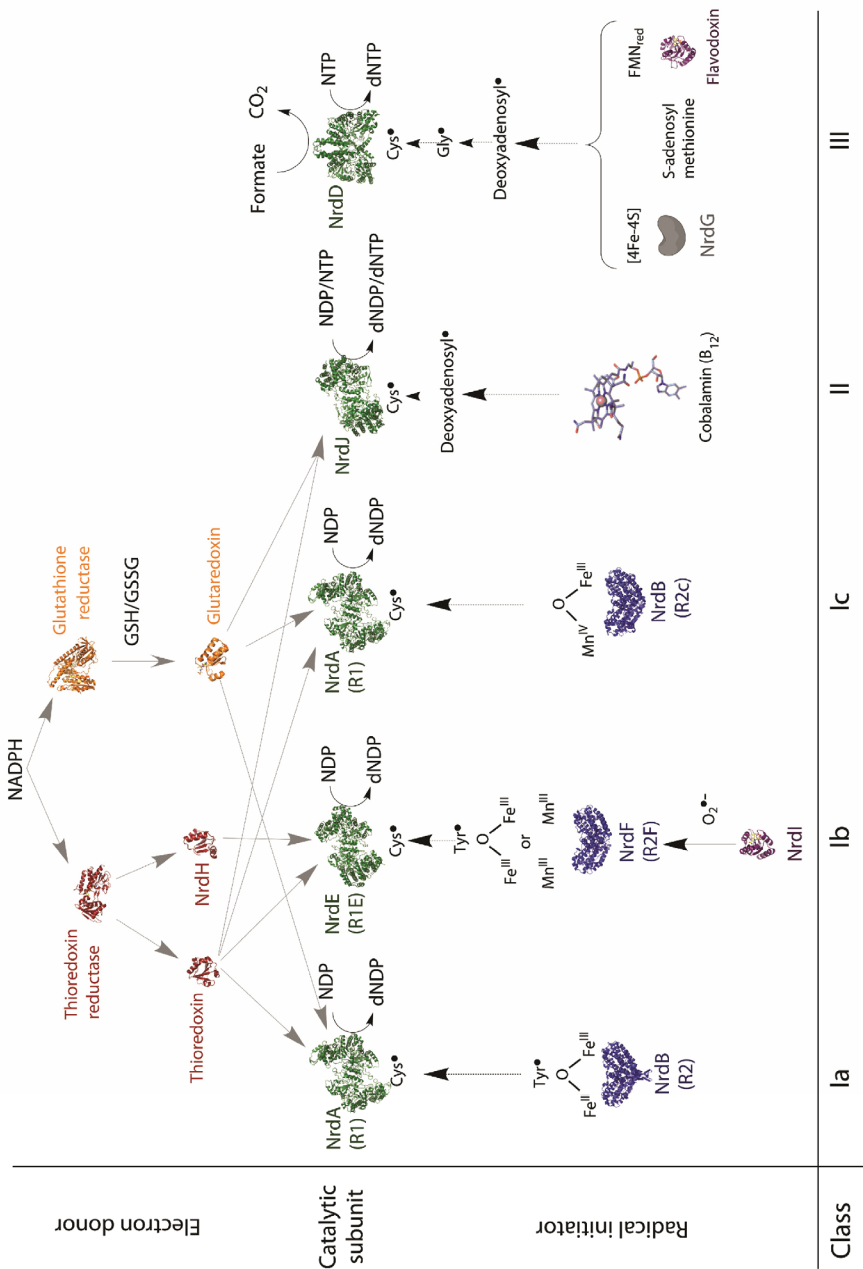


Figure 1. Schematic overview of the three RNR classes, showing the diversity of substrate specificity, electron donors and radical initiators. The figure is adapted from (44) and (45), with some modifications.

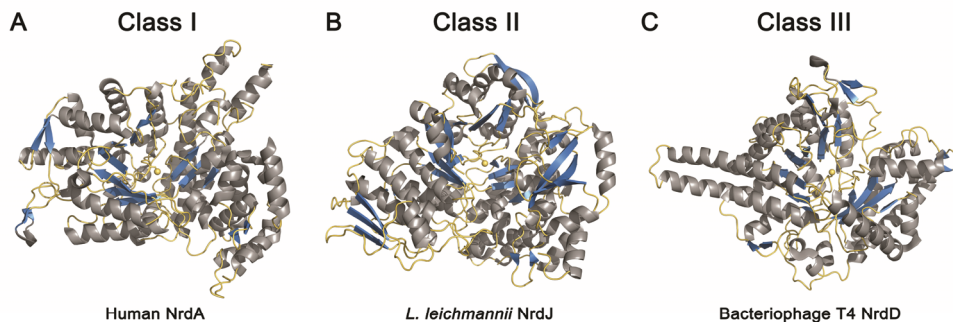


Figure 2. Crystal structures of the catalytic subunits in different RNR classes, showing the conserved α/β barrel fold. The active site cysteine responsible for S^\bullet generation is shown in the center of the barrel in yellow ball-and stick representation. (A) Human class I NrdA (PDBid:2WGH) (46), (B) *Lactobacillus leichmannii* class II NrdJ (PDBid:1L1L) (37), and (C) bacteriophage T4 class III NrdD (PDBid:1H7A) (47).

Class I RNRs

All class I RNRs contain two components; one catalytic subunit where the substrate binding site is located (R1), and one component responsible for generation of a radical center (R2). Active class I RNRs are assembled as two homodimeric subunits, α_2 and β_2 .

Nucleotide reduction is initiated through the reversible one electron oxidation of a conserved cysteine residue to a S^\bullet in the larger catalytic α_2 subunit (R1), originated by a dinuclear metallocofactor and Y^\bullet positioned in the β_2 subunit (R2) (classes Ia and Ib). The R2 subunit has a conserved structural fold consisting of an eight-helical bundle, as initially reported in the first structure of the radical-generating subunit from *Escherichia coli* in 1990 (48,49). All R2 subunits contain a dinuclear metal cluster located within a four-helix bundle (50), and the metal-binding residues are identical in most class I RNRs, where the di-metal clusters are coordinated by four carboxylates and two histidines, in close proximity to the tyrosine residue that generates the Y^\bullet (51) (or a phenylalanine in class Ic) (Figures 3 and 4).

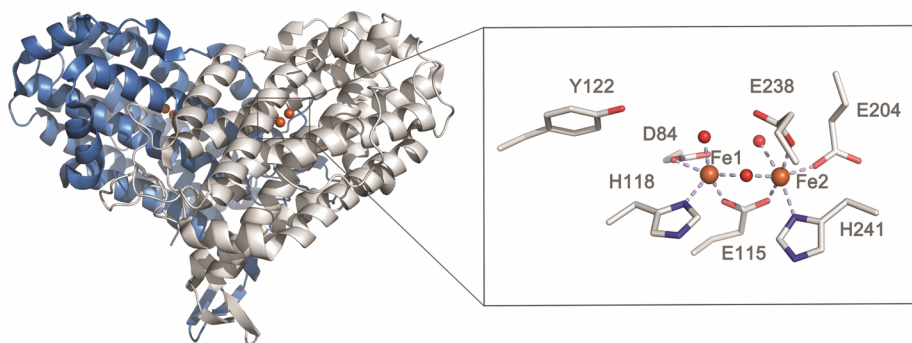


Figure 3. The RNR class Ia R2 subunit from *E. coli* (PDBid:1RIB) (49). The two monomers of the radical-generating subunit are colored by monomer and displayed as a dimer (β_2) (left). The monomers each contain two iron ions, shown as orange spheres. The inset panel on the right shows the metal ion site, where the Fe ions are shown as orange spheres, and the coordinating amino acids and Tyr are represented as sticks and colored by atom type.

The class I RNRs are divided into three structurally homologous subclasses; Ia, Ib, and Ic (Figure 4). Although class Ia and Ib RNRs have identical coordination sites, studies have shown that the class Ib NrdF can also utilize an active $\text{Mn}^{\text{III}}_2\text{-Y}\cdot$ cofactor (Figure 4D) (17,18,52), in addition to the classical $\text{Fe}^{\text{III}}_2\text{-Y}\cdot$ cofactor (Figures 4A-C), which can be assembled in both subclasses (53,54). In contrast to classes Ia and Ib, the newly discovered class Ic RNR, so far only characterized in the intracellular pathogen *Chlamydia trachomatis*, has been shown to be able to utilize a stable, heterodinuclear $\text{Mn}^{\text{IV}}\text{Fe}^{\text{III}}$ cofactor (Figures 4E and F) to initiate reduction of nucleotides in the catalytic site of R1 (19,20,55,56). This subclass contains a phenylalanine residue instead of the radical-generating tyrosine found in classes Ia and Ib. The different RNR subunits are encoded by the *nrd* genes. The NrdA/NrdE (R1/R1E) and NrdB/NrdF (R2/R2F) subunits are encoded by the *nrdA* and *nrdB* genes, respectively, in class Ia; the *nrdE* and *nrdF* genes, respectively, in class Ib; and by the *nrdA* and *nrdB*^{Phe} genes, respectively, in class Ic. While the operon structures of the genes encoding these subunits are *nrdAB* and *nrdAB*^{Phe} in classes Ia and Ic, respectively, the class Ib RNR operon structure encodes two additional proteins; NrdH and NrdI, and the gene arrangement is in most cases *nrdHIEF*. Class Ib RNRs will be discussed in more detail in the next section.

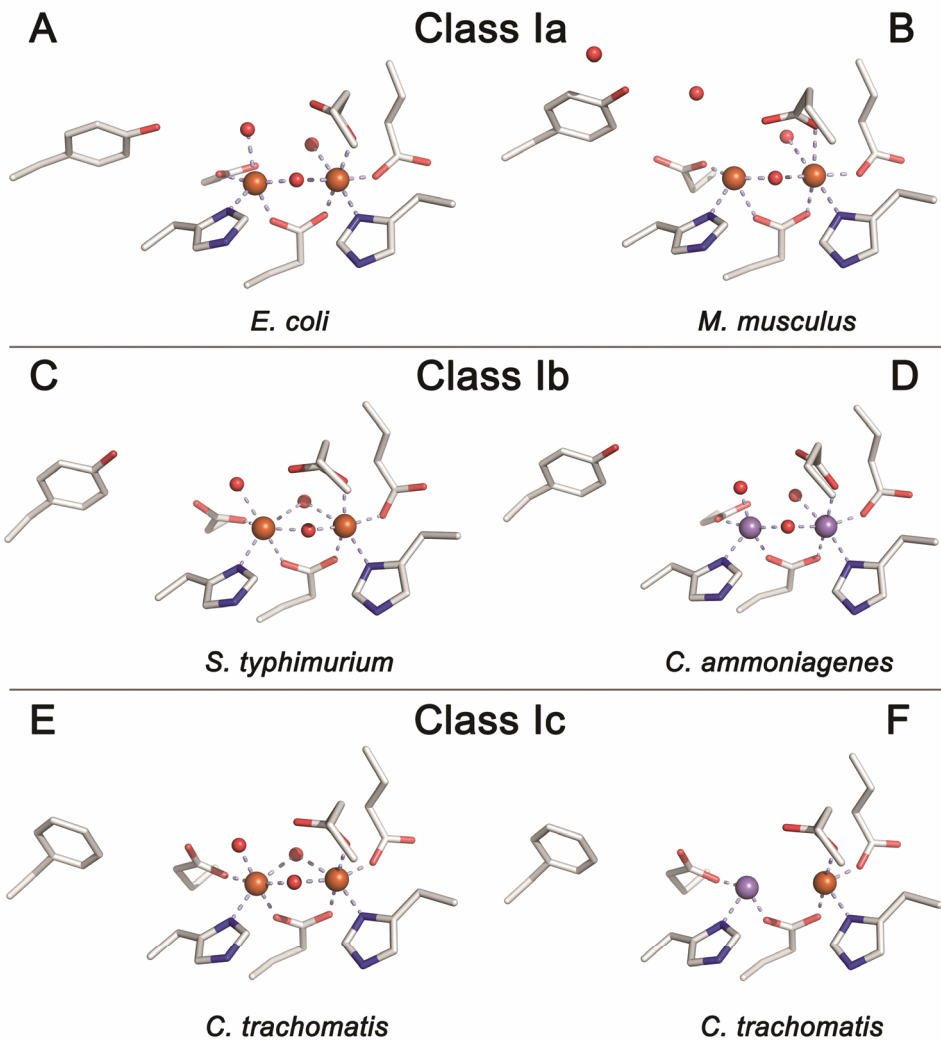


Figure 4. The metal ion sites in class Ia, Ib and Ic RNR. Fe -and Mn ions are shown as orange and purple spheres, respectively, and the coordinating amino acids and Tyr or Phe are represented as sticks and colored by atom type. (A) *E. coli* class Ia RNR (PDBid:1MXR) (57), (B) mouse class Ia RNR (PDBid:1W68) (50), (C) *Salmonella typhimurium* class Ib RNR (PDBid:2R2F) (58), (D) *C. ammoniagenes* class Ib RNR (PDBid:3MJO) (17), (E) *C. trachomatis* class Ic RNR (PDBid:1SYY) (55), and (F) *C. trachomatis* class Ic RNR (coordinates were obtained from Martin Högbom) with one metal center occupied by iron and the other by manganese.

Many organisms can express multiple classes of RNRs, where expression varies depending on growth conditions, such as adaptation to different O₂ levels in the environment. Further complexity can also be provided by the presence of more than one enzyme belonging to the same class or subclass. For example, *Streptomyces clavuligerus* and *Pseudomonas aeruginosa* express class I and class II RNRs, using both classes during aerobic growth (59,60). *E. coli* expresses two subclasses of class I RNRs; class Ia and class Ib (61) (in addition to class III (62)) while *Saccharomyces cerevisiae* contains two essential RNR small subunit genes, as well as two large subunit genes, coding for four proteins with non-overlapping function (63-65). Another example is the presence of a p53-incucible small subunit found in mammals, fishes, birds and possibly nematodes. The p53R2 protein is expressed when the tumor suppressor protein p53 is defective (66,67). *Mycobacterium tuberculosis* encodes the class Ib RNR as well as the class II RNR. The class Ib RNR in *M. tuberculosis*, however, is coded by a gene cluster containing intergenic spacings, contrary to the *nrdHIEF* operon structure seen in most class Ib RNR containing genomes (Figure 5). The well-characterized *M. tuberculosis* active small subunit, NrdF2/R2F-2, is encoded by the *nrdF2* gene. In addition, an alternate small subunit, NrdF1/R2F-1, encoded by *nrdF1* is expressed in this bacterium, previously thought to be unable to form a functional class Ib RNR with R1 (68-71) (see Paper I). Recently, another R2c-like protein (Rv2033) was characterized in *M. tuberculosis*, denoted R2lox, lacking RNR activity, and proposed to be a ligand oxidase (72).

M. tuberculosis H37Rv RNR-encoding genes

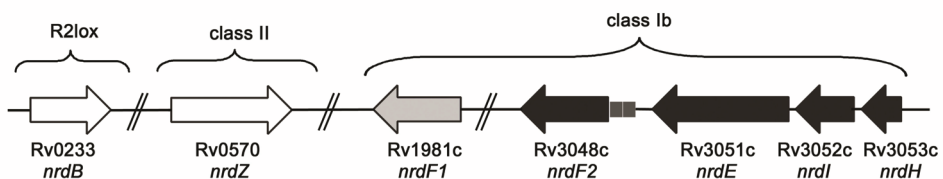


Figure 5. Organization of the RNR-encoding genes in *M. tuberculosis*, shown as arrows. The *nrdF1* gene is not linked to *nrdF2*, and neither of the genes encoding the small subunit of class Ib RNR are linked to *nrdE*; the gene encoding the large subunit.

All class I RNR subclasses are usually assembled in the $\alpha_2\beta_2$ functional form (Figure 6A). However, different oligomeric forms have recently been described and

discussed (Figure 6) (46,73-76). Recent human R1 structures show binding of effectors at different recognition-binding sites in an α_2 assembly (Figure 6B), and an inactive $\alpha_4\beta_4$ oligomeric form of the *E. coli* class Ia RNR has been observed in the presence of elevated levels of dATP (Figure 6D), also obtained as an interlock form of an $(\alpha_4\beta_4)_2$ complex (77). Additionally, a hexameric α_6 ring-like structure has been observed in the crystal packing of R1 from *S. cerevisiae* (Figure 6C).

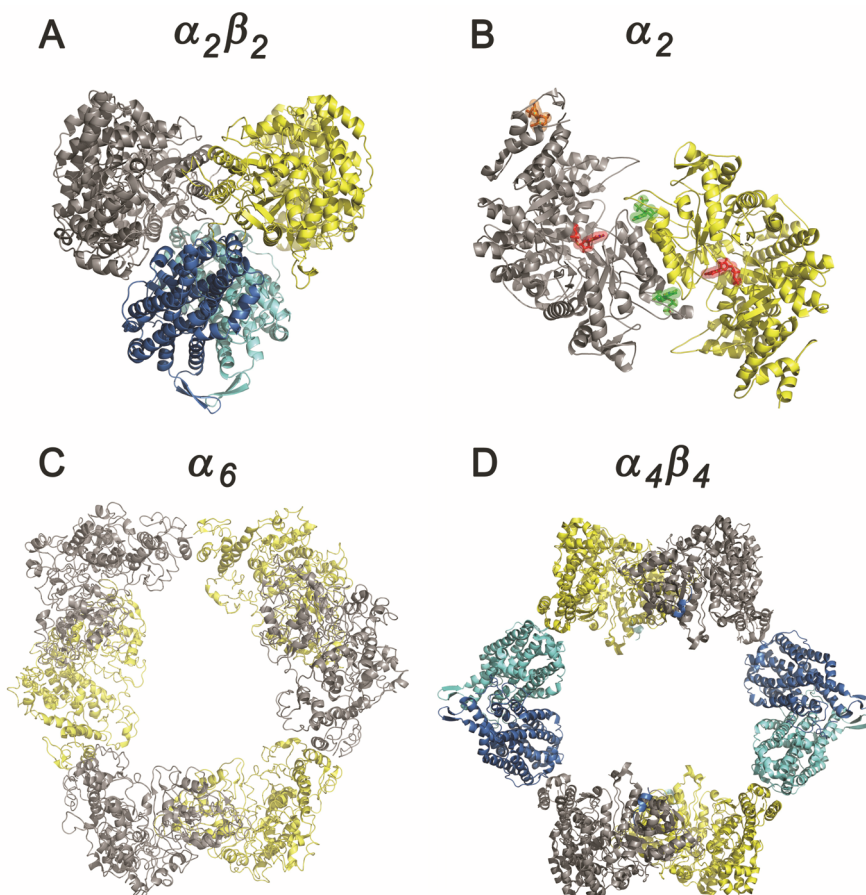


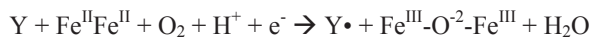
Figure 6. Different RNR molecular assemblies. (A) The proposed *E. coli* class Ia $\alpha_2\beta_2$ complex, generated by alignment of the R2 dimer (β_2) with the R1 dimer (α_2), using the original class Ia $\alpha_2\beta_2$ holocomplex coordinates (PDBid:1RIB) (49,78), (B) the human R1 dimeric structure (α_2) shown with TTP (green), GDP (red) and ATP (orange) bound at the S (specificity) site, C (catalytic) site and A (activity) site, respectively (PDBid:3HND, 3HNE) (46), (C) hexameric packing of R1 (α_6) in *S. cerevisiae* (PDBid:3PAW) (46), (D) the $\alpha_4\beta_4$ ring-like structure in *E. coli* (PDBid:3UUS) (75), see also (76).

The class Ib RNR system

Class Ib RNRs are the primary sources of dNTPs for a wide variety of prokaryotes, including many pathogens, such as *M. tuberculosis*, *Bacillus anthracis*, *Streptococcus pyogenes*, and *Bacillus cereus* (79). The class Ib enzyme consists of the α_2 (NrdE) and β_2 (NrdF) subunits (58), where the active form, as in class Ia, is believed to comprise an $\alpha_2\beta_2$ stoichiometry (38,78). Initially, class Ia and Ib RNRs were divided into two subclasses based on polypeptide sequence homology and allosteric regulation. Both subclasses possess identical metal-binding residues, and they were for a long time assumed to generate an $\text{Fe}^{\text{III}}_2\text{-Y}\cdot$ cofactor. However, initially proposed by Auling and coworkers (80-82), several recent studies performed on class Ib RNRs from *E. coli* (18,83), *Corynebacterium ammoniagenes* (17), *Bacillus subtilis* (84-86), *B. anthracis* (87), and *B. cereus* (52,87) have demonstrated that these RNRs can also utilize a $\text{Mn}^{\text{III}}_2\text{-Y}\cdot$ cofactor in their NrdF subunits, to initiate nucleotide reduction in R1. Hence, class Ib RNRs are unique in that they can assemble both active $\text{Fe}^{\text{III}}_2\text{-Y}\cdot$ and $\text{Mn}^{\text{III}}_2\text{-Y}\cdot$ cofactors.

Active $\text{Fe}^{\text{III}}_2\text{-Y}\cdot$ cofactor generation

Similar to the class Ia RNR, the $\text{Fe}^{\text{III}}_2\text{-Y}\cdot$ cofactor can be formed *in vitro* by self-assembly from apo-NrdF in the presence of Fe^{II} , O_2 , and an additional electron, forming the $\text{Y}\cdot$ required for dNDP formation in the α_2 subunit (NrdE) (39,53,54,88). The formation of the $\text{Fe}^{\text{III}}_2\text{-Y}\cdot$ has been well characterized in the class Ia RNRs, and has been studied in detail especially in *E. coli*. The diferric iron cluster and the $\text{Y}\cdot$ are formed when molecular oxygen reacts with diferrous iron in the radical generating RNR subunit:



After oxygen binding to the diferrous iron site, a μ -peroxodiferric intermediate ($\text{Fe}^{\text{III}}\text{-O-O-Fe}^{\text{III}}$) is likely formed (89,90), possibly followed by reduction by a neighboring tryptophan residue, leading to the formation of intermediate X ($\text{Fe}^{\text{IV}}\text{-O-Fe}^{\text{III}}$) (91,92). This intermediate spontaneously decays to the active $\text{Fe}^{\text{III}}\text{-O-Fe}^{\text{III}}$ cluster, oxidizing the nearby catalytically essential tyrosine to a $\text{Y}\cdot$. Kolberg *et al.* (36) have proposed a reaction pathway for the generation of the $\text{Y}\cdot$ in *E. coli* class Ia R2, which was recently also revised by Tomter *et al.* (45).

Active Mn^{III}_2 -Y• cofactor generation

Contrary to the self-assembly of the active Fe^{III}_2 -Y• cofactor in NrdF, the active Mn^{III}_2 -Y• cofactor can only be generated from the Mn^{II}_2 site in a self-assembly process in the presence of O_2 and the reduced flavodoxin-like protein NrdI (18). NrdI, encoded by the *nrdI* gene, is found in all organisms with genomes coding for the class Ib RNR (93,94). In most organisms expressing the class Ib RNR, the corresponding genes are organized in a cotranscribed *nrdHIEF* operon structure (61). NrdI contains an FMN cofactor, demonstrated to be able to act as a two-electron reductant (95,96) (Figure 7), and originally proposed to act as a reductant for generation and maintenance of the active Fe^{III}_2 -Y• cofactor (93). However, later biochemical studies proposed that NrdI, in its fully reduced hydroquinone form (NrdI_{hq}, containing FMNH⁻) reacts with O_2 providing the oxidant, H_2O_2 or HO_2^- , required for generation of the active Mn^{III}_2 -Y• cofactor, also supported by spectroscopic and crystallographic studies (17,18,97). The most recent work in this field, elucidated by Cotruvo *et al.* (23), has suggested through monitoring of the Mn^{III}_2 -Y• cofactor assembly by stopped flow absorption and rapid freeze quench EPR spectroscopies, that the metal-ion cluster oxidant is in fact $O_2^{\bullet-}$ (Figure 8). This reactive oxygen species is produced by the reaction of NrdI_{hq} with O_2 , oxidizing NrdI to its neutral semiquinone form (NrdI_{sq}, containing FMNH•) (23). The hydrophilic $O_2^{\bullet-}$ is believed to diffuse through a proposed hydrophilic solvent channel, extending from the flavin cofactor of NrdI to metal site 2 in NrdF. This channel is structurally conserved in *B. cereus* and *E. coli* NrdF, as confirmed by the two first crystal structures of NrdI in complex with NrdF (97) (see Paper II). This oxidant channel is distinct from the hydrophobic access route proposed for O_2 transport to the diferrous site in class Ia RNR, and presumably also for class Ib Fe^{II}_2 -containing RNRs (49). Studies have shown that the Mn^{III}_2 -Y• cofactor can be formed both *in vitro* and *in vivo* (52,83), and that the manganese form of the enzyme has a higher specific activity compared to the iron form, as in the case of *B. anthracis* (87), *B. cereus* (98) and *B. subtilis* (84), all showing a 10-fold increase. It is still not fully understood how the *in vitro* process of cofactor assembly using identical metal coordinating ligands, but different metals and oxidants (99), is controlled *in vivo*.

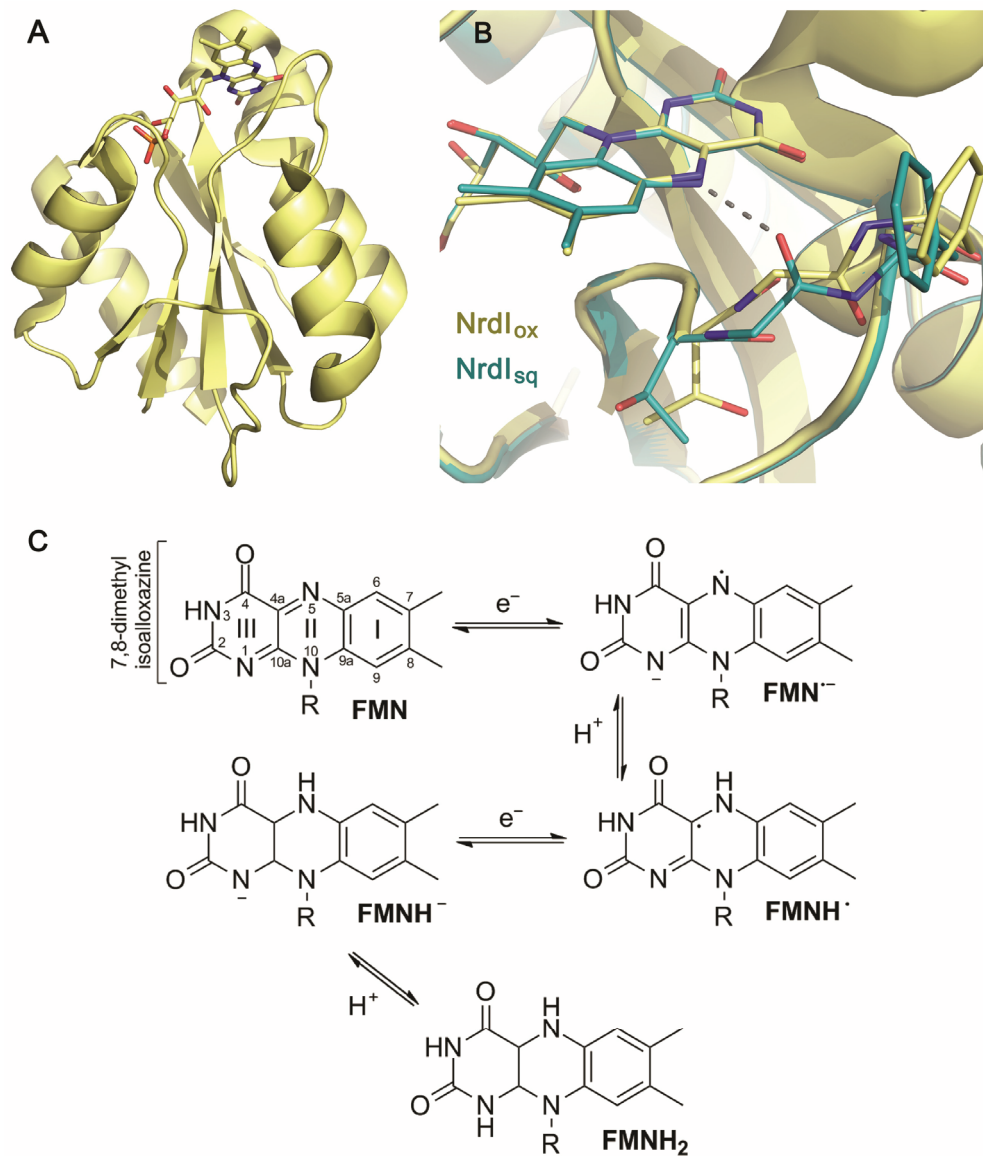


Figure 7. (A) Overall structure of the *B. cereus* NrdI (PDBid:2X2O) (96), with the FMN cofactor represented as sticks. (B) Structural alignment of NrdI structures with the FMN cofactor in different redox states. Residues proximal to the FMN cofactor on the 40S loop, as well as the active site of the oxidized form of the FMN cofactor are shown in yellow (PDBid:2X2O) (96), while the one-electron reduced semiquinone form is shown in turquoise (PDBid:2X2P) (96), all shown as sticks. A conformational change in the 40S loop is induced upon reduction of the FMN cofactor, resulting in a peptide flip between residues 44 and 45. This orients the Gly44 carbonyl group towards N5 of the FMN cofactor, initiating hydrogen bonding (shown as dashed lines). (C) Flavin mononucleotide redox and protonation states.

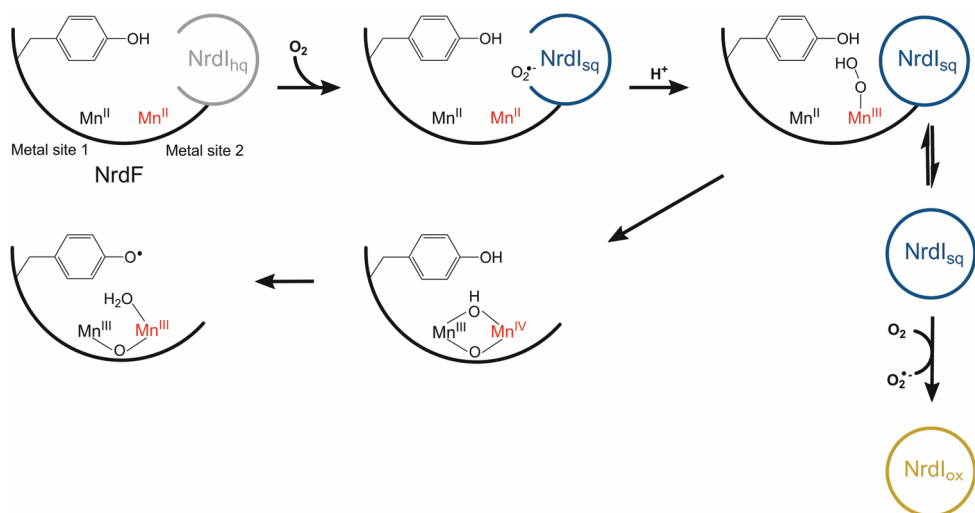


Figure 8. The latest proposed mechanism of Mn^{III}₂-Y• generation in NrdF. One-electron reduction of O₂ by NrdI_{hq} generates O₂^{•-}. The O₂^{•-} is proposed to be channeled through a hydrophilic solvent channel to Mn^{II}₂-NrdF, reacting with and forming a Mn^{III}Mn^{IV} intermediate, which decays to Mn^{III}Mn^{III}, oxidizing tyrosine to Y•. The detailed structures of the proposed Mn^{III}Mn^{III}-OO(H) and Mn^{III}Mn^{IV} intermediates are unknown (23), where the latter intermediate might also exist in a different resonance condition. The oxidation state of NrdI when it dissociates from NrdF is also unknown. Mn2 is indicated in red.

In addition to the proteins encoded by the *nrdHIEF* operon, several accessory proteins have been shown or are suggested to act as interacting redox partners in the class Ib RNR. Ferredoxin/ flavodoxin-NAD(P)(H) oxidoreductases (FNRs) catalyse the reversible redox reaction between ferredoxins or flavodoxins and NAD(P)⁺/NAD(P)H. Some of these are believed to provide reducing power to NrdI, as well as to other ferredoxin/ flavodoxin-dependent enzyme systems such as some cytochrome P450s and methionine synthase (100-102). Reduction of the active site of the catalytic subunit of classes I RNRs is performed through the assistance of glutaredoxins (Grxs), Trxs, and other subclasses of the Trx superfamily. A detailed introduction to these disulfide oxidoreductases will be given in a later section.

Radical transfer from R2 to R1

RNRs use, as already mentioned, a free-radical mechanism, in which a transient S• in the active site of R1 initiates ribonucleotide reduction by abstraction of a hydrogen atom (H•) from the C3' of the ribose ring. In class II and III RNRs, the active site cysteine is

oxidized by direct hydrogen abstraction by a 5'-deoxyadenosyl radical or a stable glycy radical, respectively. In the case of class I RNRs, oxidation occurs by the Y• (class Ia and Ib) or Mn^{IV}Fe^{III} cluster (class Ic) stored in a subunit (R2) different than the catalytic R1 subunit. In the case of class Ia RNR, in which the radical initiation process has been studied extensively (103-106), the distance between the Y• in R2 and the active site cysteine in R1 has been proposed to be ~35 Å, based on the 3D model of the R1-R2 complex (78), as well as kinetic techniques and different spectroscopies, such as pulsed electron-electron double resonance (PELDOR) spectroscopy (107,108). Rather than a slow, single electron tunneling step, conserved redox-active aromatic amino acids in both subunits have been proposed to mediate a long-range intersubunit electron transfer with transient radical formation. The electron transfer is thought to be coupled to several short-range proton transfer steps (proton-coupled electron transfer or PCET). Even though no structure of the functional $\alpha_2\beta_2$ holoenzyme has been obtained till date, a radical transfer mechanism mediated by the aromatic residues has been established based on a docking model of R1-R2 (78). However, less is known about the proton transfer. Recent studies have also shown that the Fe^{III}₂ cluster in class Ia *E. coli* RNR also functions in the enzymes catalytic cycle, in addition to generation of the Y• (109).

Thioredoxin

Thiol-redox diversity

Redox pathways based on disulphide-bridges are involved in a variety of cellular processes, such as protein folding (110), enzymatic reactions as hydrogen donors (26), response to oxidative stress (111) and modulation of protein activity (112), and are important in the maintenance of redox states in cells. The involvement of thiols is also common for all RNR classes, where redox-active cysteines, thiyl radicals and thiol containing proteins play an essential role in the catalytic cycle of RNRs. In the oxygen-dependent class I and II RNRs, a pair of cysteines performing the reduction of the substrate is located in the active site of R1, in addition to the cysteine forming the thiyl radical. The active site cysteine pair is oxidized during the reaction, and is reduced by two additional cysteines located on the flexible C-terminus of the R1 subunit. Consequently, these C-terminal cysteines need to be reduced by an external reductant for each turnover (27,113). Such reduction reactions of disulfide bonds, as well as oxidation reactions of cysteine pairs, are mediated by thiol-disulfide oxidoreductases. The thiol-disulfide oxidoreductases are members of the Trx superfamily, performing the fast and reversible thiol-disulfide exchange between their active site cysteines and cysteines in the substrate protein (25). Trxs are small ubiquitous proteins found in bacteria, plants and animals. They all share a common C-X-X-C active site motif and show a conserved $\alpha/\beta/\alpha$ sandwich polypeptide fold. Examples of *E. coli* proteins exhibiting different functions, but all having a Trx-like fold, are presented in Figure 9. In class III RNRs, only one of the two active site cysteines found in class I and II RNRs is conserved, while the other is entirely absent. In contrast to Trx-like proteins, the reductant of the class III RNRs is formate, which is oxidized to carbon dioxide during catalysis (114,115).

Proteins involved in the oxidation of disulfide bonds, such as DsbA (a member of the Dsb (disulfide bond) family of enzymes), are involved in disulfide bond formation in periplasmic proteins in bacteria, catalyzing the oxidation of peptide and protein cysteines (116). Also, eukaryotic protein disulfide isomerases (PDI) are involved in the rearrangement of incorrectly disulfide-bonded proteins in the lumen of the endoplasmic reticulum of eukaryotic cells (117,118).

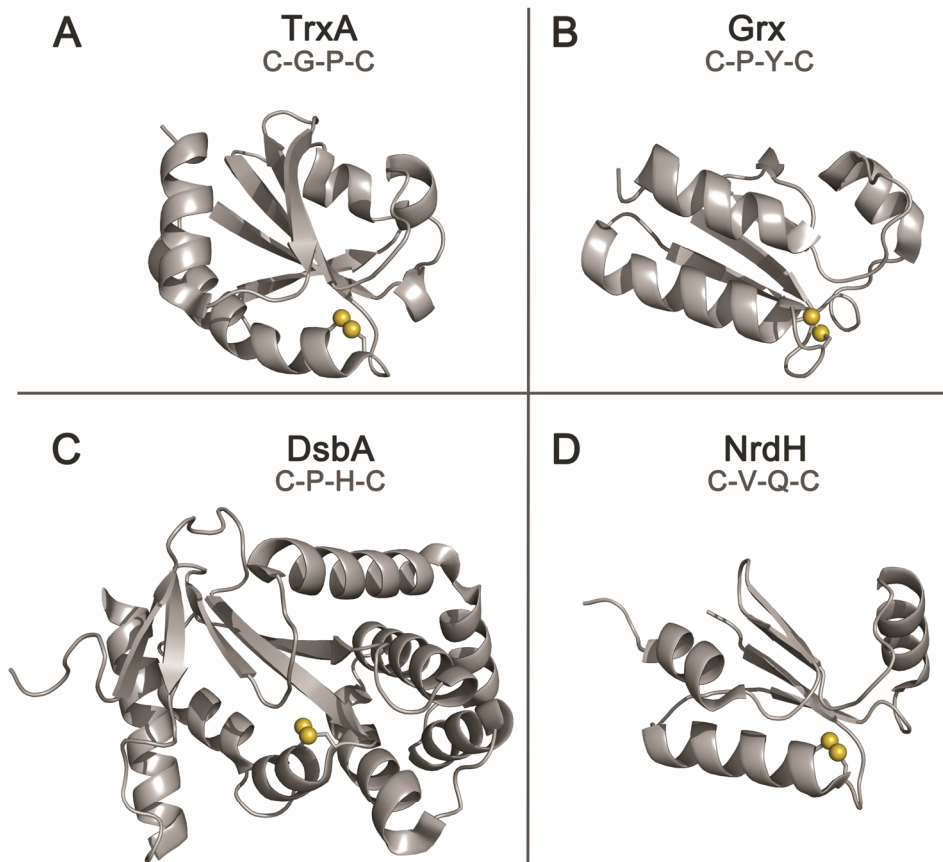
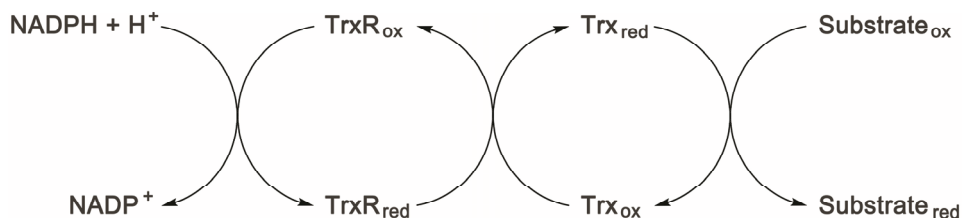


Figure 9. *E. coli* proteins belonging to the Trx superfamily, all containing the Trx-like fold and the C-X-X-C active site motif. (A) TrxA (PDBid:2TRX) (119), (B) Grx (PDBid:1EGO) (120), (C) DsbA (PDBid:1FVK) (121), and (D) NrdH-redoxin (PDBid:1H75) (122).

In the cytoplasm of *E. coli*, several pathways play roles in the reduction of disulfide bonds. Among the most studied members are the two thiol-disulfide bond reducing systems using the reducing potential derived from NADPH in the reduction of multiple cytoplasmic enzymes; the Trx system and the Grx system. The latter consists of three Grxs, glutathione (GSH) and glutathione reductase (Gor), while the former is composed of two Trxs and TrxR (25). The electrons from NADPH are transferred via TrxR or Gor, homodimeric enzymes called pyridine nucleotide disulfide oxidoreductases. TrxR reduces Trx, while Gor reduces glutathione disulfide (GSSG), a disulfide derived from two GSH molecules, to GSH, which then reduces Grx (123,124). In addition, NrdH-redoxin, which

functions as an electron donor for NrdE in the bacterial class Ib RNR, also has the Trx-like fold. This small redox protein, found in *E. coli* and several other organisms, is related in amino acid sequence to Grxs, but behave functionally as Trxs (122). While Grxs reduce their substrates using electrons derived from NADPH via Gor and GSH, Trxs and NrdHs reduce their substrates using electrons from NADPH via TrxR, as illustrated in Scheme 2.



Scheme 2. The electron flow from NADPH to the final substrate, mediated by TrxR and Trx.

Other members of the Trx superfamily, are the glutathione S-transferases and the hydroperoxidases (125), however, these proteins do not contain a C-X-X-C active site motif. Regardless of differences in their active sites, all the above mentioned proteins are related by their Trx fold, forming distinct, but structurally related families (126).

The thioredoxin-like fold and active site motif

The crystal structure involving an oxidized active site C-X-X-C motif was first solved for the *E. coli* Trx (127), in which the molecule showed to include a central β -sheet motif, and hence, core of five parallel and antiparallel strands surrounded by four α -helices. Thus, the characteristic Trx-fold is noticeably smaller than Trx itself, lacking one β -strand and one α -helix. Extra residues and secondary structure elements are present in all other proteins containing the standard fold as well, in addition to the approximately 80 residues making up the Trx fold. The four Grx orthologs found in *E. coli* also revealed the classical Trx-like fold with a central pleated sheet surrounded by helices (128,129). NrdH seems to be a hybrid of Trx and Grx (Figure 9). Despite these differences, functional similarity is found among several important classes of redox proteins, including Trx, NrdH and Grx, which all share the C-X-X-C similar reaction mechanisms.

E. coli Trx1 was first discovered as the electron donor for RNR (26). Based on sequence similarity, a second Trx, Trx2, was also discovered as a reductant for RNR, despite some structural and functional differences compared to Trx1 (130). Grx1 was discovered as an alternative electron donor for RNR, coupling the reducing capacities of GSH and Gor to the enzymatic formation of deoxyribonucleotides (128,131,132). In addition to their involvement in electron transfer in several enzymatic systems, members of the Trx superfamily are involved in a range of other cellular functions, such as signal transduction pathways, sulfate assimilation and involvement in oxidative stress response (133-135).

The two cysteine residues in the C-X-X-C motif can reversibly form a disulfide bond, enabling Trx-related proteins to participate in disulfide exchange reactions (136). The residues between the two cysteines vary among the different protein classes, including Trxs and Grxs. In *E. coli* Trx, the disulfide bridge is formed from Cys32 and Cys35, spaced by Gly33 and Pro34 (C-G-P-C). Cys32 is the N-terminal nucleophilic cysteine, while Cys35 is the C-terminal, buried cysteines. The three Grx orthologs found in *E. coli*, Grx1, Grx2, Grx3 all share a C-P-[F-Y-W]-C active site sequence (137), whereas Grx4, a member of the last group of Grxs, is a monothiol enzyme containing an active site C-X-F-X motif, usually as C-G-F-S (138,139). NrdH-redoxins typically contain a C-[VM]-Q-C motif (140). Other variations to the two residues flanking the redox active cysteines are found among additional members belonging to the Trx superfamily. DsbA contains an active site conserved C-P-H-C motif (141), while the eukaryotic PDI contains the active site sequence C-G-H-C (142).

Mechanism of electron transfer in thioredoxin

The reduction potentials of thiol-disulfide reactions are correlated with the pK_a value of the surface exposed N-terminal reactive cysteines. A low redox potential has been correlated with a relatively high pK_a value and vice versa. For example, the *E. coli* Trx low redox potential of -270 mV (143) is correlated with a relatively high pK_a value of 7.1-7.4 (144). Experiments have shown that the -X-X- residues in the active site motif contribute to changes in the pK_a values, and hence, the tuning of redox potentials (145).

The side chain of the *E. coli* Trx N-terminal Cys32 is exposed to the solvent, and has a pK_a value which is lowered from approximately 9 to 7, crucial to drive efficient thiol-disulfide exchange reactions at physiological pH values (123). In order to give disulfide reductants low reduction potentials, nature has evolved enzymatic systems with the Cys32

thiol initiating the nucleophilic attack positioned in a special microenvironment. The lowered nucleophilic cysteine pK_a value, leading to deprotonation, has been suggested to involve contributions from several factors, including assistance from an alpha-helix dipole (146), charge-charge interactions (147) and intra-protein hydrogen bonding (148). It has been proposed that the latter is the leading determinant to be considered when predicting pK_a values, resulting in the suggestion that the low pK_a value of the N-terminal Cys32 is due to hydrogen bonding to the Cys35 amide proton (149,150). However, the pK_a value of Cys35 is estimated to values up to 4 units higher, making this residue virtually unreactive (136,151). There are no polar or acidic groups in the immediate environment of the C-terminal buried Cys35 $S\gamma$ -atom that can stabilize a thiolate prior to the second nucleophilic attack. As an explanation, a proximal, conserved Asp26 has been proposed to act as a general acid/base catalyst in the deprotonation of the thiol of Cys35, through a water molecule positioned between the Asp26 carboxyl group and the Cys35 $S\gamma$ -atom (136,152). This hypothesis has later been supported by the analysis of a 1 Å resolution structure of oxidized Trx from *Acetobacter acetii*, where a water molecule is aligned between Asp26 and Cys35, well positioned to participate in proton transfer between the Asp26 and Cys35 side chains (153). However, reduced crystal structures of Trx showing this feature are yet not solved. Even though the replacement of Asp26 in Trx strongly impairs the catalytic reaction rate in the redox reactions of Trxs (154), the deprotonation mechanism of the buried Cys35 is still debated (136).

The fundamental mechanism of Trx-mediated electron transfer, proposed by Kallis and Holmgren in 1980 (155), is explained using *E. coli* amino acid numbering in Figure 10. Electrons pass from reduced Trx to the substrate via several steps. The initial nucleophilic attack on the disulfide substrate involves Cys32, with the formation of a mixed disulfide (step 1) (Figures 10A and B). The next step, involving deprotonation of Cys35, makes the second nucleophilic attack caused by this thiolate possible. This resolves the mixed disulfide intermediate, generating a dithiol in the substrate (Figures 10C and D). The proton abstraction necessary to induce the nucleophilic attack of the last thiolate, illustrated in step 2, is possibly assisted by Asp26, but not completely understood.

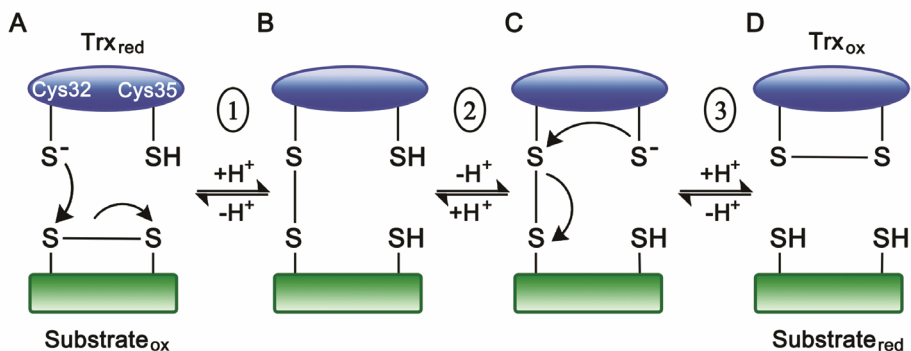


Figure 10. The disulfide reductase reaction mechanism of Trx. (A) The initial nucleophilic attack performed by the Trx N-terminal Cys on the substrate disulfide bond is followed by a deprotonation of the buried C-terminal Cys (step 2) and a second nucleophilic attack, resolving the mixed disulfide intermediate (C), and leading to a reduced substrate (step 3 and D).

Interestingly, variations to the possible role of Asp26 as an acid/base catalyst for the buried Cys are likely present among other subclasses of the Trx superfamily (Paper III). Some members lack the amino acid residue analogous to the *E. coli* and *A. aceti* Trx Asp26. Examples of such groups of proteins, possessing Trx functionality, are the NrdH-redoxins, previously shown to be able to act as reductants of the catalytic site of the R1 subunit in the class Ib RNR (87,156,157), and *Clostridium pasteurianum* Cp9-redoxins, involved in the reduction of various hydroperoxide substrates (158).

B. cereus ATCC 14579 class Ib RNR-encoding genes

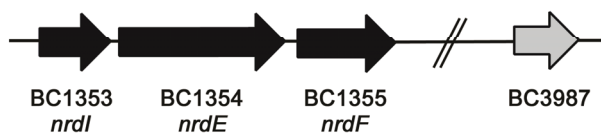


Figure 11. Organization of the genes encoding the *B. cereus* class Ib RNR. Contrary to the classical class Ib RNR operon structure, the gene coding for the putative NrdH-redoxin (BC3987) is not linked to the genes coding for NrdI, NrdE and NrdF.

The class Ib RNR operon from *B. cereus* lacks the *nrdH* gene encoding the NrdH-redoxin, differing from other characterized class Ib RNRs. However, a gene coding for a

small Trx-like protein, BC3987 (Figure 11), has been located in the *B. cereus* genome, revealing a significant amino acid sequence similarity with NrdH. The mechanism behind the proton abstraction of the C-terminal buried cysteine in these proteins has not been investigated until recently (Paper III).

AIMS OF STUDY

The aim of this thesis has been to structurally and functionally characterize proteins involved in the class Ib RNR system. Detailed knowledge about the mode of interaction between different RNR proteins at the molecular level, as well as catalytic mechanism, is crucial for the development of antimicrobial drugs. X-ray crystallography, combined with biochemical analysis, QM/MM calculations, as well as different spectroscopic techniques provides detailed information about the structural and functional features of these enzymes.

The *M. tuberculosis* class Ib RNR contains two genes encoding the small R2 subunit, *nrdF1* and *nrdF2*, encoding R2F-1 and R2F-2, respectively. The latter has previously been characterized, and assumed to be the only biologically active RNR small subunit. The lack of biochemical and biophysical data on the putative R2F-1 subunit lead us to carry out experiments corresponding to the first part of the thesis, involving biochemical and spectroscopic characterization of R2F-1.

In the second part of the project, an extensive crystallographic study of the *B. cereus* class Ib RNR small subunit in complex with NrdI was performed. It has been of great interest for us to investigate this protein-protein assembly, in order to examine geometric and structural features, as well as to investigate the binding modes between these proteins.

The class Ib RNR operon from *B. cereus* lacks the *nrdH* gene, coding for the NrdH-redoxin in other characterized class Ib RNRs. However, BC3987, a protein homologous to NrdH, has been located in the *B. cereus* genome. The presence of a Thr residue, also conserved in all NrdHs, was found located in the proximity of the C-X-X-C active site motif in BC3987, unlike in typical Trxs. This encouraged us to carry out a characterization of BC3987 and investigate the role of the Thr sidechain on the deprotonation of the C-terminal buried Cys, in order to find a model for the enzymatic reaction mechanism in BC3987 and other similar Trx-like proteins.

SYMMARY OF PAPERS I-III

Paper I

Hammerstad, M., Røhr, Å. K., Andersen, N. H., Gräslund, A., Högbom, M., and Andersson, K. K. (2014) The class Ib ribonucleotide reductase from *Mycobacterium tuberculosis* has two active R2F subunits. *J. Biol. Inorg. Chem.* DOI: 10.1007/s00775-014-1121-x

This paper presents the first evidence for an active diferric tyrosyl radical ($\text{Fe}^{\text{III}}_2\text{-Y}\bullet$) cofactor in the *M. tuberculosis* class Ib RNR putative R2F-1 small subunit, supported by UV-vis, X-band EPR, and rRaman spectroscopy. Additionally, R2F-1, which was previously thought to be inactive, showed enzymatic activity when assayed with R1.

The first genetic and biochemical characterization of the class *M. tuberculosis* class Ib RNR was performed almost two decades ago by Rubin and coworkers (68). The study revealed the presence of two genes, *nrdF1* and *nrdF2*, encoding the class Ib small subunit (R2F-1 and R2F-2, respectively). Since then, R2F-2 containing the $\text{Fe}^{\text{III}}_2\text{-Y}\bullet$ cofactor has been well characterized, and suggested to be the only R2 subunit able to form a functional class Ib RNR in *M. tuberculosis* with R1, thereby implying that R2F-1 is unable to substitute for R2F-2 in the active class Ib RNR system.

In this study, we have found that R2F-1 is able to generate an active $\text{Fe}^{\text{III}}_2\text{-Y}\bullet$ cofactor. X-band EPR studies reveal minor differences in the radical spectra when comparing the R2F-1- $\text{Fe}^{\text{III}}_2\text{-Y}\bullet$ with the previously characterized R2F-2- $\text{Fe}^{\text{III}}_2\text{-Y}\bullet$, and the simulated EPR spectra of R2F-1 and R2F-2 display well resolved, nearly identical anisotropic proton hyperfine coupling parameters (*hfc*). The study also presents the first rRaman characterization of structural details associated with the $\text{Y}\bullet$ cofactor of R2F-1 and R2F-2 in *M. tuberculosis*, indicating that no exchangeable hydrogen atom is present adjacent to the radical. Most importantly, Fe-reconstituted R2F-1, when assayed with R1, revealed similar specific activity to that of R2F-2, comparable to previously published results for the latter. This suggests that the *M. tuberculosis* class Ib RNR can function with two biologically active small subunits.

Paper II

Hammerstad, M., Hersleth, H. -P., Tomter, A. B., Røhr, Å. K., and Andersson, K. K. (2014) Crystal structure of *Bacillus cereus* class Ib ribonucleotide reductase di-iron NrdF in complex with NrdI. *ACS Chem. Biol.* **9** (2), 526–537

The first crystal structure of the *E. coli* class Ib RNR NrdF subunit in complex with the flavoprotein NrdI was published by Boal *et al.* (97) in 2010, revealing the presence of a continuous channel connecting the FMN cofactor of NrdI with the NrdF Mn^{II}₂ active site.

In this paper, we present the first crystal structure of *B. cereus* NrdI-Fe₂-NrdF. Compared to the *E. coli* NrdI-Mn^{II}₂-NrdF crystal complex, our structure confirms similar NrdI-NrdF binding through a network of conserved residues lining the core interface in both structures. In the *E. coli* and *B. cereus* complex structures, these charged and polar residues create a similar hydrophilic channel, suggested to serve in transport of the hydrophilic oxidant, O₂^{•-}. This supports a conserved NrdI-NrdF binding in all class Ib RNRs, providing a general structural basis for cofactor activation.

The NrdI-Fe₂-NrdF structure presented in this paper contains a di-iron site, differing from the NrdI-Mn^{II}₂-NrdF structure from *E. coli*. Our work reveals a specific movement of a metal-coordinating carboxylate residue linked to the metal type present in the di-metal site, also supported by the *B. cereus* Fe₂-NrdF and Mn^{II}₂-NrdF crystal structures presented in this paper. In the NrdI-Fe₂-NrdF and Fe₂-NrdF structures, the carboxylate conformation seems to structurally block the access of an oxidant channeled from the FMN cofactor to the di-metal cofactor in NrdF. However, the carboxylate conformation seen in Mn^{II}₂-NrdF crystal structures opens up for the water network leading to the di-metal site in NrdF, allowing oxidant access.

We further show that binding of NrdI to NrdF introduces steric clashes in the NrdI-NrdF-NrdE formation, and discuss the potential mode of binding interactions between these proteins upon active cofactor generation and $\alpha_2\beta_2$ holoenzyme formation.

Paper III

Røhr, Å. K., Hammerstad, M., and Andersson, K. K. (2013) Tuning of thioredoxin redox properties by intramolecular hydrogen bonds. *PLoS One* **8** (7), e69411

In this paper, a small Trx-like protein from *B. cereus*, BC3987, has been characterized, and we have proposed a substrate reduction reaction mechanism for Trxs with a similar active site environment.

Together with certain other Trx-like proteins, BC3987 lacks the conserved carboxylate residue believed to function in deprotonation of the C-terminal cysteine, as proposed for the *E. coli* and *A. aceti* Trxs. However, BC3987 contains a Thr8 residue preceding the active site C-X-X-C motif, able to form a hydrogen bond to the buried cysteine. This residue has been shown to be conserved in other Trx-like proteins, such as NrdH-redoxins, and is believed to increase enzymatic activity, playing a central role in the reaction mechanism in these proteins.

Through biochemical assays comparing the wild type BC3987 with the Thr8Ala mutant, we have shown that the efficiency of substrate reduction is reduced for the mutant. Also, thiolate pK_a titrations were performed comparing the wild type and Thr8Ala mutant enzymes. The results revealed that the wild type enzyme may have two titratable thiolates with different pK_a values, 5.1 and 7.2, whereas the mutant enzyme has one thiolate with a pK_a value of 7.2, and a second thiolate with a different behavior. Additionally, the mutant was shown to be unstable at pH values below 5.4.

The paper also presents the high resolution crystal structures of the wild type BC3987, as well as the Thr8Ala mutant with oxidized active sites. Based on these crystal structures, as well as crystal structures from other organism showing different Thr8 rotamers, QM/MM calculations were performed in order to investigate the role of Thr8 in lowering of the buried cysteine pK_a value. The calculations revealed that the Thr8 hydroxyl group and the Gln9 amide proton could form hydrogen bonds to the buried cysteine. Based on the modeling studies of the reduced active site, and the biochemical investigations performed in this work, a reaction mechanism model is proposed. This model involves deprotonation of the buried cysteine by the proximal Thr residue, proposed for Trxs lacking an analogue to the acidic Asp26 residue believed to participate in deprotonation of the C-terminal thiol in *E. coli* Trx.

MY CONTRIBUTIONS TO PAPERS I-III

Paper I

Designed and carried out most of the experiments (cloning, protein expression and purification, activity measurements, UV-vis spectroscopy, preparation of EPR -and rRaman samples, contribution to EPR experiments), analyzed the corresponding data, performed structural investigations and discussion, and wrote the manuscript.

Paper II

Designed and carried out most of the experiments (protein expression and purification, single-crystal light absorption spectroscopy, protein crystallization and data collection), solved and refined several structures, investigated and analyzed crystallographic data, and wrote the manuscript.

Paper III

Carried out experiments (in particular work with the T8A mutant protein), analyzed data and participated writing the manuscript.

DISCUSSION

The main goal of my thesis has been to increase the knowledge of different proteins involved in the class Ib RNR, through structural, spectroscopic and biochemical investigations. In the following section, I will summarize the results presented in Papers I to III, and place these contributions in context with the ongoing research in the field of RNRs and other redox enzymes.

The discussion has been divided into four parts, starting with a short introduction to three of the biophysical techniques used; rRaman and EPR spectroscopy (Paper I), and X-ray protein crystallography (Papers II and III). Thereafter, the different findings from Papers I to III will be discussed; the alternative R2F-1 RNR subunit in *M. tuberculosis*, the structure of the *B. cereus* NrdI-NrdF crystal complex, and the *B. cereus* BC3987 thioredoxin.

A short introduction to biophysical techniques

X-ray protein crystallography

Crystallography is one of the most powerful methods used for visualization of three-dimensional images of molecules at atomic resolution. It can provide detailed structural information about functional aspects of proteins, such as conformational changes including metal coordination geometries, and mechanisms of binding.

In order to be able to visualize an object, light with the wavelength corresponding to the size of the objects is required. Atomic distances are in the 10^{-10} m range; hence, to resolve the positions of atoms within a molecule, X-ray radiation is required. In order to amplify the scattering signal, a prerequisite for solving a three-dimensional structure of a protein by X-ray crystallography is a well-ordered crystal that diffracts X-rays. Molecules pack in the crystal in an ordered pattern. Based on each equivalent point in the crystal, a unit cell can be defined. This three-dimensional array of molecules is described by the crystal lattice, whereas the whole symmetry of the lattice is defined by its space group.

The scattering of electromagnetic radiation from the electrons in a crystal, interfering constructively, generates a diffraction pattern, which can be used to determine the protein structure. The intensity of the diffraction spots depends on the position of atoms in the sample through which X-rays pass, and therefore, information about the molecular content of the unit cell. Since scattered X-ray beams in a diffraction experiment cannot be converted directly into an image as in conventional light microscopy, indirect computational procedures are crucial for structure determination. The structure factor is a function of the atomic content in the crystal, and sums up the scattering from all the electrons in the unit cell from each direction. Since the structure factor is the Fourier transform of the electron density, the electron density at every position in the unit cell can be calculated. One of the challenges in structure determination, however, is the fact that the time component of the scattered waves is lost during data collection. This is referred to as the phase problem. In order to solve the phase problem and hence, solve the structure by generating an electron density map, the approach used in this thesis has been “molecular replacement” (MR).

For improvement of the atomic coordinates corresponding to the final structural model, structure refinement is performed in an iterative manner. The generated model is compared to the diffraction data, until any discrepancy between the two has reached a minimum. The correctness and quality of the structure is evaluated, and the agreement between the model and the experimental diffraction data is measured by the *R*-factor.

Electron paramagnetic resonance spectroscopy

As an important complement to structural determinations by X-ray crystallography, electron paramagnetic resonance (EPR or electron spin resonance (ESR)) is a spectroscopic technique used to study species containing unpaired electrons. It detects changes in electronic spin configuration and depends on the presence of a permanent paramagnetic moment, being a useful and sensitive method for studying paramagnetic active sites in metalloproteins and free radical intermediates. Hence, EPR can give intrinsic information about protein-bound metal ions, the geometry of ligand binding and redox changes in electron transfer mechanisms. Class Ia and Ib RNRs use a di-metal oxygen cluster for a generation of a stable tyrosyl radical, and is well suited for EPR investigations.

In the presence of a magnetic field, the magnetic moment of unpaired electrons will align either parallel or antiparallel to the field, corresponding to the two spin states of the electron, with different energies. Transitions between these two energy levels can be induced by providing electromagnetic radiation with energies corresponding to the energy difference between these two levels. In EPR spectroscopy, the absorption of microwave radiation is observed due to the excitation of electrons from one electronic spin to another. The energy is determined by the resonance conditions; hence, the splitting of the two energy levels can be described as a function of the applied magnetic field:

$$\Delta E = g\beta B = h\nu$$

Where *h* is Planck's constant, *ν* is the frequency of the applied field (microwave), *g* is the electron *g*-factor, *β* is the Bohr magneton, and *B* is the external magnetic field.

The microwave radiation is absorbed due to a population difference in the energy levels involved, where the number of unpaired electrons in the lower energy level is greater than the number of electrons in the higher energy level. Thus, more transitions occur from the lower energy level state, resulting in a net absorption. In standard EPR, a

signal may be achieved by gradually increasing the magnetic field while applying electromagnetic radiation with a constant energy, $h\nu$, until the resonance condition is fulfilled. Amplitude modulation of the magnetic field with a fixed frequency results in the first derivative of the absorbed continuous wave (CW) EPR spectra. The EPR signal intensity is proportional to the population difference, which is dictated by the Boltzmann distribution. The amount of the studied species, such as free radical, can be determined by quantitation of the spin concentration through double integration of the EPR spectra. EPR measurements can be performed at different wavebands, most commonly at 9.6 GHz (X-band), but also at higher magnetic field and microwave frequencies (HF-EPR), such as 95 GHz (W-band), and at 285 GHz, important for separation of small g -tensor anisotropies.

The electron responds to the magnetic field, in addition to the surrounding field of atoms and molecules. The positions and splitting of the lines in the spectrum depend on the direction of the external field, relative to the molecular axes, called anisotropy. The symmetry of a spin center is reflected in its EPR signal g -anisotropy. Three g -values can result in splitting of the EPR signal, while the hyperfine couplings arising from the interaction of the unpaired electron with nearby nuclei spins, further split the fine structure of the spectra.

Resonance Raman spectroscopy

Resonance Raman (rRaman) spectroscopy is another powerful tool used to study the structure of metal ion environments in metalloproteins, as well as ligation modes of amino acid residues. In rRaman, the wavelength of the exciting laser is adjusted to correspond to a specific electronic transition in a molecule in order to increase the intensities of certain Raman bands. This makes the technique sensitive to changes in molecular bonding and conformations of specific structures, and can provide information about vibrational characteristics of metal centers and radicals. In RNR, the vibrational characteristics of tyrosyl radicals are sensitive to the presence of exchangeable hydrogens in the proximity of the phenoxyl oxygen. Therefore, the tyrosinate oxygen vibrational mode, $\tilde{\nu}_{7a}$, is sensitive to the presence of a hydrogen bond. rRaman spectroscopy is a valuable tool for detection of changes in out-of-plane bond angles, as well as proximal electronic changes affecting the tyrosyl radical state.

The RNR class Ib R2F subunit

For decades, the nature of the di-metal oxygen cluster and Y• cofactor in the small subunit of class I RNRs has triggered the curiosity of many scientists. Extensive characterization of these cofactors has been executed, gaining knowledge about metal-ion cluster identities, 3D structures, magnetic-optical properties, and reaction mechanisms. The bacterial class Ib R2F subunit is unique because of its ability to utilize different metal-ion clusters to generate a stable Y•, generating an active Fe^{III}₂-Y• cofactor or Mn^{III}₂-Y• cofactor. In the case of *M. tuberculosis*, the unusual and simultaneous presence of two R2F subunits was confirmed by Harvey Rubin and coworkers in 1997 (68). This led us to perform a biochemical and biophysical characterization of the second, putative R2F subunit R2F-1, in order to find out whether it could resemble the previously confirmed features of the well characterized R2F-2 subunit (Paper I). Despite the wide knowledge about the generation and nature of the Fe^{III}₂-Y• cofactor, a thorough understanding of the generation of the Mn^{III}₂-Y• cofactor is still not reached. Further complexity is also provided in the latter case, where the presence of an additional protein, NrdI, is needed as an electron donor for cofactor assembly. This encouraged us to investigate this protein-protein association further, employing the crystal complex of NrdI-Fe₂-NrdF from *B. cereus* (Paper II). This gave additional knowledge about the structure of the metal ion coordination environment in R2F, in addition to the work published by Boal *et al.* (97) in 2010, including the crystal complex of NrdI-Mn^{II}₂-NrdF from *E. coli*. We have also shown insight into the mode of interaction between the different proteins in the active $\alpha_2\beta_2$ holoenzyme formation. In contrast to NrdI, which provides electrons used for generation of the Mn^{III}₂-Y• cofactor in R2F, Trxs function as electron donors for the catalytic subunit R1. NrdH-redoxins have been shown to function as specific reductants of the active site of R1 in class Ib RNRs. Since the class Ib RNR operon in *B. cereus* lacks the *nrdH* gene, we carried out a characterization of BC3987, proposing a model for the reaction mechanism in these Trx-like proteins (Paper III).

M. tuberculosis has two active R2F subunits

The R2F-2 subunit of the class Ib RNR from *M. tuberculosis* was first shown to be active when assayed with the catalytic subunit almost two decades ago (68). The same study showed the presence of a Y• cofactor by EPR spectroscopy. Extensive EPR investigations of the R2F-2 subunit were later carried out by Gräslund and coworkers (159-161), confirming similar features as previously observed in the class Ib R2F subunit from *S. typhimurium* (162). In contrast, the alternate *M. tuberculosis* R2F-1 subunit has been suggested to be unable to substitute for R2F-2 in the active class Ib RNR, despite the high sequence identity level. In Paper I, we have shown that iron-reconstituted R2F-1, containing the Fe^{III}₂-Y• cofactor, shows similar specific activity as compared to R2F-2, when assayed with R1. These results are the first to demonstrate catalytic activity of the second putative R2F-1 subunit in *M. tuberculosis*, consistent with previously reported activity for R2F-2 (68). Both *nrdF1* and *nrdF2* genes have been shown to be expressed at similar levels in aerobic conditions (69), however, loss of the *nrdF1* gene has no significant effects on the cell viability or virulence (71). Therefore, the results from Paper I, confirming R2F-1 activity with R1, raise questions about the biological role of R2F-1, and hence, the aspect of a simultaneous presence of two active small RNR subunits in *M. tuberculosis*. One explanation could be changes in affinity for metal ion incorporation among the two subunits, during distinct growth conditions. For example, R2F-2 could be preferred as the active Mn^{III}₂-Y• cofactor generating subunit in *Mycobacteria* living in their natural habitats, such as soil or water, whereas R2F-1 could act as the preferred subunit responsible for generation of an active Fe^{III}₂-Y• cofactor used for nucleotide reduction during mammalian lung infection. Further investigations are required in order to elucidate the biological role of R2F-1. *M. tuberculosis* is the first species shown to simultaneously express two active class Ib RNR R2F subunits.

Spectroscopic characterization of R2F-1

In agreement with similar specific activity shown for R2F-1 and R2F-2, and based on conserved metal coordinating -and tyrosine residues present in both subunits, X-band EPR spectra of R2F-1 and R2F-2 presented in Paper I reveal nearly identical features. Not surprisingly, the EPR spectra of the R2F-1-Fe^{III}₂-Y• and the R2F-2-Fe^{III}₂-Y• strongly resemble the spectrum of R2F-2-Fe^{III}₂-Y• previously characterized by Gräslund and

coworkers (159), which was also characterized by HF-EPR. Based on the latter results, we assume that the Y• in R2F-1 has the same g -tensor components as R2F-2. EPR spectra simulations reveal nearly identical anisotropic hyperfine coupling parameters (hfc), and the dihedral angle, θ , describing the orientation of the α -carbon of the tyrosine ring plane, for the Y• in R2F-1 and R2F-2 is estimated to be around 75° . This is similar to the θ -angle in the previously characterized *M. tuberculosis* R2F-2 and *S. typhimurium* (162). Additionally, rRaman spectroscopy indicates the absence of a hydrogen bond to the tyrosyl-oxygen radical in R2F-1 and R2F-2. The findings in Paper I suggest that R2F-1 and R2F-2 both can function as radical generating subunits in the class Ib RNR in *M. tuberculosis*, with similar activity, supported by nearly identical spectroscopic features of their $\text{Fe}^{\text{III}}_2\text{-Y}\bullet$ cofactors.

B. cereus NrdF and the NrdI-NrdF crystal complex

In Paper II, we have investigated the structural mode of binding between NrdF and NrdI in the class Ib RNR from *B. cereus*, as well as examined the structural features suggested to play a role upon active $\text{Mn}^{\text{III}}_2\text{-Y}\cdot$ cofactor generation in NrdF. Six crystal structures were obtained for this purpose: two structures of $\text{Fe}_2\text{-NrdF}$ in complex with NrdI, $\text{Fe}_2\text{-NrdF}$, $\text{Mn}^{\text{II}}_2\text{-NrdF}$, and two structures of apo-NrdF.

The *B. cereus* NrdI- $\text{Fe}_2\text{-NrdF}$ crystal complex reveals structural similarity as compared to the *E. coli* NrdI- $\text{Mn}^{\text{II}}_2\text{-NrdF}$ crystal complex (97) (with an RMSD value of 1.42 Å calculated for the monomeric NrdI-NrdF complexes) (Figure 12A), suggesting similar binding of NrdI to NrdF in class Ib RNRs. The similar overall interaction between NrdI and NrdF is also supported by the high level of conservation of the amino acids lining the NrdI-NrdF interface (Figure 12B), a general attribute for all class Ib RNRs. These charged and polar residues are suggested to form a hydrophilic solvent channel, connecting the FMN cofactor in NrdI with the di-metal site in NrdF, proposed to serve in the channeling of a hydrophilic oxidant ($\text{O}_2\cdot^-$) needed for generation of the active $\text{Mn}^{\text{III}}_2\text{-Y}\cdot$ cofactor (Figure 12C). The core interface is likely essential for recognition between NrdFs and NrdIs, suggesting that the NrdI-NrdF complex is important for generation of the hydrophilic channel preceding electron transfer. We propose that amino acid differences outside the conserved core region are important for the small variations observed in the NrdI-NrdF binding in *E. coli* and *B. cereus*, where the association is much stronger in *E. coli* than in *Bacillus* species (18,87,95,98). The conserved core interface region is not present in bacterial class Ia NrdB, neither in the eukaryotic R2s.

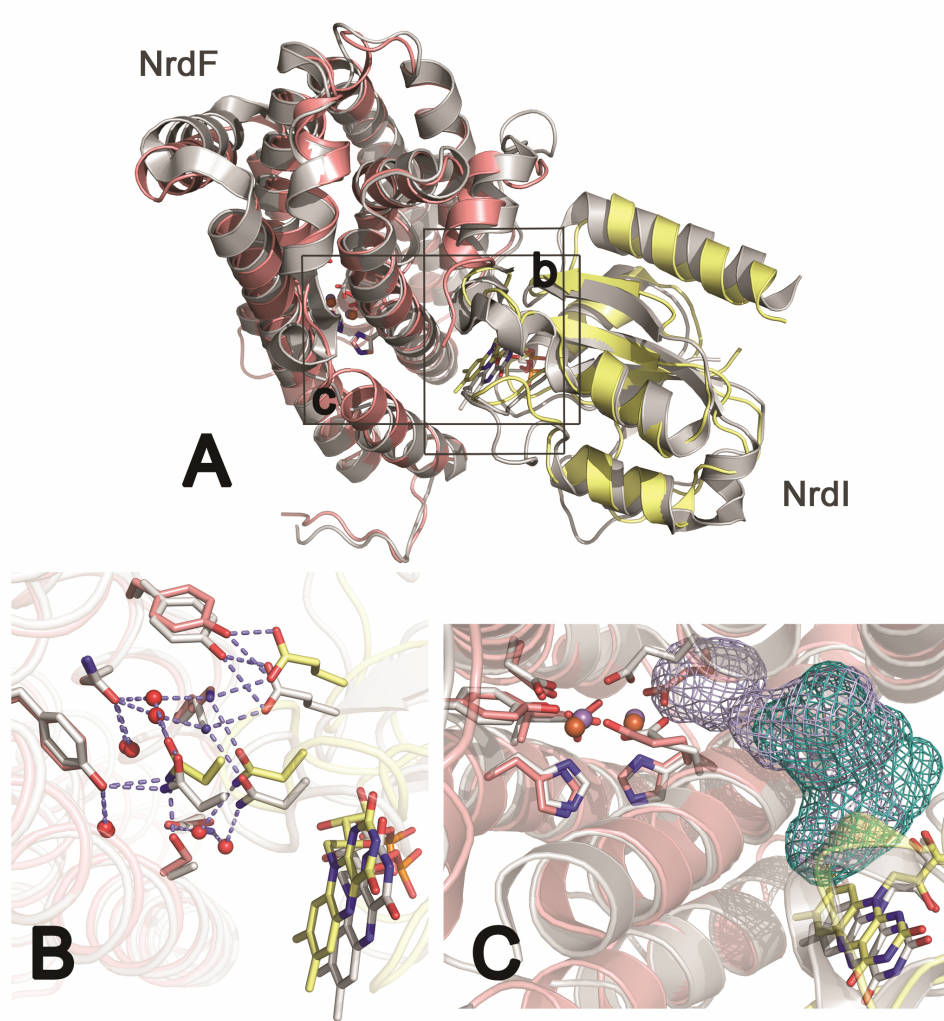


Figure 12. Structure of the NrdI-NrdF complex. (A) Alignment of the overall *B. cereus* and *E. coli* (PDBid:3N39) (97) NrdI-Fe₂-NrdF and NrdI-Mn^{II}₂-NrdF structures, respectively. (B) Alignment of the conserved hydrogen bonding network in the NrdI-NrdF core interface, and the (C) solvent channel connecting the FMN cofactor in NrdI with the di-metal cluster in NrdF, in *B. cereus* and *E. coli*. *B. cereus* NrdI is shown in yellow, NrdF is shown in pink, while the *E. coli* structure is shown in grey. The FMN cofactor, as well as the residues in the active site of NrdF are shown as sticks and colored by atom type. Fe (*B. cereus*) and Mn^{II} (*E. coli*) ions are shown as orange and purple spheres, respectively.

Flexibility of the metal ion coordination environment

In the *E. coli* and *B. cereus* complexes, the proposed solvent channel is structurally conserved, extending from NrdI to the vicinity of metal site 2 in NrdF. However, in the *B. cereus* NrdI-Fe₂-NrdF crystal complex, the channel is prevented from accessing the Fe₂-NrdF metal site due to structural differences in the metal coordination environment, as compared to the *E. coli* NrdI-NrdF complex crystallized with manganese. The access seems to be blocked by the bidentate coordination to metal site 2 by Glu161 (*B. cereus* numbering), observed in both NrdI-Fe₂-NrdF crystal structures (Figure 13), where one of the structures contain alternative Glu161 conformations, likely due to the lower iron occupancy (50%, as compared to 90% for the first structure). The same Glu161 coordination is also observed for the *B. cereus* Fe₂-NrdF structure presented in Paper II (as well as the two apo-NrdF structures), where Glu161 coordinates to Fe2 in a mono- or bidentate fashion (monomers B and A, respectively).

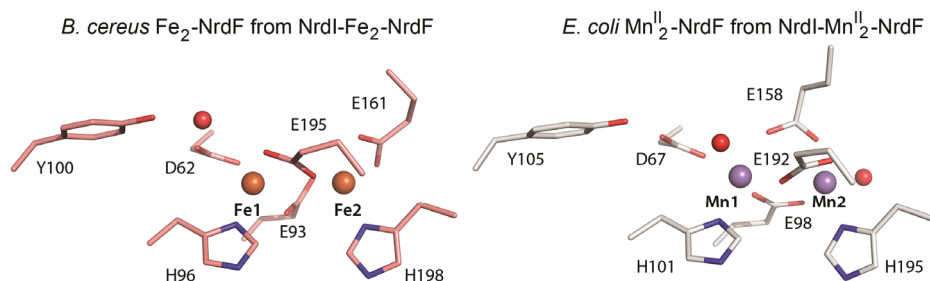


Figure 13. Structures of the Fe₂-NrdF and Mn^{II}₂-NrdF active sites in *B. cereus* and *E. coli* (PDBid:3N39) (97), showing differences in the Glu161 (*B. cereus* numbering) conformation. The bidentate coordination of Glu161 to Fe2 in *B. cereus* occupies the terminal part of the solvent channel. In contrast, the *E. coli* Glu158 bridges both metals in a μ -1,3 fashion, opening up for a water ligand thought to be part of the ordered water network connecting FMN in NrdI to the di-metal site in NrdF (See Figure 12C). The *B. cereus* residues are shown as pink sticks, while the *E. coli* residues are shown in grey.

This feature is consistent with other class Ib NrdF crystal structures, showing the same channel-blocking Glu161 coordination mode. In contrast, crystal structures of the *E. coli* NrdI-Mn^{II}₂-NrdF crystal complex and the Mn^{II}₂-NrdF structure, as well as the *B. cereus* Mn^{II}₂-NrdF structure from Paper II (the latter showing conformational flexibility), show an unusual Glu161 coordination, involving bridging of both metals in a μ -1,3 fashion (Figure

13). This conformation differs from other class Ib NrdF structures, where Glu coordinates to metal site 2 alone. In the case of the *B. cereus* and *E. coli* Mn-containing NrdF structures, the Glu161 conformation opens up for a water coordinating to the Mn2 site and the extended ordered water network connecting the FMN cofactor to the NrdF metal site, facilitating transport of O₂^{•-}. These findings indicate that the movement of Glu161 can be linked to the metal type present in the metal ion site of NrdF, showing flexibility of the Glu161 conformation. The flexibility in key coordinating residues of the NrdF di-metal site suggests that different active site geometries can serve as starting points for metallocofactor activation, where Glu161 seems to specifically distinguish between the different Fe -or Mn containing structures. Similar NrdI binding to NrdF in the *B. cereus* and *E. coli* NrdI-Fe₂-NrdF and NrdI-Mn^{II}₂-NrdF complexes, respectively, suggests the same general binding interface in all class Ib RNRs, independent of metal ion type bound in NrdF.

Assembly of the class Ib holoenzyme

In Paper II, we further report that NrdI-NrdF binding likely affects the formation of the NrdF-NrdE holoenzyme. The *B. cereus* NrdI-NrdF complex supports similar binding between these two proteins in all class Ib RNRs. Based on a structural alignment of the latter structure with the *E. coli* class Ia $\alpha_2\beta_2$ holoenzyme structure (78) (see Figure 6A), we suggest that binding of NrdI to NrdF introduces steric clashes disturbing $\alpha_2\beta_2$ holoenzyme formation. Since studies also support an active $\alpha_2\beta_2$ holoenzyme stoichiometry for the class Ib RNR assembly, the results from Paper II indicate that activation of the Mn^{III}₂-Y• cofactor must occur in an initial stage, prior to NrdF-NrdE interaction in the active R2-R1 complex. Consequently, NrdI would dissociate prior to NrdF binding to NrdE, not interfering with the binding of these subunits. This requirement could possibly explain the inhibitory effect of NrdI present during activity assays performed with Fe-NrdF and NrdE from *E. coli*, in which a tight association between NrdI and NrdF has been reported (18). This association has been shown to be weak in *Bacillus* species, and a similar inhibitory effect of NrdI has not been observed. Hence, the weaker NrdI-NrdF binding in *Bacillus* likely makes NrdF more accessible for NrdE binding. Consequently, these studies also indicate differences in binding strength and the mode of interaction among different species. Moreover, the presence of NrdI does not influence the binding of NrdH-redoxin to NrdE (87,95,98). Further studies are required in the investigation of the class Ib RNR

interactions. The conserved binding interface between NrdIs and NrdFs, as well as NrdFs and NrdEs, could be of great importance related to the development of antimicrobial drugs and class Ib RNR inhibition.

B. cereus BC3987 – a small thioredoxin

NrdH-redoxins, as well as the *B. cereus* BC3987 redoxin, lack the acidic residue similar to Asp26 in *E. coli* and *A. aceti* Trx, believed to participate in deprotonation of the C-terminal cysteine. A phylogenetic analysis performed in Paper III revealed the presence of several conserved residues preceding the C-X-X-C active site motif in Trx-like proteins. These often include highly conserved Asp, Thr and Ser residues, shown to affect the catalytic activity, or proposed to do so. The Cp9, NrdH and BC3987 redoxins all contain a conserved threonine residue, Thr8 (BC3987 numbering), four amino acid residues preceding the active site motif. In Paper III, we have investigated how hydrogen bonding by Thr8 to the deprotonated thiol affects the C-terminal cysteine pK_a value, making the second nucleophilic attack on the substrate possible by these Trx-like proteins. This has been performed through a comparison of the wild type BC3987 with a Thr8Ala mutant protein.

Cysteine pK_a values can be adjusted through hydrogen bonding

The BC3987 wild type and Thr8Ala mutant structures were obtained at high resolution, revealing the typical $\alpha/\beta/\alpha$ Trx fold, as also seen for the *E. coli* (122), *C. ammoniagenes* (163), and *M. tuberculosis* (157) NrdH structures. The C-P-P-C active site motif differs from what is typically observed in Trxs and Grxs. As seen from the crystal structures of BC3987, a Thr53 residue is also found in the proximity of the active site motif, possibly acting as a hydrogen bond donor. It is clear from the structure that the Gln9 amide proton is within hydrogen bonding distance to the Cys15 S_γ -atom. In contrast, the Thr8 residue in the vicinity of the active site motif of the wild type structure shows a different rotamer (Figure 14A), as compared to the previously reported structures of NrdH-redoxins from *E. coli* and *C. ammoniagenes*. In BC3987, the hydroxyl group of Thr8 is pointing away from the buried Cys15 S_γ -atom, stabilized by a nearby water molecule. In the *M. tuberculosis* NrdH structure, Thr8 is present in two alternative conformations, corresponding to the conformations present in both *E. coli* and *C. ammoniagenes* NrdH (40% occupancy), as well as *B. cereus* BC3987 (60% occupancy). In order to investigate whether this Thr8 residue, as well as the Thr53 hydroxyl group, could contribute in

lowering of the buried cysteine pK_a value through hydrogen bonding, QM/MM modeling including the whole protein was performed. Two models of the reduced active site were obtained; Model I, where Thr8 has the same rotamer as seen in the BC3987 crystal structure, pointing away from the buried Cys15 $S\gamma$ -atom; and Model II, where the conformation of Thr8 resembles the rotamers seen in the NrdH-redoxin structures from *E. coli* and *C. ammoniagenes*, pointing towards the buried Cys15 $S\gamma$ -atom (Figure 14B).

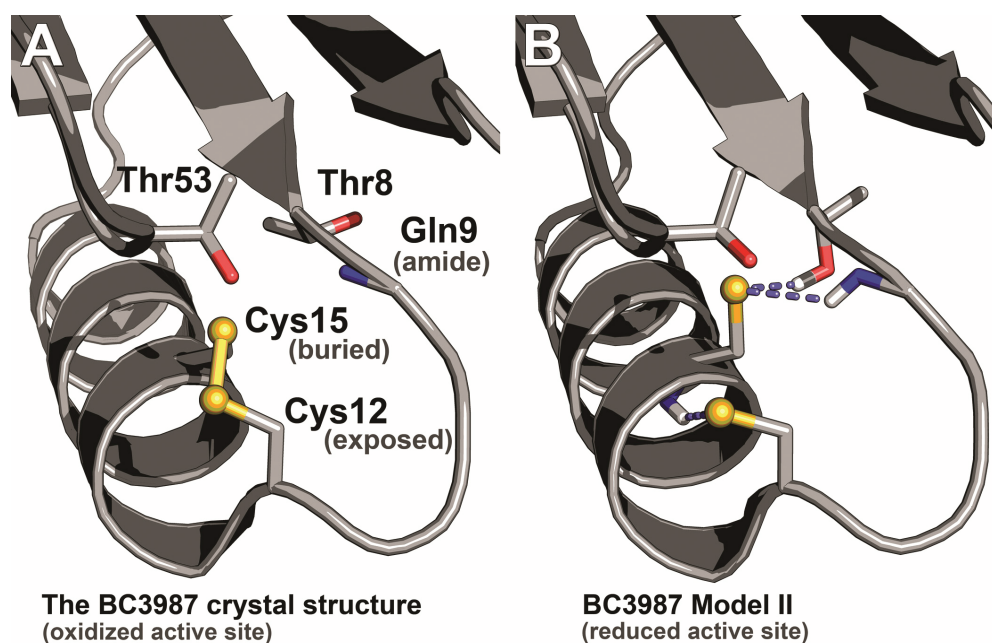


Figure 14. The BC3987 active site environment. (A) Crystal structure of the oxidized active site environment, displaying the C-X-X-C disulfide bridge, Thr8 and Thr53 side chains, and the Gln9 amide. (B) The reduced active site environment from QM/MM Model II, where the Thr8 side chain has been rotated to resemble the rotamer observed in *E. coli* and *C. ammoniagenes* NrdH-redoxins. The Gln9 amide proton and Thr8 hydroxyl group appears to form hydrogen bonds to the C-terminal Cys15 side chain, while the N-terminal Cys12 side chain hydrogen bonds to the Cys15 amide proton.

Both models suggest that the N-terminal Cys12 side chain is hydrogen bonded to the Cys15 amide proton, likely explaining the lowered pK_a value of this thiol, making it suitable to perform the initial nucleophilic attack on the substrate disulfide bond. From both models, it is also clear that the buried Cys15 thiolate can make a hydrogen bond to the

Gln9 amide proton. While the predicted contribution from Thr53 is small in both models, Model II reveals an additional hydrogen bond to the buried cysteine thiolate from Thr8. The calculated pK_a values from Model II for Cys12 and Cys15 are 7.1 and 6.4, respectively, whereas the Cys15 pK_a value calculated from Model I is higher (8.0). These results are compatible with the experimental results from Paper III, where the pK_a values of the active site cysteines were estimated using reduced samples of wild type BC3987 and the Thr8Ala mutant, compared with oxidized references. The pH-titration experiments indicate that the N-terminal Cys12 pK_a value is the same for the wild type and mutant proteins, with a pK_a value of 7.2. In contrast, the wild type BC3987 appears to have a lowered pK_a value for the C-terminal Cys15 thiolate of 5.1, indicating that BC3987 has two thiolates with titratable pK_a values of 7.2 and 5.1, similar to the values calculated from Model II (pK_a values of 7.1 and 6.4). The Thr8Ala mutant, however, was shown to be unstable, leading to protein precipitation at pH values below 5.4, indicating that the Cys15 thiolate behaves differently as compared to the wild type. Paper III also reveals that the wild type BC3987 Trx is a more efficient insulin disulfide reductant as compared to the Thr8Ala mutant. Based on these results, we suggest that the lowered pK_a value of the buried cysteine can be explained through hydrogen bonding to the Thr8 side chain and the Gln9 amide proton. These studies are contrary to what is proposed based on the structural investigation of the *M. tuberculosis* NrdH structure (157), suggesting that the Thr8 OH group can only face the disulfide of the active site motif in the oxidized form, due to lack of space to accommodate the Cys15 thiol group in the reduced form. Based on our results suggesting that the deprotonated thiolate form of Cys15 is stabilized by Thr8 and Gln9, we propose a reaction mechanism (see Figure 7 in Paper III) for BC3987. This mechanism is likely also with respect to other Trx-like proteins lacking the acidic residue analogous to the *E. coli* Trx Asp26. The *B. cereus* BC3987 redoxin has also been shown to promote high catalytic activity in the *B. cereus* and *B. anthracis* Mn-reconstituted class Ib RNR (87).

FUTURE PERSPECTIVES

In order to explain additional aspects regarding the RNR system, studies of the *M. tuberculosis* and *B. cereus* class Ib RNR is ongoing in our group. *B. cereus* contains three annotated FNRs and one TrxR. While the role of TrxR in transferring electrons from NADPH to Trx has been thoroughly studied, the targets of the reducing power provided by the FNRs are not fully established. Preliminary results indicate that one of these FNRs can act as an electron donor for the class Ib RNR protein NrdI. Other FNRs might function as unspecific reductases with other protein partners, such as nitric oxide synthase (NOS). The relationship between the different proteins participating in the class Ib RNR system, such as FNRs, flavodoxins, NrdF and NrdE needs further investigations in order to map the network. Activity assays, as well as extensive thermodynamic characterization using isothermal calorimetry (ITC) are useful tools for describing the interactions between these accessory proteins, as well as NrdF and NrdE in combinations with allosteric effectors and substrates.

A broader understanding of the structural basis of the interactions and specificity between the above mentioned redox partners is further needed. The crystal structure of the NrdI-NrdF complex in Paper II provided interesting knowledge about the association between these proteins. However, such knowledge should also be addressed for other protein partners in the system, in order to understand how these proteins recognize and associate with each other. We are currently working on crystallization trials with several of the above mentioned proteins, where crystallization of protein complexes has been considered crucial. Co-crystallization of different protein complexes will be supplemented with standard biochemical analysis, as well as spectroscopic studies such as UV-vis, rRaman and EPR spectroscopy.

Although the *M. tuberculosis* R2F-1 subunit has been biochemically and spectroscopically characterized in Paper I, there is no crystal structure of R2F-1 available in the PDB database. A crystal structure of R2F-1 would provide useful information about this protein, when compared to the *M. tuberculosis* R2F-2 subunit and other class Ib small subunits. It is also of interest to investigate whether the two small subunits of the *M.*

tuberculosis class Ib are able to generate active $\text{Mn}^{\text{III}}_2\text{-Y}\cdot$ cofactors. Comparisons of the class Ib RNR proteins to the eukaryotic RNR system will be performed, including studies involving the p53R2 subunit (66).

REFERENCES

1. Lehninger, A. L. (1950) Role of metal ions in enzyme systems. *Physiol. Rev.* **30**, 393-429
2. Thomson, A. J., and Gray, H. B. (1998) Bio-inorganic chemistry. *Curr. Opin. Chem. Biol.* **2**, 155-158
3. Kaim, W., Schwederski, B., and Klein, A. (2013) *Bioinorganic chemistry: Inorganic elements in the chemistry of life, an introduction and guide*, John Wiley & Sons, Ltd. ISSN: 1939-5175
4. Lippard, S. J., and Berg, J. M. (1994) *Principles of bioinorganic chemistry*, University Science Books, Mill Valley, CA. ISBN: 0-935702-72-5
5. Cotton, A. F., and Wilkinson, G. (1972) *Advanced inorganic chemistry - a comprehensive text*, Third ed., John Wiley & Sons, Inc. ISBN: 0-471-17560-9
6. Holm, R. H., Kennepohl, P., and Solomon, E. I. (1996) Structural and functional aspects of metal sites in biology. *Chem. Rev.* **96**, 2239-2314
7. Paoli, M., Marles-Wright, J., and Smith, A. (2002) Structure-function relationships in heme-proteins. *DNA Cell Biol.* **21**, 271-280
8. Efimov, I., Basran, J., Thackray, S. J., Handa, S., Mowat, C. G., and Raven, E. L. (2011) Structure and reaction mechanism in the heme dioxygenases. *Biochemistry* **50**, 2717-2724
9. Stoll, S., Shafaat, H. S., Krzystek, J., Ozarowski, A., Tauber, M. J., Kim, J. E., and Britt, R. D. (2011) Hydrogen bonding of tryptophan radicals revealed by EPR at 700 GHz. *J. Am. Chem. Soc.* **133**, 18098-18101
10. Nordlund, P., and Eklund, H. (1995) Di-iron-carboxylate proteins. *Curr. Opin. Struct. Biol.* **5**, 758-766
11. Andersson, K. K., and Gräslund, A. (1995) Diiron-oxygen proteins. *Adv. Inorg. Chem.* **43**, pp 359-408
12. Jordan, A., and Reichard, P. (1998) Ribonucleotide reductases. *Annu. Rev. Biochem.* **67**, 71-98
13. Rosenzweig, A. C., Frederick, C. A., Lippard, S. J., and Nordlund, P. (1993) Crystal-structure of a bacterial nonheme iron hydroxylase that catalyzes the biological oxidation of methane. *Nature* **366**, 537-543

14. Harrison, P. M., and Arosio, P. (1996) Ferritins: Molecular properties, iron storage function and cellular regulation. *Biochim. Biophys. Acta, Bioenergetics.* **1275**, 161-203
15. Hohenberger, J., Ray, K., and Meyer, K. (2012) The biology and chemistry of high-valent iron-oxo and iron-nitrido complexes. *Nat. Commun.* **6**;3:720
16. Kawakami, K., Umena, Y., Kamiya, N., and Shen, J.-R. (2011) Structure of the catalytic, inorganic core of oxygen-evolving photosystem II at 1.9 Å resolution. *J. Photochem. Photobiol.* **104**, 9-18
17. Cox, N., Ogata, H., Stolle, P., Reijerse, E., Auling, G., and Lubitz, W. (2010) A tyrosyl-dimanganese coupled spin system is the native metalloradical cofactor of the R2F subunit of the ribonucleotide reductase of *Corynebacterium ammoniagenes*. *J. Am. Chem. Soc.* **132**, 11197-11213
18. Cotruvo, J. A., and Stubbe, J. (2010) An active dimanganese(III)-tyrosyl radical cofactor in *Escherichia coli* class Ib ribonucleotide reductase. *Biochemistry* **49**, 1297-1309
19. Voevodskaya, N., Lenzian, F., Ehrenberg, A., and Gräslund, A. (2007) High catalytic activity achieved with a mixed manganese-iron site in protein R2 of *Chlamydia* ribonucleotide reductase. *FEBS Lett.* **581**, 3351-3355
20. Jiang, W., Yun, D., Saleh, L., Barr, E. W., Xing, G., Hoffart, L. M., Maslak, M. A., Krebs, C., and Bollinger, J. M. (2007) A manganese(IV)/iron(III) cofactor in *Chlamydia trachomatis* ribonucleotide reductase. *Science* **316**, 1188-1191
21. Voet, D., and Voet, J. G. (2011) *Biochemistry* (4th Ed.), John Wiley & Sons, Inc., USA. ISBN: 978-0470-57095-1
22. Massey, V. (2000) The chemical and biological versatility of riboflavin. *Biochem. Soc. Trans.* **28**, 283-296
23. Cotruvo, J. A., Stich, T. A., Britt, D. R., and Stubbe, J. (2013) Mechanism of assembly of the dimanganese-tyrosyl radical cofactor of class Ib ribonucleotide reductase: Enzymatic generation of superoxide is required for tyrosine oxidation via a Mn(III)Mn(IV) intermediate. *J. Am. Chem. Soc.* **135**, 4027-4039
24. Verkhovskaya, M., and Wikström, M. (2014) Oxidoreduction properties of bound ubiquinone in complex I from *Escherichia coli*. *Biochim. Biophys. Acta, Bioenergetics.* **1837**, 246-250
25. Ritz, D., and Beckwith, J. (2001) Roles of thiol-redox pathways in bacteria. *Annu. Rev. Microbiol.* **55**, 21-48
26. Laurent, T. C., Moore, E. C., and Reichard, P. (1964) Enzymatic synthesis of deoxyribonucleotides. IV. Isolation + characterization of thioredoxin hydrogen donor from *Escherichia coli*. *J. Biol. Chem.* **239**, 3436-3444

27. Holmgren, A., and Sengupta, R. (2010) The use of thiols by ribonucleotide reductase. *Free Radic. Biol. Med.* **49**, 1617-1628
28. Brachet, J. (1933) Recherches sur la synthese de l'acide thymonucleique pendant le developpement de l'oeuf d'oursin. *Arch. Biol.* **44**, 519-576
29. Hammarsten, E., Reichard, P., and Saluste, E. (1950) Pyrimidine nucleosides as precursors of pyrimidines in polynucleotides. *J. Biol. Chem.* **183**, 105-109
30. Reichard, P. (1962) Enzymatic synthesis of deoxyribonucleotides. 1. Formation of deoxycytidine diphosphate from cytidine diphosphate with enzymes from *Escherichia coli*. *J. Biol. Chem.* **237**, 3513-3519
31. Reichard, P. (1968) Biosynthesis of deoxyribonucleotides. *Eur. J. Biochem.* **3**, 259-266
32. Reichard, P. (2010) Ribonucleotide reductases: Substrate specificity by allostery. *Biochem. Biophys. Res. Commun.* **396**, 19-23
33. Reichard, P. (1993) From RNA to DNA, why so many ribonucleotide reductases? *Science* **260**, 1773-1777
34. Andersson, K. K. (ed) (2008) *Ribonucleotide reductase*, Nova Science Publishers, Inc., Hauppauge, NY, USA. ISBN: 978-1-60456-199-9
35. Stubbe, J., Ator, M., and Krenitsky, T. (1983) Mechanism of ribonucleoside diphosphate reductase from *Escherichia-coli* - evidence for 3'-C-H bond-cleavage. *J. Biol. Chem.* **258**, 1625-1631
36. Kolberg, M., Strand, K. R., Graff, P., and Andersson, K. K. (2004) Structure, function, and mechanism of ribonucleotide reductases. *Biochim. Biophys. Acta, Proteins Proteomics* **1699**, 1-34
37. Sintchak, M. D., Arjara, G., Kellogg, B. A., Stubbe, J., and Drennan, C. L. (2002) The crystal structure of class II ribonucleotide reductase reveals how an allosterically regulated monomer mimics a dimer. *Nat. Struct. Biol.* **9**, 293-300
38. Logan, D. T. (2011) Closing the circle on ribonucleotide reductases. *Nat. Struct. Mol. Biol.* **18**, 251-253
39. Cotruvo, J. A., and Stubbe, J. (2011) Class I ribonucleotide reductases: Metallocofactor assembly and repair *in vitro* and *in vivo*. *Annu. Rev. Biochem.* **80**, 733-767
40. Poole, A. M., Logan, D. T., and Sjöberg, B. -M. (2002) The evolution of the ribonucleotide reductases: Much ado about oxygen. *J. Mol. Evol.* **55**, 180-196
41. Raux, E., Schubert, H. L., and Warren, M. J. (2000) Biosynthesis of cobalamin (vitamin B-12): A bacterial conundrum. *Cell. Mol. Life Sci.* **57**, 1880-1893

42. Tamao, Y., and Blakley, R. L. (1973) Cobamides and ribonucleotide reduction. 11. Direct spectrophotometric observation of an intermediate formed from deoxyadenisonecobalamine in ribonucleotide reduction. *Biochemistry* **12**, 24-34
43. Sofia, H. J., Chen, G., Hetzler, B. G., Reyes-Spindola, J. F., and Miller, N. E. (2001) Radical SAM, a novel protein superfamily linking unresolved steps in familiar biosynthetic pathways with radical mechanisms: Functional characterization using new analysis and information visualization methods. *Nucleic Acids Res.* **29**, 1097-1106
44. Røhr, Å. K. (2010) Structural and spectroscopic studies of the flavoprotein NrdI, thioredoxin BC3987, and ribonucleotide reductase diiron-protein R2. *Faculty of Mathematics and Natural Sciences*, University of Oslo. ISSN: 1501-7710 No. 953
45. Tomter, A. B., Zoppellaro, G., Andersen, N. H., Hersleth, H. -P., Hammerstad, M., Røhr, Å. K., Sandvik, G. K., Strand, K. R., Nilsson, G. E., Bell, C. B., Barra, A. L., Blasco, E., Le Pape, L., Solomon, E. I., and Andersson, K. K. (2013) Ribonucleotide reductase class I with different radical generating clusters. *Coord. Chem. Rev.* **257**, 3-26
46. Fairman, J. W., Wijerathna, S. R., Ahmad, M. F., Xu, H., Nakano, R., Jha, S., Prendergast, J., Welin, R. M., Flodin, S., Roos, A., Nordlund, P., Li, Z., Walz, T., and Dealwis, C. G. (2011) Structural basis for allosteric regulation of human ribonucleotide reductase by nucleotide-induced oligomerization. *Nat. Struct. Mol. Biol.* **18**, 316-322
47. Larsson, K. M., Andersson, J., Sjöberg, B. -M., Nordlund, P., and Logan, D. T. (2001) Structural basis for allosteric substrate specificity regulation in anaerobic ribonucleotide reductases. *Structure* **9**, 739-750
48. Nordlund, P., Sjöberg, B. -M., and Eklund, H. (1990) 3-dimensional structure of the free-radical protein of ribonucleotide reductase. *Nature* **345**, 593-598
49. Nordlund, P., and Eklund, H. (1993) Structure and function of the *Escherichia-coli* ribonucleotide reductase protein R2. *J. Mol. Biol.* **232**, 123-164
50. Strand, K. R., Karlsen, S., Kolberg, M., Røhr, Å. K., Gørbitz, C. H., and Andersson, K. K. (2004) Crystal structural studies of changes in the native dinuclear iron center of ribonucleotide reductase protein R2 from mouse. *J. Biol. Chem.* **279**, 46794-46801
51. Solomon, E. I., Brunold, T. C., Davis, M. I., Kemsley, J. N., Lee, S. K., Lehnert, N., Neese, F., Skulan, A. J., Yang, Y. S., and Zhou, J. (2000) Geometric and electronic structure/function correlations in non-heme iron enzymes. *Chem. Rev.* **100**, 235-349
52. Tomter, A. B., Zoppellaro, G., Bell, C. B., Barra, A. L., Andersen, N. H., Solomon, E. I., and Andersson, K. K. (2012) Spectroscopic studies of the iron and manganese

reconstituted tyrosyl radical in *Bacillus cereus* ribonucleotide reductase R2 protein. *PLoS One* **7**, e33436

53. Jordan, A., Pontis, E., Atta, M., Krook, M., Gibert, I., Barbe, J., and Reichard, P. (1994) A 2nd class-I ribonucleotide reductase in *Enterobacteriaceae* - characterization of the *Salmonella typhimurium* enzyme. *Proc. Natl. Acad. Sci. USA* **91**, 12892-12896
54. Huque, Y., Fieschi, F., Torrents, E., Gibert, I., Eliasson, R., Reichard, P., Sahlin, M., and Sjöberg, B. -M. (2000) The active form of the R2F protein of class Ib ribonucleotide reductase from *Corynebacterium ammoniagenes* is a diferric protein. *J. Biol. Chem.* **275**, 25365-25371
55. Högbom, M., Stenmark, P., Voevodskaya, N., McClarty, G., Gräslund, A., and Nordlund, P. (2004) The radical site in chlamydial ribonucleotide reductase defines a new R2 subclass. *Science* **305**, 245-248
56. Roshick, C., Iliffe-Lee, E. R., and McClarty, G. (2000) Cloning and characterization of ribonucleotide reductase from *Chlamydia trachomatis*. *J. Biol. Chem.* **275**, 38111-38119
57. Högbom, M., Galander, M., Andersson, M., Kolberg, M., Hofbauer, W., Lassmann, G., Nordlund, P., and Lendzian, F. (2003) Displacement of the tyrosyl radical cofactor in ribonucleotide reductase obtained by single-crystal high-field EPR and 1.4-Ångström X-ray data. *Proc. Natl. Acad. Sci. USA* **100**, 3209-3214
58. Eriksson, M., Jordan, A., and Eklund, H. (1998) Structure of *Salmonella typhimurium* NrdF ribonucleotide reductase in its oxidized and reduced forms. *Biochemistry* **37**, 13359-13369
59. Borovok, I., Kreisberg-Zakarín, R., Yanko, M., Schreiber, R., Myslovati, M., Aslund, F., Holmgren, A., Cohen, G., and Aharonowitz, Y. (2002) *Streptomyces spp.* contain class Ia and class II ribonucleotide reductases: Expression analysis of the genes in vegetative growth. *Microbiology* **148**, 391-404
60. Jordan, A., Torrents, E., Sala, I., Hellman, U., Gibert, I., and Reichard, P. (1999) Ribonucleotide reduction in *Pseudomonas* species: Simultaneous presence of active enzymes from different classes. *J. Bacteriol.* **181**, 3974-3980
61. Monje-Casas, F., Jurado, J., Prieto-Alamo, M. J., Holmgren, A., and Pueyo, C. (2001) Expression analysis of the *nrdHIEF* operon from *Escherichia coli* - conditions that trigger the transcript level *in vivo*. *J. Biol. Chem.* **276**, 18031-18037
62. Torrents, E., Grinberg, I., Gorovitz-Harris, B., Lundström, H., Borovok, I., Aharonowitz, Y., Sjöberg, B. -M., and Cohen, G. (2007) *nrdR* controls differential expression of the *Escherichia coli* ribonucleotide reductase genes. *J. Bacteriol.* **189**, 5012-5021

63. Huang, M. X., and Elledge, S. J. (1997) Identification of RNR4, encoding a second essential small subunit of ribonucleotide reductase in *Saccharomyces cerevisiae*. *Mol. Cell. Biol.* **17**, 6105-6113
64. Elledge, S. J., and Davis, R. W. (1990) 2 genes differentially regulated in the cell-cycle and by DNA-damaging agents encode alternative regulatory subunits of ribonucleotide reductase. *Genes Dev.* **4**, 740-751
65. Chabes, A., Domkin, V., Larsson, G., Liu, A. M., Gräslund, A., Wijmenga, S., and Thelander, L. (2000) Yeast ribonucleotide reductase has a heterodimeric iron-radical-containing subunit. *Proc. Natl. Acad. Sci. USA* **97**, 2474-2479
66. Guittet, O., Håkansson, P., Voevodskaya, N., Fridd, S., Gräslund, A., Arakawa, H., Nakamura, Y., and Thelander, L. (2001) Mammalian p53R2 protein forms an active ribonucleotide reductase in vitro with the R1 protein, which is expressed both in resting cells in response to DNA damage and in proliferating cells. *J. Biol. Chem.* **276**, 40647-40651
67. Tanaka, H., Arakawa, H., Yamaguchi, T., Shiraishi, K., Fukuda, S., Matsui, K., Takei, Y., and Nakamura, Y. (2000) A ribonucleotide reductase gene involved in a p53-dependent cell-cycle checkpoint for DNA damage. *Nature* **404**, 42-49
68. Yang, F. D., Curran, S. C., Li, L. S., Avarbock, D., Graf, J. D., Chua, M. M., Lui, G. Z., Salem, J., and Rubin, H. (1997) Characterization of two genes encoding the *Mycobacterium tuberculosis* ribonucleotide reductase small subunit. *J. Bacteriol.* **179**, 6408-6415
69. Dawes, S. S., Warner, D. F., Tsenova, L., Timm, J., McKinney, J. D., Kaplan, G., Rubin, H., and Mizrahi, V. (2003) Ribonucleotide reduction in *Mycobacterium tuberculosis*: Function and expression of genes encoding class Ib and class II ribonucleotide reductases. *Infect. Immun.* **71**, 6124-6131
70. Nurbo, J., Roos, A. K., Muthas, D., Wahlström, E., Ericsson, D. J., Lundstedt, T., Unge, T., and Karlen, A. (2007) Design, synthesis and evaluation of peptide inhibitors of *Mycobacterium tuberculosis* ribonucleotide reductase. *J. Pept. Sci.* **13**, 822-832
71. Mowa, M. B., Warner, D. F., Kaplan, G., Kana, B. D., and Mizrahi, V. (2009) Function and regulation of class I ribonucleotide reductase-encoding genes in *Mycobacteria*. *J. Bacteriol.* **191**, 985-995
72. Andersson, C. S., and Högbom, M. (2009) A *Mycobacterium tuberculosis* ligand-binding Mn/Fe protein reveals a new cofactor in a remodeled R2-protein scaffold. *Proc. Natl. Acad. Sci. USA* **106**, 5633-5638
73. Rofougaran, R., Vodnala, M., and Hofer, A. (2006) Enzymatically active mammalian ribonucleotide reductase exists primarily as an $\alpha_6\beta_2$ octamer. *J. Biol. Chem.* **281**, 27705-27711

74. Sjöberg, B. -M. (1997) Ribonucleotide reductases - a group of enzymes with different metallosites and a similar reaction mechanism. *Struct. Bonding* **88**, 139-173
75. Ando, N., Brignole, E. J., Zimanyi, C. M., Funk, M. A., Yokoyama, K., Asturias, F. J., Stubbe, J., and Drennan, C. L. (2011) Structural interconversions modulate activity of *Escherichia coli* ribonucleotide reductase. *Proc. Natl. Acad. Sci. USA* **108**, 21046-21051
76. Hofer, A., Crona, M., Logan, D. T., and Sjöberg, B. -M. (2012) DNA building blocks: Keeping control of manufacture. *Crit. Rev. Biochem. Mol. Biol.* **47**, 50-63
77. Zimanyi, C. M., Ando, N., Brignole, E. J., Asturias, F. J., Stubbe, J., and Drennan, C. L. (2012) Tangled up in knots: Structures of inactivated forms of *E. coli* class Ia ribonucleotide reductase. *Structure* **20**, 1374-1383
78. Uhlin, U., and Eklund, H. (1994) Structure of ribonucleotide reductase protein R1. *Nature* **370**, 533-539
79. Lundin, D., Torrents, E., Poole, A. M., and Sjöberg, B. -M. (2009) RNRdb, a curated database of the universal enzyme family ribonucleotide reductase, reveals a high level of misannotation in sequences deposited to genbank. *BMC Genomics* **10**, 589 (link to database: rnrdb.pfitmap.org)
80. Schimpffweiland, G., Follmann, H., and Auling, G. (1981) A new manganese-activated ribonucleotide reductase found in gram-positive bacteria. *Biochem. Biophys. Res. Commun.* **102**, 1276-1282
81. Willing, A., Follmann, H., and Auling, G. (1988) Nucleotide and thioredoxin specificity of the manganese ribonucleotide reductase from *Brevibacterium ammoniagenes*. *Eur. J. Biochem.* **175**, 167-173
82. Mohamed, S. F., Gvozdiak, O. R., Stallmann, D., Gripenburg, U., Follmann, H., and Auling, G. (1998) Ribonucleotide reductase in *Bacillus subtilis* - evidence for a Mn-dependent enzyme. *Biofactors* **7**, 337-344
83. Cotruvo, J. A., and Stubbe, J. (2011) *Escherichia coli* class Ib ribonucleotide reductase contains a dimanganese(III)-tyrosyl radical cofactor *in vivo*. *Biochemistry* **50**, 1672-1681
84. Zhang, Y., and Stubbe, J. (2011) *Bacillus subtilis* class Ib ribonucleotide reductase is a dimanganese(III)-tyrosyl radical enzyme. *Biochemistry* **50**, 5615-5623
85. Boal, A. K., Cotruvo, J. A., Stubbe, J., and Rosenzweig, A. C. (2012) The dimanganese(II) site of *Bacillus subtilis* class Ib ribonucleotide reductase. *Biochemistry* **51**, 3861-3871

86. Parker, M. J., Zhu, X., and Stubbe, J. (2014) *Bacillus subtilis* class Ib ribonucleotide reductase: High activity and dynamic subunit interactions. *Biochemistry* **53**, 766-776
87. Crona, M., Torrents, E., Røhr, Å. K., Hofer, A., Furrer, E., Tomter, A. B., Andersson, K. K., Sahlin, M., and Sjöberg, B.-M. (2011) NrdH-redoxin protein mediates high enzyme activity in manganese-reconstituted ribonucleotide reductase from *Bacillus anthracis*. *J. Biol. Chem.* **286**, 33053-33060
88. Atkin, C. L., Thelander, L., Reichard, P., and Lang, G. (1973) Iron and free-radical in ribonucleotide reductase - exchange of iron and mössbauer-spectroscopy of protein-B2 subunit of *Escherichia coli* enzyme. *J. Biol. Chem.* **248**, 7464-7472
89. Yun, D., Garcia-Serres, R., Chicalese, B. M., An, Y. H., Huynh, B. H., and Bollinger, J. M., Jr. (2007) (μ -1,2-peroxo)diiron(III/III) complex as a precursor to the diiron(III/IV) intermediate X in the assembly of the iron-radical cofactor of ribonucleotide reductase from mouse. *Biochemistry* **46**, 1925-1932
90. Andersson, M. E., Högbom, M., Rinaldo-Matthis, A., Andersson, K. K., Sjöberg, B. -M., and Nordlund, P. (1999) The crystal structure of an azide complex of the diferrous R2 subunit of ribonucleotide reductase displays a novel carboxylate shift with important mechanistic implications for diiron-catalyzed oxygen activation. *J. Am. Chem. Soc.* **121**, 2346-2352
91. Sturgeon, B. E., Burdi, D., Chen, S. X., Huynh, B. H., Edmondson, D. E., Stubbe, J., and Hoffman, B. M. (1996) Reconsideration of X, the diiron intermediate formed during cofactor assembly in *E-coli* ribonucleotide reductase. *J. Am. Chem. Soc.* **118**, 7551-7557
92. Bollinger, J. M., Edmondson, D. E., Huynh, B. H., Filley, J., Norton, J. R., and Stubbe, J. (1991) Mechanism of assembly of the tyrosyl radical dinuclear iron cluster cofactor of ribonucleotide reductase. *Science* **253**, 292-298
93. Cotruvo, J. A., and Stubbe, J. (2008) NrdI, a flavodoxin involved in maintenance of the diferric-tyrosyl radical cofactor in *Escherichia coli* class Ib ribonucleotide reductase. *Proc. Natl. Acad. Sci. USA* **105**, 14383-14388
94. Roca, I., Torrents, E., Sahlin, M., Gibert, I., and Sjöberg, B. -M. (2008) NrdI essentiality for class Ib ribonucleotide reduction in *Streptococcus pyogenes*. *J. Bacteriol.* **190**, 4849-4858
95. Johansson, R., Torrents, E., Lundin, D., Sprenger, J., Sahlin, M., Sjöberg, B. -M., and Logan, D. T. (2010) High-resolution crystal structures of the flavoprotein NrdI in oxidized and reduced states - an unusual flavodoxin. *FEBS J.* **277**, 4265-4277
96. Røhr, Å. K., Hersleth, H. -P., and Andersson, K. K. (2010) Tracking flavin conformations in protein crystal structures with Raman spectroscopy and QM/MM calculations. *Angew. Chem.-Int. Edit.* **49**, 2324-2327

97. Boal, A. K., Cotruvo, J. A., Stubbe, J., and Rosenzweig, A. C. (2010) Structural basis for activation of class Ib ribonucleotide reductase. *Science* **329**, 1526-1530
98. Tomter, A. B. (2010) Spectroscopic studies of the ribonucleotide reductase R2-subunit from mammals, virus, and bacteria. *Faculty of Mathematics and Natural Sciences*, Univeristy of Oslo. ISSN: 1501-7710 No. 1027
99. Högbom, M., Huque, Y., Sjöberg, B. -M., and Nordlund, P. (2002) Crystal structure of the di-iron/radical protein of ribonucleotide reductase from *Corynebacterium ammoniagenes*. *Biochemistry* **41**, 1381-1389
100. Bianchi, V., Haggardljungquist, E., Pontis, E., and Reichard, P. (1995) Interruption of ferredoxin (flavodoxin) NADP⁺ oxidoreductase gene of *Escherichia coli* does not affect anaerobic growth but increases sensitivity to paraquat. *J. Bacteriol.* **177**, 4528-4531
101. Seo, D., Okabe, S., Yanase, M., Kataoka, K., and Sakurai, T. (2009) Studies of interaction of homo-dimeric ferredoxin-NAD(P)⁺ oxidoreductases of *Bacillus subtilis* and *Rhodospseudomonas palustris*, that are closely related to thioredoxin reductases in amino acid sequence, with ferredoxins and pyridine nucleotide coenzymes. *Biochim. Biophys. Acta, Proteins Proteomics* **1794**, 594-601
102. Wan, J. T., and Jarrett, J. T. (2002) Electron acceptor specificity of ferredoxin (flavodoxin): NADP⁺ oxidoreductase from *Escherichia coli*. *Arch. Biochem. Biophys.* **406**, 116-126
103. Seyedsayamdost, M. R., and Stubbe, J. (2006) Site-specific replacement of Y-356 with 3,4-dihydroxyphenylalanine in the β_2 subunit of *E. coli* ribonucleotide reductase. *J. Am. Chem. Soc.* **128**, 2522-2523
104. Seyedsayamdost, M. R., Yee, C. S., Reece, S. Y., Nocera, D. G., and Stubbe, J. (2006) pH rate profiles of FnY356-R2s (n=2, 3, 4) in *Escherichia coli* ribonucleotide reductase: Evidence that Y356 is a redox-active amino acid along the radical propagation pathway. *J. Am. Chem. Soc.* **128**, 1562-1568
105. Minnihan, E. C., Seyedsayamdost, M. R., Uhlin, U., and Stubbe, J. (2011) Kinetics of radical intermediate formation and deoxynucleotide production in 3-aminotyrosine-substituted *Escherichia coli* ribonucleotide reductases. *J. Am. Chem. Soc.* **133**, 9430-9440
106. Stubbe, J., Nocera, D. G., Yee, C. S., and Chang, M. C. Y. (2003) Radical initiation in the class I ribonucleotide reductase: Long-range proton-coupled electron transfer? *Chem. Rev.* **103**, 2167-2201
107. Bennati, M., Robblee, J. H., Mugnaini, V., Stubbe, J., Freed, J. H., and Borbat, P. (2005) EPR distance measurements support a model for long-range radical initiation in *E. coli* ribonucleotide reductase. *J. Am. Chem. Soc.* **127**, 15014-15015

108. Minnihan, E. C., Nocera, D. G., and Stubbe, J. (2013) Reversible, long-range radical transfer in *E. coli* class Ia ribonucleotide reductase. *Accounts Chem. Res.* **46**, 2524-2535
109. Woersdoerfer, B., Conner, D. A., Yokoyama, K., Livada, J., Seyedsayamdost, M., Jiang, W., Silakov, A., Stubbe, J., Bollinger, J. M., Jr., and Krebs, C. (2013) Function of the diiron cluster of *Escherichia coli* class Ia ribonucleotide reductase in proton-coupled electron transfer. *J. Am. Chem. Soc.* **135**, 8585-8593
110. Berndt, C., Lillig, C. H., and Holmgren, A. (2008) Thioredoxins and glutaredoxins as facilitators of protein folding. *Biochim. Biophys. Acta-Mol. Cell Res.* **1783**, 641-650
111. Fourquet, S., Huang, M. E., D'Autreaux, B., and Toledano, M. B. (2008) The dual functions of thiol-based peroxidases in H₂O₂ scavenging and signaling. *Antioxid. Redox Signal.* **10**, 1565-1575
112. Sevier, C. S., and Kaiser, C. A. (2002) Formation and transfer of disulphide bonds in living cells. *Nat. Rev. Mol. Cell Biol.* **3**, 836-847
113. Holmgren, A. (1988) Thioredoxin and glutaredoxin - small multi-functional redox proteins with active-site disulfide bonds. *Biochem. Soc. Trans.* **16**, 95-96
114. Mulliez, E., Padovani, D., Atta, M., Alcouffe, C., and Fontecave, M. (2001) Activation of class III ribonucleotide reductase by flavodoxin: A protein radical-driven electron transfer to the iron-sulfur center. *Biochemistry* **40**, 3730-3736
115. Andersson, J., Bodevin, S., Westman, M., Sahlin, M., and Sjöberg, B. -M. (2001) Two active site asparagines are essential for the reaction mechanism of the class III anaerobic ribonucleotide reductase from bacteriophage T4. *J. Biol. Chem.* **276**, 40457-40463
116. Carvalho, A. P., Fernandes, P. A., and Ramos, M. J. (2006) Similarities and differences in the thioredoxin superfamily. *Prog. Biophys. Mol. Biol.* **91**, 229-248
117. Lambert, N., and Freedman, R. B. (1985) The latency of rat-liver microsomal protein disulfide-isomerase. *Biochem. J.* **228**, 635-645
118. Hillson, D. A., Lambert, N., and Freedman, R. B. (1984) Formation and isomerization of disulfide bonds in proteins - protein disulfide-isomerase. *Meth. Enzymol.* **107**, 281-294
119. Katti, S. K., Lemaster, D. M., and Eklund, H. (1990) Crystal-structure of thioredoxin from *Escherichia coli* at 1.68 Å resolution. *J. Mol. Biol.* **212**, 167-184
120. Xia, T. H., Bushweller, J. H., Sodano, P., Billeter, M., Björnberg, O., Holmgren, A., and Wüthrich, K. (1992) NMR structure of oxidized *Escherichia coli* glutaredoxin - comparison with reduced *Escherichia coli* glutaredoxin and functionally related proteins. *Protein Sci.* **1**, 310-321

121. Guddat, L. W., Bardwell, J. C. A., Glockshuber, R., HuberWunderlich, M., Zander, T., and Martin, J. L. (1997) Structural analysis of three His32 mutants of DsbA: Support for an electrostatic role of His32 in DsbA stability. *Prot. Sci.* **6**, 1893-1900
122. Stehr, M., Schneider, G., Åslund, F., Holmgren, A., and Lindqvist, Y. (2001) Structural basis for the thioredoxin-like activity profile of the glutaredoxin-like NrdH-redoxin from *Escherichia coli*. *J. Biol. Chem* **276**, 35836-35841
123. Vlamis-Gardikas, A. (2008) The multiple functions of the thiol-based electron flow pathways of *Escherichia coli*: Eternal concepts revisited. *Biochim. Biophys. Acta.* **1780**, 1170-1200
124. Mustacich, D., and Powis, G. (2000) Thioredoxin reductase. *Biochem. J.* **346** 1-8
125. Pan, J. L., and Bardwell, J. C. (2006) The origami of thioredoxin-like folds. *Protein Sci.* **15**, 2217-2227
126. Martin, J. L. (1995) Thioredoxin - a fold for all reasons. *Structure* **3**, 245-250
127. Holmgren, A., Söderberg, B. O., Eklund, H., and Branden, C. I. (1975) 3-dimensional structure of *Escherichia coli* thioredoxin-S2 to 2.8 Å resolution. *Proc. Natl. Acad. Sci. USA* **72**, 2305-2309
128. Holmgren, A. (1976) Hydrogen donor system for *Escherichia-coli* ribonucleoside-diphosphate reductase dependent upon glutathione. *Proc. Natl. Acad. Sci. USA* **73**, 2275-2279
129. Eklund, H., Ingelman, M., Söderberg, B. O., Uhlin, T., Nordlund, P., Nikkola, M., Sonnerstam, U., Joelson, T., and Petratos, K. (1992) Structure of oxidized bacteriophage-T4 glutaredoxin (thioredoxin) - refinement of native and mutant proteins. *J. Mol. Biol.* **228**, 596-618
130. Miranda-Vizuete, A., Damdimopoulos, A. E., Gustafsson, J. A., and Spyrou, G. (1997) Cloning, expression, and characterization of a novel *Escherichia coli* thioredoxin. *J. Biol. Chem.* **272**, 30841-30847
131. Holmgren, A. (1979) Glutathione-dependent synthesis of deoxyribonucleotides - characterization of the enzymatic mechanism of *Escherichia coli* glutaredoxin. *J. Biol. Chem.* **254**, 3672-3678
132. Holmgren, A. (1979) Glutathione-dependent synthesis of deoxyribonucleotides - purification and characterization of glutaredoxin from *Escherichia coli*. *J. Biol. Chem.* **254**, 3664-3671
133. Zeller, T., and Klug, G. (2006) Thioredoxins in bacteria: Functions in oxidative stress response and regulation of thioredoxin genes. *Naturwissenschaften* **93**, 259-266

134. Meyer, Y., Buchanan, B. B., Vignols, F., and Reichheld, J. P. (2009) Thioredoxins and glutaredoxins: Unifying elements in redox biology. *Annu. Rev. Genet.* **43**, 335-367
135. Carmel-Harel, O., and Storz, G. (2000) Roles of the glutathione- and thioredoxin-dependent reduction systems in the *Escherichia coli* and *Saccharomyces cerevisiae* responses to oxidative stress. *Annu. Rev. Microbiol.* **54**, 439-461
136. Chivers, P. T., and Raines, R. T. (1997) General acid/base catalysis in the active site of *Escherichia coli* thioredoxin. *Biochemistry* **36**, 15810-15816
137. Foloppe, N., and Nilsson, L. (2004) The glutaredoxin -C-P-Y-C- motif: Influence of peripheral residues. *Structure* **12**, 289-300
138. Shi, J., Vlamis-Gardikas, V., Åslund, F., Holmgren, A., and Rosen, B. P. (1999) Reactivity of glutaredoxins 1, 2, and 3 from *Escherichia coli* shows that glutaredoxin 2 is the primary hydrogen donor to ArsC-catalyzed arsenate reduction. *J. Biol. Chem.* **274**, 36039-36042
139. Fernandes, A. P., Fladvad, M., Berndt, C., Andresen, C., Lillig, C. H., Neubauer, P., Sunnerhagen, M., Holmgren, A., and Vlamis-Gardikas, A. (2005) A novel monothiol glutaredoxin (Grx4) from *Escherichia coli* can serve as a substrate for thioredoxin reductase. *J. Biol. Chem.* **280**, 24544-24552
140. Leitung, W. U., and Jianping, X. I. E. (2010) Comparative genomics analysis of *Mycobacterium* NrdH-redoxins. *Microb. Pathog.* **48**, 97-102
141. Martin, J. L., Bardwell, J. C. A., and Kuriyan, J. (1993) Crystal-structure of the DsbA protein required for disulfide bond formation *in vivo*. *Nature* **365**, 464-468
142. Edman, J. C., Ellis, L., Blacher, R. W., Roth, R. A., and Rutter, W. J. (1985) Sequence of protein disulfide isomerase and implications of its relationship to thioredoxin. *Nature* **317**, 267-270
143. Åslund, F., Berndt, K. D., and Holmgren, A. (1997) Redox potentials of glutaredoxins and other thiol-disulfide oxidoreductases of the thioredoxin superfamily determined by direct protein-protein redox equilibria. *J. Biol. Chem.* **272**, 30780-30786
144. Mössner, E., Huber-Wunderlich, M., and Glockshuber, R. (1998) Characterization of *Escherichia coli* thioredoxin variants mimicking the active-sites of other thiol/disulfide oxidoreductases. *Protein Sci.* **7**, 1233-1244
145. Krause, G., Lundström, J., Barea, J. L., Delacuesta, C. P., and Holmgren, A. (1991) Mimicking the active-site of protein disulfide-isomerase by substitution of proline 34 in *Escherichia coli* thioredoxin. *J. Biol. Chem.* **266**, 9494-9500
146. Hol, W. G. J. (1985) The role of the alpha-helix dipole in protein function and structure. *Prog. Biophys. Mol. Biol.* **45**, 149-195

147. Tanford, C., and Kirkwood, J. G. (1957) Theory of protein titration curves. 1. General equations for impenetrable spheres. *J. Am. Chem. Soc.* **79**, 5333-5339
148. Jensen, J. H., Li, H., Robertson, A. D., and Molina, P. A. (2005) Prediction and rationalization of protein pK_a values using QM and QM/MM methods. *J. Phys. Chem.* **109**, 6634-6643
149. Li, H., Robertson, A. D., and Jensen, J. H. (2005) Very fast empirical prediction and rationalization of protein pK_a values. *Proteins* **61**, 704-721
150. Roos, G., Loverix, S., and Geerlings, P. (2006) Origin of the pK_a perturbation of N-terminal cysteine in alpha- and 3(10)-helices: A computational DFT study. *J. Phys. Chem. B* **110**, 557-562
151. Chivers, P. T., Prehoda, K. E., Volkman, B. F., Kim, B. M., Markley, J. L., and Raines, R. T. (1997) Microscopic pK_a values of *Escherichia coli* thioredoxin. *Biochemistry* **36**, 14985-14991
152. Eklund, H., Gleason, F. K., and Holmgren, A. (1991) Structural and functional relations among thioredoxins of different species. *Protein Struct. Funct. Genet.* **11**, 13-28
153. Starks, C. M., Francois, J. A., MacArthur, K. M., Heard, B. Z., and Kappock, T. J. (2007) Atomic-resolution crystal structure of thioredoxin from the acidophilic bacterium *Acetobacter aceti*. *Protein Sci.* **16**, 92-98
154. Dyson, H. J., Jeng, M. F., Tennant, L. L., Slaby, I., Lindell, M., Cui, D. S., Kuprin, S., and Holmgren, A. (1997) Effects of buried charged groups on cysteine thiol ionization and reactivity in *Escherichia coli* thioredoxin: Structural and functional characterization of mutants of Asp 26 and Lys 57. *Biochemistry* **36**, 2622-2636
155. Kallis, G. B., and Holmgren, A. (1980) Differential reactivity of the functional sulfhydryl-groups of cysteine-32 and cysteine-35 present in the reduced form of thioredoxin from *Escherichia coli*. *J. Biol. Chem.* **255**, 261-265
156. Rabinovitch, I., Yanku, M., Yeheskel, A., Cohen, G., Borovok, I., and Aharonowitz, Y. (2010) *Staphylococcus aureus* NrdH redoxin is a reductant of the class Ib ribonucleotide reductase. *J. Bacteriol.* **192**, 4963-4972
157. Phulera, S., and Mande, S. C. (2013) The crystal structure of *Mycobacterium tuberculosis* NrdH at 0.87 Å suggests a possible mode of its activity. *Biochemistry* **52**, 4056-4065
158. Reynolds, C. M., Meyer, J., and Poole, L. B. (2002) An NADH-dependent bacterial thioredoxin reductase-like protein in conjunction with a glutaredoxin homologue form a unique peroxiredoxin (AhpC) reducing system in *Clostridium pasteurianum*. *Biochemistry* **41**, 1990-2001

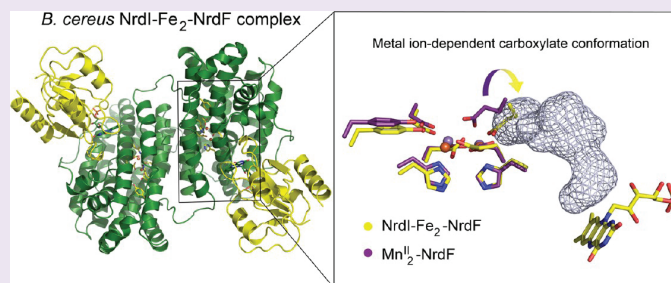
159. Liu, A., Potsch, S., Davydov, A., Barra, A. L., Rubin, H., and Gräslund, A. (1998) The tyrosyl free radical of recombinant ribonucleotide reductase from *Mycobacterium tuberculosis* is located in a rigid hydrophobic pocket. *Biochemistry* **37**, 16369-16377
160. Davydov, A., Liu, A. M., and Gräslund, A. (2000) EPR evidence of two structurally different diferric sites in *Mycobacterium tuberculosis* R2-2 ribonucleotide reductase protein. *J. Inorg. Biochem.* **80**, 213-218
161. Liu, A. M., Barra, A. L., Rubin, H., Lu, G. Z., and Gräslund, A. (2000) Heterogeneity of the local electrostatic environment of the tyrosyl radical in *Mycobacterium tuberculosis* ribonucleotide reductase observed by high-field electron paramagnetic resonance. *J. Am. Chem. Soc.* **122**, 1974-1978
162. Allard, P., Barra, A. L., Andersson, K. K., Schmidt, P. P., Atta, M., and Gräslund, A. (1996) Characterization of a new tyrosyl free radical in *Salmonella typhimurium* ribonucleotide reductase with EPR at 9.45 and 245 GHz. *J. Am. Chem. Soc.* **118**, 895-896
163. Stehr, M., and Lindqvist, Y. (2004) NrdH-redoxin of *Corynebacterium ammoniagenes* forms a domain-swapped dimer. *Protein Struct. Funct. Bioinf.* **55**, 613-619

Crystal Structure of *Bacillus cereus* Class Ib Ribonucleotide Reductase Di-iron NrdF in Complex with NrdI

Marta Hammerstad, Hans-Petter Hersleth,* Ane B. Tomter, Åsmund K. Røhr, and K. Kristoffer Andersson

Department of Biosciences, University of Oslo, P.O. Box 1066, Blindern, NO-0316 Oslo, Norway

Supporting Information



ABSTRACT: Class Ib ribonucleotide reductases (RNRs) use a dimetal-tyrosyl radical (Y●) cofactor in their NrdF (β_2) subunit to initiate ribonucleotide reduction in the NrdE (α_2) subunit. Contrary to the diferric tyrosyl radical (Fe^{III}₂-Y●) cofactor, which can self-assemble from Fe^{II}₂-NrdF and O₂, generation of the Mn^{III}₂-Y● cofactor requires the reduced form of a flavoprotein, NrdI_{h₉}, and O₂ for its assembly. Here we report the 1.8 Å resolution crystal structure of *Bacillus cereus* Fe₂-NrdF in complex with NrdI. Compared to the previously solved *Escherichia coli* NrdI-Mn^{II}₂-NrdF structure, NrdI and NrdF binds similarly in *Bacillus cereus* through conserved core interactions. This protein–protein association seems to be unaffected by metal ion type bound in the NrdF subunit. The *Bacillus cereus* Mn^{II}₂-NrdF and Fe₂-NrdF structures, also presented here, show conformational flexibility of residues surrounding the NrdF metal ion site. The movement of one of the metal-coordinating carboxylates is linked to the metal type present at the dimetal site and not associated with NrdI-NrdF binding. This carboxylate conformation seems to be vital for the water network connecting the NrdF dimetal site and the flavin in NrdI. From these observations, we suggest that metal-dependent variations in carboxylate coordination geometries are important for active Y● cofactor generation in class Ib RNRs. Additionally, we show that binding of NrdI to NrdF would structurally interfere with the suggested $\alpha_2\beta_2$ (NrdE-NrdF) holoenzyme formation, suggesting the potential requirement for NrdI dissociation before NrdE-NrdF assembly after NrdI-activation. The mode of interactions between the proteins involved in the class Ib RNR system is, however, not fully resolved.

Ribonucleotide reductases (RNRs) catalyze the conversion of ribonucleotides to their corresponding deoxyribonucleotides in all living organisms, providing the essential building blocks required for DNA replication and repair.^{1,2} Class I RNRs consist of two homodimeric subunits: α_2 and β_2 . Nucleotide reduction is initiated through the reversible one-electron oxidation of a conserved cysteine residue to a thiyl radical in the α_2 subunits, initiated by a dinuclear metallocofactor and tyrosyl radical positioned in the β_2 subunits.³ Three subclasses of the class I enzymes have been characterized based on their metal ion composition and sequence: Ia, Ib, and Ic.⁴ The class Ia RNRs are found in eukaryotes, some viruses, and some prokaryotes such as *Escherichia coli* (*Ec*) (the latter also containing the class Ib RNR), supplying deoxyribonucleotides during normal aerobic growth.^{5,5} Enzyme activity requires a μ -oxo-bridged diferric tyrosyl radical (Fe^{III}₂-Y●) cofactor localized in the β_2 subunit (NrdB/R2).⁶ The cofactor can be formed by self-assembly from apo-NrdB in the presence of Fe^{II} and O₂, forming the Y● required for dNDP formation in the α_2 subunits

(NrdA/R1).⁷ The class Ic RNR has so far been well characterized only in the obligate intracellular pathogen *Chlamydia trachomatis*. Subsequent studies have shown that its β_2 subunit utilizes a stable, heterodinuclear Mn^{IV}Fe^{III} cofactor to initiate catalysis.^{8–11} Class Ib RNRs are the primary sources of dNTPs for a wide variety of prokaryotes, such as *Mycobacterium tuberculosis* (*Mt*), *Corynebacterium ammoniagenes* (*Ca*), *Bacillus anthracis* (*Ba*), *Bacillus subtilis* (*Bs*), and *Bacillus cereus* (*Bc*).¹² The class Ib enzymes consist of the α_2 (NrdE/R1E) and β_2 (NrdF/R2F) subunits,¹³ where the active form in both class Ia and class Ib is believed to comprise an $\alpha_2\beta_2$ stoichiometry.^{14,15} The metallocofactor required for activity in class Ib RNRs has for several decades been known to consist of an Fe^{III}₂-Y● cofactor, assembled *in vitro* similarly to the class Ia

Received: June 17, 2013

Accepted: December 2, 2013

Published: December 2, 2013

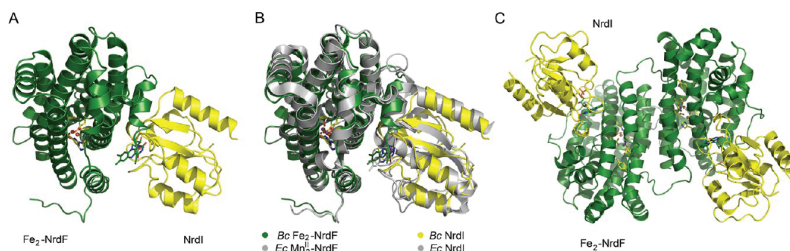


Figure 1. Structure of the NrdI-NrdF complex. (A) The overall structure of the *Bc* NrdI-Fe₂-NrdF complex and (B) alignment of the *Bc* and *Ec* (PDB id: 3N39) NrdI-Fe₂-NrdF and NrdI-Mn^{II}-NrdF complexes, respectively. (C) The dimeric *Bc* NrdI-Fe₂-NrdF complex, represented by the monomeric *Bc* NrdI-Fe₂-NrdF (asymmetric unit) shown with its symmetry equivalent molecule. The FMN cofactor in NrdI and the residues in the active site of NrdF are represented as sticks and colored by atom type in *Bc* and colored gray in *Ec*. Fe ions are shown as orange spheres (*Bc*), and Mn^{II} ions are shown as purple spheres (*Ec*).

enzymes.^{16,17} However, recent studies have shown that the class Ib NrdF can also utilize an active Mn^{III}-Y• cofactor for nucleotide reduction.^{18–20} The Mn^{III}-Y• cofactor can only be generated from the dimanganese(II) site (Mn^{II}₂) in a self-assembly process in the presence of O₂ and the flavodoxin-like protein NrdI.¹⁸ NrdI is found in all organisms with genomes coding for the class Ib RNR²¹ and contains a flavin mononucleotide cofactor (FMN), demonstrated to be able to act as a two-electron reductant.^{22,23} It has been proposed that NrdI, in its fully reduced hydroquinone form (NrdI_{h₄} containing FMNH⁻), reacts with O₂ providing the oxidant, H₂O₂ or O₂•⁻, required for generation of the active Mn^{III}-Y• cofactor.^{24–26} Studies have shown that the Mn^{III}-Y• cofactor can be formed both *in vitro* and *in vivo*,^{20,24} and that the manganese form of the enzyme has a higher specific activity compared to the iron form, as in the case of *Ba*,²⁷ *Bc*,²⁸ and *Bs*,²⁹ all showing a 10-fold difference. It is still not understood how the *in vitro* process of cofactor assembly using identical metal coordinating ligands, but different metals and oxidants,³⁰ is controlled *in vivo*. Structural studies of *Ec* NrdF both in the Fe^{III}₂ and Mn^{III}₂ forms, as well as of the crystal structure of the Mn^{II}₂-NrdF in complex with NrdI, give insight into Y• generation in NrdF.²⁵ The metal-binding residues are identical in most class Ia and Ib RNRs, where the dimetal clusters are coordinated by four carboxylates and two histidines.³¹ The coordination environment in structures of *Ec* Mn^{II}₂-NrdF and NrdI-NrdF complexes revealed an unusual structural feature involving Glu158 (*Ec* numbering), showing bridging of both metals in a μ -1,3 fashion.²⁵ This carboxylate conformation observed in the *Ec* structures is different from other reported RNR class I structures, where the corresponding Glu coordinates to metal site 2 alone. In these structures, Glu occupies the site of a Mn2 water ligand thought to be part of an ordered water network facilitating transport of the reactive oxidant from the NrdI flavin cofactor to the NrdF metal site, required for the generation of the Mn^{III}-Y• cofactor.¹⁸

Here, we present the first crystal structure of the *Bc* class Ib NrdF in complex with the flavoprotein NrdI. In this 1.8 Å resolution crystal structure, the *Bc* NrdF is in the Fe₂ form, and the Glu161 (*Bc* numbering) coordinates to only metal site 2, as seen for most class Ib NrdF structures. This is in contrast to what was observed in the *Ec* Mn^{II}₂-NrdF and NrdI-Mn^{II}₂-NrdF structures, where Glu bridges both metals in a μ -1,3 fashion opening up for an ordered water network to the FMN site. In both the *Bc* NrdI-Fe₂-NrdF and Fe₂-NrdF structures, this water network and channel is blocked by the bidentate coordination

of Glu161 only to the Fe2 site. However, in the *Bc* Mn^{II}₂-NrdF crystal structure, also presented here, Glu161 shows variations in this carboxylate conformation, with one conformation bridging both metals in a μ -1,3 fashion, revealing the water network. The carboxylate variations in the different NrdI-NrdF complexes, as well as NrdF structures, indicate that flexibility in coordinating amino acids is possible, almost in a gating fashion, and is likely important for metal cofactor and tyrosyl radical generation.

RESULTS AND DISCUSSION

In this work, we present six crystal structures of the *Bc* class Ib RNR small subunit NrdF, including two structures of NrdF in complex with NrdI (NrdI-NrdF-1 and -2), Fe₂-NrdF, Mn^{II}₂-NrdF, and two structures of apo-NrdF (apo-NrdF-1 and -2).

Overall Structure of the *Bc* Fe₂-NrdF, Mn^{II}₂-NrdF, and NrdI-NrdF Complex. Both the 2.1 Å (NrdI-NrdF-1) and 1.8 Å (NrdI-NrdF-2) resolution crystal structures of *Bc* NrdI-NrdF were obtained by co-crystallizing NrdF with an equimolar amount of NrdI. The asymmetric unit contains one monomer of NrdI in complex with one monomer of NrdF, in which the overall architecture strongly resembles the *Ec* NrdI-NrdF structure reported earlier by Boal et al.²⁵ The overall structure of the 2.1 Å resolution *Bc* NrdI-NrdF protein complex is shown in Figure 1A and C, while a structural alignment of the *Bc* and *Ec* NrdI-NrdF complexes is shown in Figure 1B and Supplementary Figure S1. Structural similarity between the *Bc* and *Ec* monomeric NrdI-NrdF complexes has been calculated to an RMSD value of 1.42 Å, while structural similarity between the dimeric NrdI-NrdF structures have an RMSD of 1.78 Å. The RMSDs for the *Bc* and *Ec* NrdF and NrdI structures individually (from the crystal complexes) are 1.23 and 1.05 Å, respectively. This shows that the NrdF and NrdI bind similarly to each other in *Ec* and *Bc*, but with some small structural variations (see below). The final model for NrdI-NrdF-1 consists of residues 1–290 out of 322 in NrdF and residues 1–117 out of 119 in NrdI and are refined to final $R_{\text{work}}/R_{\text{free}}$ values of 17.7%/23.3%. The NrdI-NrdF-2 structure consists of residues 1–290 in NrdF and 1–118 in NrdI and are refined to final $R_{\text{work}}/R_{\text{free}}$ values of 16.7%/20.9%. Both the NrdI-NrdF and the different NrdF structures show well-defined electron density for the modeled residues. The 2.1 and 1.9 Å resolution crystal structures of *Bc* Fe₂-NrdF and Mn^{II}₂-NrdF, respectively, contain two molecules in the asymmetric unit, with the final models consisting of residues 1–287 out of 322 in monomers A

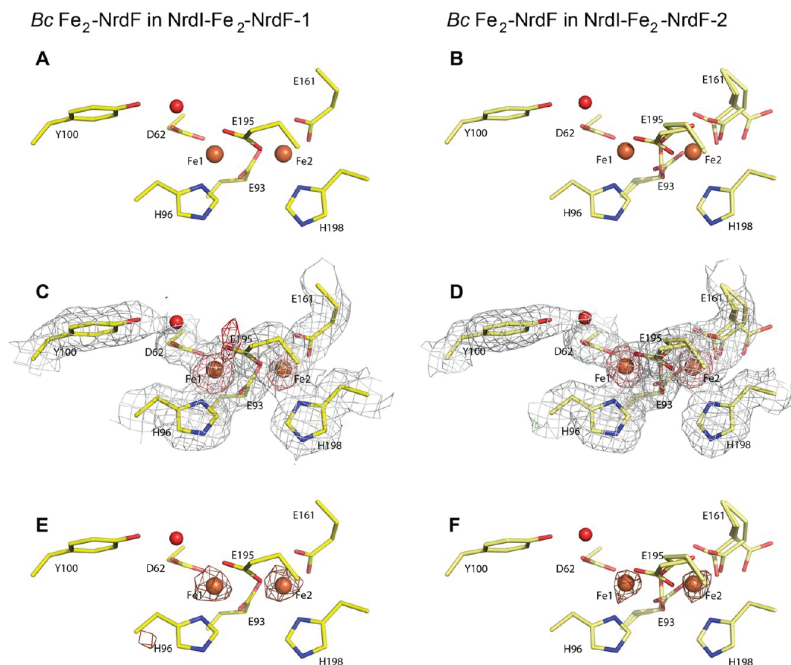


Figure 2. Metal ion sites in the two *Bc* NrdI-Fe₂-NrdF complex structures. (A, C, and E) The metal site in NrdI-Fe₂-NrdF-1 and (B, D, and F) the metal site in NrdI-Fe₂-NrdF-2. The Fe ions are shown as orange spheres, and the coordinating amino acids and Tyr100 are represented as sticks and colored by atom type. In panels C and D, the $2F_o - F_c$ electron density map (gray) is contoured at 1σ , while the $F_o - F_c$ map is shown as green mesh (3σ) and red mesh (-3σ). The omit map surrounding the Fe ions is contoured at 6σ (salmon). The Fe ions are modeled with 90% (C) and 50% (D) occupancy. For panels E and F, anomalous maps are included, contoured at 3.5σ (brown).

and B for both structures. The structures are refined to final $R_{\text{work}}/R_{\text{free}}$ values of 18.5%/23.5% and 21.0%/26.0%, respectively. The two *Bc* apo-NrdF structures belong to different crystal forms. Apo-NrdF-2 (2.0 Å) belongs to space group $P2_1$ as the *Bc* Fe/Mn-NrdF structures and contains residues 1–287/1–288 for the two monomers with final $R_{\text{work}}/R_{\text{free}}$ values of 20.8%/26.0%. Apo-NrdF-1 (2.2 Å) belongs to space group $C2$, also consisting of two monomers, and was refined to final $R_{\text{work}}/R_{\text{free}}$ values of 17.6%/24.3%. The overall structure of *Bc* NrdF in the different NrdI-NrdF and NrdF structures presented here are very similar (Supplementary Figure S2A). However, residues 26–31 in NrdI-NrdF-1 and monomer B of apo-NrdF-1 have a more helical conformation compared to the other structures (Supplementary Figure S2C and D). Due to a different crystal packing, 13 more residues of the flexible C-terminal end were built into the electron density of monomer A of apo-NrdF-1 (Supplementary Figure S2B), with the two resulting monomers containing residues 1–300/1–287, respectively. These additionally built in residues point into the area where interaction with NrdE is suggested,¹⁴ indicating that the flexible C-terminal could become ordered through interaction with NrdE.

Structure and Coordination Environment of the Crystal Complex Metal Cluster Site. The overall structure of the metal cluster coordination site in the *Bc* NrdI-NrdF structure strongly resembles other class Ib NrdF structures,^{13,19,30,32,33} except for the *Ec* Mn^{II}₂-NrdFs²⁵ and the *Bc*

Mn^{II}-NrdF presented in this paper. Both *Bc* NrdI-NrdF complex structures have been obtained with iron in the NrdF dimetal sites (Figure 2). For the NrdI-Fe₂-NrdF-1 structure modeled with 90% iron occupancy, the Fe sites are four- and five-coordinated, respectively, with an Fe–Fe distance of 3.9 Å, Glu195 in a μ -1,3 coordination, and Glu161 bidentate to Fe2 (Figure 2A, C, and E). The coordination and the long Fe–Fe distance is consistent with previously reported ferrous (Fe^{II}) iron NrdF/B structures.^{13,19,30,32,33} The Fe omit map shown in Figure 2C and D and the anomalous difference map at 1.0 Å wavelength confirm the presence of metals in the di-Fe sites (Figure 2E and F). In the 1.8 Å NrdI-Fe₂-NrdF-2 structure, similar coordination and Fe–Fe distance is observed; however, additional alternative conformations are modeled for Glu195, Glu93, and Glu161 (Figure 2B, D, and F). This could partly be due to the lower iron occupancy in the di-Fe sites (50%). The X-ray doses absorbed by the different crystals in this study (Table 1) are within the recommended Henderson limit of 20 MGy to avoid considerable radiation damage of protein crystals.³⁴ Nevertheless, X-ray induced radiation damage of metal sites occurs on a much shorter time scale.³⁵ Studies on RNR have shown a fast reduction of the oxidized metal ion states;^{36,37} however, the structures presented here are considered to already be in the reduced states, and therefore X-ray induced changes are limited.

***Bc* Fe₂-NrdF Coordination Environment.** The crystal structure of the dimeric *Bc* Fe₂-NrdF has been modeled with

Table 1. Data Collection and Refinement Statistics

	<i>Bc</i> Mn ^{II} ₂ -NrdF	<i>Bc</i> Fe ₂ -NrdF	<i>Bc</i> NrdI-NrdF-1	<i>Bc</i> NrdI-NrdF-2
	Crystal Data			
space group	P2 ₁	P2 ₁	C222 ₁	C222 ₁
<i>a</i> , <i>b</i> , <i>c</i> (Å)	61.9/49.2/98.5	62.0/49.3/98.5	59.3/125.0/142.6	59.5/124.7/141.3
α , β , γ (deg)	90.0/107.2/90.0	90.0/107.2/90.0	90.0/90.0/90.0	90.0/90.0/90.0
crystal size (μm^3)	40 × 100 × 200	40 × 100 × 200	75 × 75 × 200	100 × 100 × 200
	Data Collection			
X-ray source	ESRF-ID29	ESRF-ID29	ESRF-ID29	SLS-PXII-X10SA
wavelength (Å)	0.9724	0.9724	0.9763	0.9999
flux (photons/s)	1660 × 10 ⁹	1600 × 10 ⁹	75 × 10 ⁹	225 × 10 ⁹
beam size (μm^2)	30 × 50	30 × 50	30 × 50	100 × 100
total exposure (s)	19	30	150	120
absorbed X-ray dose (MGy)	7.4	11.3	2.4	1.0
resolution range (Å)	47.0–1.9/2.0–1.9	47.0–2.1/2.2–2.1	62.5–2.1/2.2–2.1	53.7–1.8/1.9–1.8
temperature (K)	100	100	100	100
completeness (%) ^a	90.4/92.9	88.7/84.9	98.5/98.9	98.2/99.3
redundancy ^a	2.1/2.1	2.8/2.7	3.9/3.9	4.1/4.1
<i>I</i> / σ (<i>I</i>) ^a	11.3/2.1	5.7/2.7	8.6/2.8	11.3/2.9
<i>R</i> _{sym} ^{a,b}	10.7/37.9	10.1/30.1	9.5/43.7	5.9/45.0
	Refinement Statistics			
<i>R</i> _{work} (%) ^c	18.4	21.0	17.7	16.7
<i>R</i> _{free} (%) ^d	23.4	26.0	23.3	20.9
	Model Content			
amino acids	574	574	407	408
Fe ions (occupancy)	-	4 (100%)	2 (90%)	2 (50%)
Mn ions (occupancy)	4(100,90,100,100%)	-	-	-
Cl ⁻ ions	-	-	1	5
water molecules	166	61	117	196
FMN cofactors	-	-	1	1
molecules per asu	2	2	1 + 1	1 + 1
solvent content (%)	40.1	42.7	54.2	50.8
unmodelled residues	288–322 (both monomers)	288–322 (both monomers)	291–322 (NrdF), 117–119 (NrdI)	291–322 (NrdF), 118–119 (NrdI)
volume not occupied by model (%)	28.8	30.7	45.2	43.0
	Model Analysis			
mean overall isotropic B-factor (Å ²)	19.8	19.5	32.9	32.1
Ramachandran plot: ratio in most favored/other allowed regions/generously allowed regions (%)	96.9/3.1/-	96.9/3.1/-	92.7/6.5/0.8	95.9/3.5/0.5
estimated overall coordinate error based on <i>R</i> _{work} /maximum likelihood (Å)	0.19/0.11	0.33/0.15	0.18/0.12	0.11/0.084
RMSD bonds (Å)/angles (deg)	0.019/1.90	0.017/1.78	0.019/2.04	0.020/1.90
PDB code	4BMU	4BMT	4BMP	4BMO

^aThe value before the slash is for all data, and the value after the slash is for the data in the highest resolution shell. ^b*R*_{sym} = $\sum |I| - \langle I \rangle / \sum I$ ^c*R*_{work} = $\sum (|F_o| - |F_c|) / \sum |F_o|$ ^d*R*_{free} is the *R*_{work} calculated on the 5% reflections excluded for refinement.

full metal occupancy at the dimetal sites. The higher B-factor of the Fe1 sites in Fe₂-NrdF could indicate lower occupancy. The di-Fe sites in the ferrous soaked NrdF structure have higher coordination compared to the NrdI-Fe₂-NrdF structures (Figures 2, 3, and 4A). For monomer A, contrary to NrdI-Fe₂-NrdF-1, Glu195 has moved to a μ -(η^1 - η^2) coordination opening up for a water coordinating to Fe1 instead of a water molecule hydrogen-bound to Tyr100, the residue responsible for tyrosyl radical (Y●) generation in *Bc*. This results in the Fe sites becoming five- and six-coordinated, respectively, differing from what has been observed by circular dichroism and magnetic circular dichroism on RNR protein solutions.^{2,38} The μ -(η^1 - η^2) coordination of Glu195 (*Bc* numbering) in *Bc* Fe₂-NrdF is also observed in *Ec* Fe₂-NrdB (without the water coordinating to Fe1) and in *Ec* Mn^{II}₂-NrdF structures, while the Fe^{II}₂-NrdF structures from *Ca*, *Salmonella typhimurium* (*St*),

Mt, and the Mn^{II}₂-NrdF structures from *Ca*, *Ec*, and *Bs* all show the μ -1,3 coordination (Figure 4B).^{13,25,30,32,33} In monomer B of *Bc* Fe₂-NrdF, Glu161 coordinates to Fe2 in a monodentate way instead of bidentate, resulting in both di-Fe sites being five coordinated (Figure 3A–D).

***Bc* Mn^{II}₂-NrdF Coordination Environment and Glu161 Movement.** The *Bc* Mn^{II}₂-NrdF structure has been modeled with full occupancy at the dimetal sites (except for Mn2 in monomer A with 90% occupancy) (Figure 3E–H) and shows higher coordination for the dimetal site than in the *Bc* Fe₂-NrdF with both Mn-sites being six-coordinated similar to what is observed in *Ec*. In the *Bc* Mn^{II}₂-NrdF structure, Glu161 shows great flexibility. Two and three alternative conformations have been modeled at the Glu161 site in monomers A and B, respectively. In monomer A, one coordinates to metal site 2 alone, in a bidentate fashion (33%) as seen in the *Bc* Fe₂-NrdF

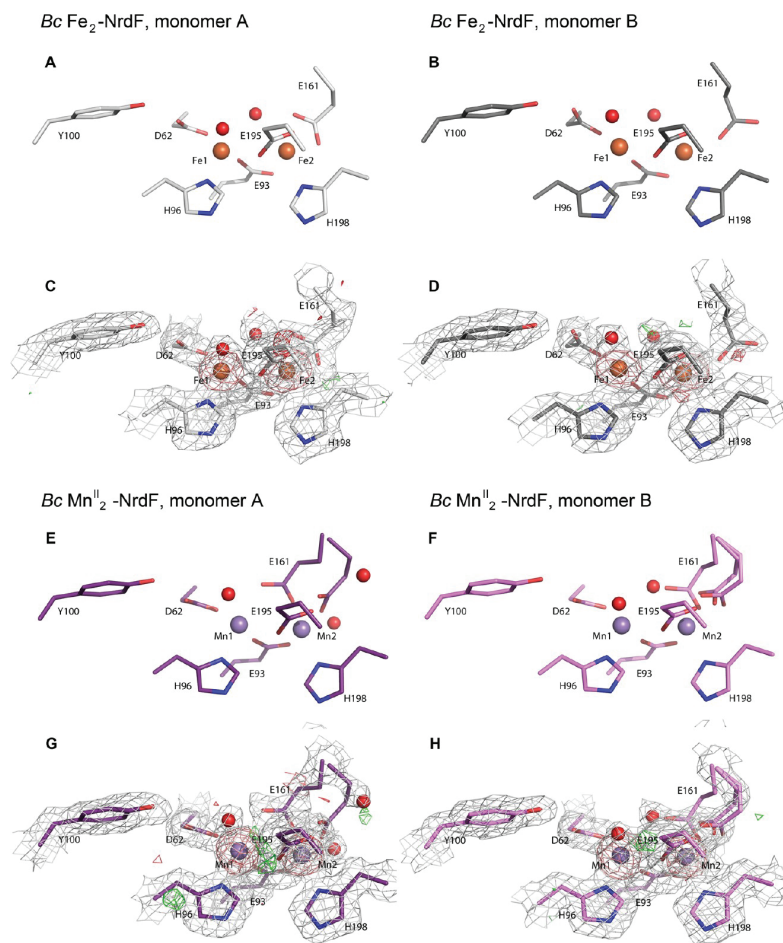


Figure 3. Metal ion sites in *Bc* Fe₂-NrdF and Mn^{II}₂-NrdF. (A and C) Monomer A in *Bc* Fe₂-NrdF, (B and D) monomer B in *Bc* Fe₂-NrdF. (E and G) Monomer A in *Bc* Mn^{II}₂-NrdF and (F and H) monomer B in *Bc* Mn^{II}₂-NrdF. The Fe ions are shown as orange spheres, Mn ions as purple spheres, and the coordinating amino acids and Tyr100 are represented as sticks and colored by atom type. The $2F_o - F_c$ electron density map (gray) is contoured at 1σ and the $F_o - F_c$ map is shown as green mesh (3σ) and red mesh (-3σ), whereas the omit map (salmon) surrounding the Fe or Mn ions is contoured at 6σ (C, D, G and H). Glu161 coordinates to Fe2 in a bidentate fashion in monomer A and in a monodentate fashion in monomer B of Fe₂-NrdF (A–D). In Mn₂-NrdF, two and three different conformations are observed for Glu161 in monomers A and B, respectively, varying between a bidentate mode coordinating to Mn2 alone and a conformation bridging both metals (E–H).

structures, while the other major conformations (67%) bridge both metals similar to the μ -1,3 coordination observed in the *Ec* NrdI-Mn^{II}₂-NrdF and Mn^{II}₂-NrdF structures (Figure 4B). This opens up for a water coordinating to the Mn2 site and an extended water network (as discussed below). The μ -1,3 coordination of this Glu residue was not reported for the *Bs* Mn^{II}₂-NrdF structure (PDB id: 4DR0)³³ and thereby not supporting a direct Fe to Mn induced movement of Glu158 (*Ec* numbering) as observed in *Ec* and now in *Bc*. However, although Glu164 (*Bs* numbering) is reported to coordinate only to Mn2 in a bidentate fashion, some negative density can be seen in the difference map at the modeled Glu164, and some positive density where an alternative conformation for Glu164

bridging both metals in a μ -1,3 fashion would be positioned, supporting flexibility at the Glu161 (*Bc* numbering) site. In the *Ec* structures, the main-chain between Phe162 and Glu158 (*Ec* numbering) has an altered conformation between the Fe and Mn structures, while in the *Bc* structures, the main-chain between Phe165 and Glu161 (*Bc* numbering) is more similar, resulting in an incomplete μ -1,3 coordination of Glu161 in *Bc* Mn^{II}₂-NrdF (Supplementary Figure S3). The observed difference could be due to the fact that the *Ec* structures are co-crystallized with Mn^{II}, while the *Bc* crystals have been soaked with Mn^{II}, thereby allowing less structural adjustments in *Bc*. This further indicates that the Glu161 movement is linked to the Mn substitution. The movement of Glu161 in *Bc* from a

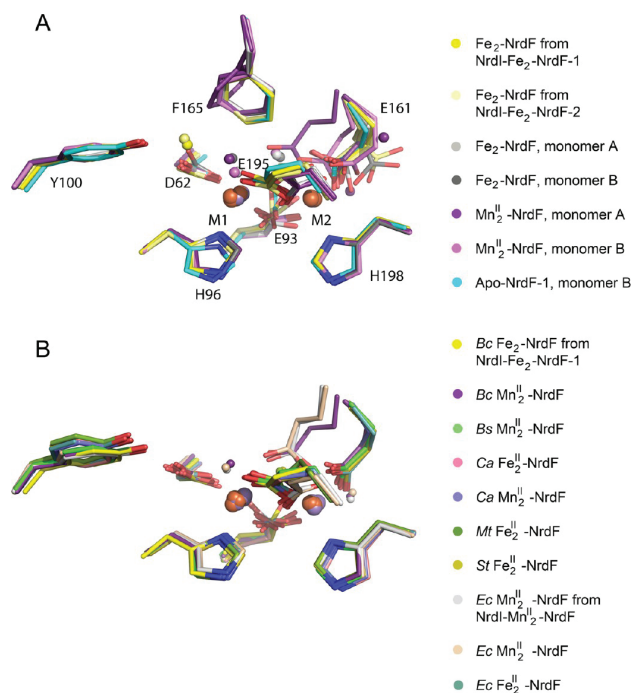


Figure 4. Overlay of metal sites in different NrdF crystal structures. (A) Metal sites in the different *Bc* NrdF crystal structures. (B) Metal sites in class Ib β_2 structures from different organisms. The Mn ions and Fe ions are colored as purple and orange spheres, respectively, and the coordinating amino acids, as well as Tyr100 and Phe165, are represented as sticks and colored by atom type. Structures compared in panel B (A chains) are; *Bc* NrdI- Fe_2 -NrdF-1, *Ec* NrdI- Mn_2^{II} -NrdF complex (PDB id: 3N39),²⁵ *Bc* Mn_2^{II} -NrdF, *Ec* Mn_2^{II} -NrdF (PDB id: 3N37),²⁵ *Ec* Fe_2^{II} -NrdF (PDB id: 3N38),²⁵ *Bs* Mn_2^{II} -NrdF (PDB id: 4DR0),³⁵ *Ca* Mn_2^{II} -NrdF (PDB id: 1KGP),³⁰ *Ca* Fe_2^{II} -NrdF (PDB id: 1KGO),³⁰ *Mt* Fe_2^{II} -NrdF (PDB id: 1UZR),³² and *St* Fe_2^{II} -NrdF (PDB id: 1R2F).¹³

bidentate coordination of metal site 2 to a μ -1,3 coordination is further associated with a rotation of Phe165 (Figure 4A and Supplementary Figure S3), which is also observed in *Ec* between the Fe_2^{II} -NrdF and Mn_2^{II} -NrdF/NrdI- Mn_2^{II} -NrdF structures.²⁵ Moreover, if the flexibility of Glu161 in the *Bc* Mn_2^{II} -NrdF structures is influenced by a minor iron contamination, as previously reported in work by Tomter et al.,³⁸ an inhomogeneous metalation in metal site 2 would even stronger support a metal-type-dependent movement of Glu161. The redox state and the pH of the metal ion cluster is also known to influence the conformation of the coordinating residues.^{6,39} The metal cluster environments in the two *Bc* apo-NrdF structures are shown in Supplementary Figures S4 and S5. The trends for Glu195 and Glu93 coordination seem more unclear, while Glu161 coordination appears to give important insight into the distinction between the Fe- and Mn-NrdF/NrdI-NrdF structures (Figure 4A and B). In both *Bc* NrdI- Fe_2 -NrdF complex crystals, Glu161 coordinates bidentate to iron site 2 alone, opposite to what is seen in the *Ec* NrdI- Mn_2^{II} -NrdF structure, where the corresponding carboxylate ligand bridges both metals in a μ -1,3 fashion (Figure 4B). It has been proposed that the latter conformation allows greater access of a manganese-bound water ligand, hydrogen-bonded to an ordered water network facilitating oxidant transport from the NrdI FMN cofactor.²⁵ The μ -1,3 coordination of Glu161 is

observed in both the *Ec* Mn_2^{II} -NrdF structure and the *Bc* Mn_2^{II} -NrdF structure (major conformation in monomer A), the latter presented here. The *Bc* Mn_2^{II} -NrdF and *Bc* Fe_2 -NrdF structures presented here are therefore important toward a more generalized understanding of the metal-ion-dependent movement of this Glu residue with respect to NrdF activation. These observations support greater flexibility of the residues surrounding the class Ib NrdF metal sites and that variations in the carboxylate conformations seem to be linked to the metal-type present at the dimetal site, rather than induced by NrdI binding to NrdF, as also supported by NrdI-NrdF binding studies in *Ba* apo, Fe-, and Mn-NrdF.²⁷

NrdI-NrdF Interface Solvent Channel. In the *Ec* and *Bc* NrdI-NrdF complexes, the proposed solvent-accessible channel extends from the vicinity of the metal site 2 in NrdF to the FMN cofactor of NrdI (Figure 5). This channel is structurally conserved in *Bc* and *Ec* NrdF with identical side-chain geometries of the lining residues Ser157/154, Tyr166/163, Ser162/159, Asn267/264, Lys263/260 and main-chain C=O for Glu195/192, Ser196/Ala193 (*Bc*/*Ec* numbering). In the interface between NrdF and NrdI, the water network is slightly altered, due to Tyr 197 in *Ec* replacing Val200 in *Bc*; however, FMN is also slightly shifted. Unlike observed in the *Ec* Mn_2^{II} -NrdF structures with Glu158 in a μ -1,3 coordination, the solvent channel modeled in the *Bc* NrdI-NrdF complex is

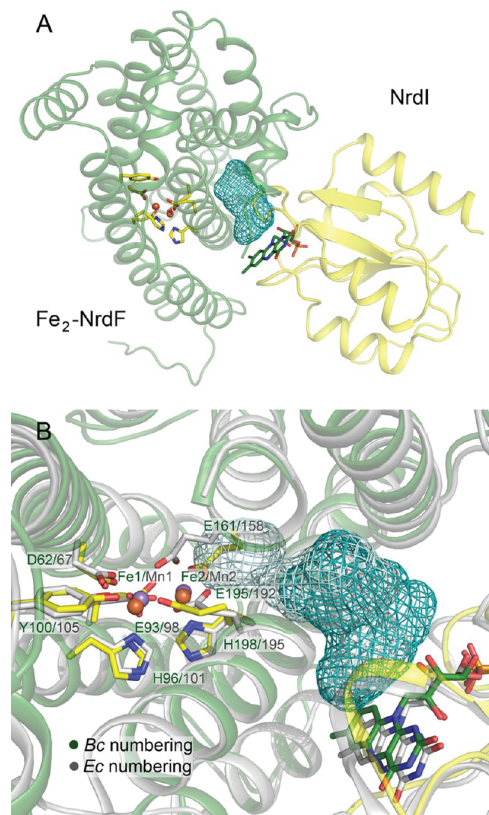


Figure 5. NrdI-NrdF solvent channel. (A) The *Bc* NrdI-Fe₂-NrdF complex structures showing the hydrophilic channel connecting the active site in Fe₂-NrdF with the FMN cofactor in NrdI, calculated using a 1.4 Å probe radius, and (B) structural alignment of the *Bc* and *Ec* (PDB id: 3N39) NrdI-Fe₂-NrdF and NrdI-Mn^{II}₂-NrdF complexes, respectively, showing a closer view of the solvent channel (*Bc*; blue mesh, *Ec*; cyan mesh) connecting the NrdF and NrdI cofactors. *Bc* NrdI is shown as a yellow ribbon diagram and *Bc* Fe₂-NrdF as a green ribbon diagram, whereas the FMN cofactor in *Bc* NrdI and the residues in the active site of *Bc* Fe₂-NrdF are represented as sticks and colored by atom type. The *Ec* structure is shown in gray. Fe ions are shown as orange spheres (*Bc*), while Mn^{II} ions are shown as purple spheres (*Ec*). The Glu161 conformation in the *Bc* structure occupies the terminal part of the solvent channel, as modeled for the *Ec* structure, preventing the solvent channel in *Bc* from accessing the Fe₂-NrdF site.

prevented from accessing the Fe₂-NrdF site largely due to the bidentate coordination mode of Glu161 to Fe₂, blocking the channel (Figure 5). Only in the case of the *Ec* NrdI-Mn^{II}₂-NrdF structure does Glu158 allow full access of the solvent channel directly to the vicinity of the Mn^{II}₂ site. A similar water network is also seen around the Mn₂ site in the *Bc* Mn^{II}₂-NrdF structure (Figure 3E and G). The NrdI-NrdF channel modeled for the *Bc* complex, and compared to the *Ec* complex, is shown in Figure 5A and B, respectively. Different Glu161 conformations observed for the *Ec* NrdI-Mn^{II}₂-NrdF and *Bc* NrdI-Fe₂-NrdF complex structures indicate that variations in the NrdF active

site geometries might be present during active cofactor formation. The different geometries are likely not affected by NrdI binding to NrdF in protein complex formation. Highly similar NrdI-NrdF interfaces in both complexes are observed (see below), regardless of metal ion bound in the NrdF active site.

NrdF Interface with NrdI. The overall structure comparison of *Ec* and *Bc* NrdI-NrdF shows that the overall interaction between NrdF and NrdI is similar in the two organisms; however, the binding of NrdI to NrdF in *Bc* is slightly rotated compared to NrdI-NrdF binding in *Ec* (Supplementary Figure S1). The amino acids lining the *Bc* and *Ec* NrdI-NrdF interface show a high level of conservation. This is a general attribute for all class Ib RNRs, supported by the high sequence similarity³³ at the interface region, supporting invariable NrdI binding to the NrdF surface for class Ib RNRs. The charged and polar residues lining the NrdI-NrdF interface in both *Ec* and *Bc* complex structures create a hydrophilic environment consistent with channeling of a hydrophilic oxidant: H₂O₂ or O₂•⁻ for generation of the active Mn^{III}₂-Y• cofactor in class Ib RNRs. One variation between the two complex structures of NrdI-NrdF in *Bc* and *Ec* is the distance between the NrdI flavin plane to the NrdF interface, which is 0.4 Å closer (based on whole structure alignment as measured from N5 of FMN), for the *Bc* structure, creating a narrower interface (Figure 1B). A comparison of the *Bc* and *Ec* NrdI-NrdF structures, showing an ordered and identical hydrogen bonding network between conserved residues lining the core interface in both structures, is shown in Figure 6A and B. This core interface is likely essential for recognition between NrdFs and NrdIs in class Ib RNRs. Frequently, proteins involved solely in electron transfer do not interact in a well-defined orientation,⁴⁰ and therefore, the observation of a conserved binding-core between NrdI and NrdF supports that the complex is important for more than pure electron transfer, as it also generates a channel for the transfer of H₂O₂ or O₂•⁻. Outside this core region, however, residues in the protein interface are not conserved, probably leading to a small rotation of NrdI relative to NrdF as observed between the *Bc* and *Ec* NrdI-NrdF structures (Supplementary Figure S1). While the core region governs recognition, amino acid differences outside the core must be important for the variations observed in NrdI-NrdF binding in *Ec* and the *Bacillus* species, where the association is much stronger in *Ec* than in *Bacillus*.^{18,22,27,28} The conserved core interface region on the NrdF surface, as observed in the *Bc* and *Ec* NrdI-NrdF complex structures, is not present in the class Ia R2/NrdB, as shown in the structural alignment of the *Bc* NrdF and *Ec* NrdB structures⁴¹ (Supplementary Figure S6). The structural differences in NrdBs, compared to NrdFs, do not support binding to NrdI, as observed in the class Ib NrdI-NrdF complex structures.²⁵ Moreover, the conserved class Ib NrdF interface region is also absent in eukaryotic class Ia R2 structures, as observed in mouse R2³⁹ and human p53R2.⁴²

Spectroscopic Similarity between NrdI and NrdI-NrdF.

Single-crystal light absorption measurements performed on crystals of *Bc* NrdI and *Bc* NrdI-NrdF show similar flavin spectra, indicating little or no influence on the NrdI FMN cofactor upon NrdF binding. Figure 6C shows the spectra obtained from the two crystals (*Bc* NrdI and *Bc* NrdI-NrdF) both containing NrdI in its oxidized (NrdI_{ox}) form. The light absorption spectrum of a crystal depends on crystal orientation relative to the incident beam, causing small variations in the shapes of different peaks.⁴³ High structural similarity is

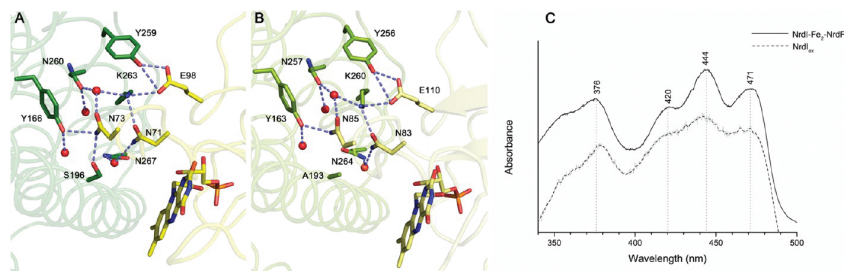


Figure 6. NrdI-NrdF protein-protein interface and single-crystal light absorption spectra. Comparison of the conserved hydrogen bonding network in the NrdI-NrdF core interface in the (A) *Bc* and (B) *Ec* (PDB id: 3N39) NrdI-NrdF crystal structures. NrdF residues are colored green, while NrdI residues are colored yellow. (C) Single-crystal light absorption spectra of *Bc* NrdI (dashed) and NrdI-NrdF (solid). Typical features of the oxidized state of the flavin cofactor are observed for the NrdI_{ox} crystal and similar features are in the NrdI-NrdF crystal, regardless of the interaction with NrdF. A weaker signal is observed for the NrdI spectrum, largely due to crystal thickness.

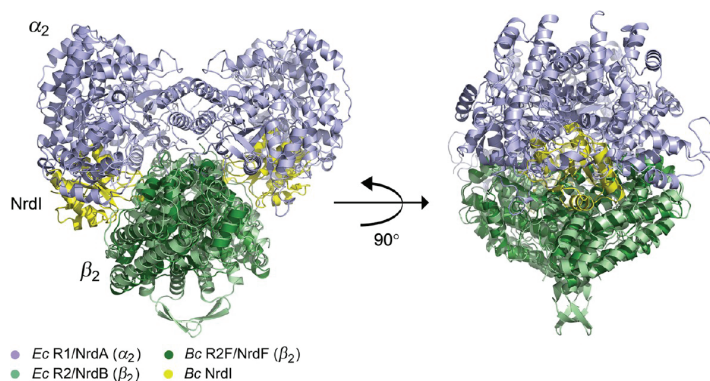


Figure 7. *Ec* class Ia $\alpha_2\beta_2$ holoenzyme complex. The holoenzyme complex, shown from two different views (A and B), was generated by alignment of the R2 dimer (β_2) with the R1 dimer (α_2),¹⁴ overlaid with the class Ib *Bc* NrdI-Fe₂-NrdF complex. NrdI protrudes into the $\alpha_2\beta_2$ interface, interfering with binding to the R1 dimer.

observed between NrdI from the *Bc* NrdI-NrdF crystal complex and *Bc* NrdI (PDB id: 2X2O)²³ (RMSD calculated to 0.37 Å) and between Fe₂-NrdF and NrdF from the *Bc* NrdI-NrdF crystal complex (RMSD calculated to 0.54 Å).

Investigation of the Possible NrdI-NrdF-NrdE Interface. Given that NrdI is required for Mn^{III}-Y• cofactor generation,²⁴ it is important to gain information about how NrdI-NrdF assembly effects NrdF-NrdE holoenzyme formation. A model of the $\alpha_2\beta_2$ holoenzyme structure was first proposed by Uhlin and Eklund in 1994¹⁴ for the class Ia RNR. Complementarity was shown between the α_2 (NrdA) dimer and the upper part of the heart-shaped structure of the β_2 (NrdB) dimer, and a model was constructed with the 2-fold axes of the dimers superimposed. The proposed holoenzyme is believed to form a compact complex, where the binding surface of the NrdB dimer contains a region of high conservation.¹⁴ A high extent of amino acid conservation in the corresponding region has also been addressed for various class Ib NrdF structures, through a sequence alignment study performed by Boal et al.³³ Also, high amino acid sequence conservation was shown for the NrdI-NrdF interface. The *Bc* NrdI-NrdF complex interface supports NrdI binding in the same general location on all NrdFs, as suggested previously.³³ In this study, we report that binding of NrdI to NrdF can disturb the $\alpha_2\beta_2$

holocomplex formation in class Ib RNRs, contrary to what was previously suggested by Zhang et al.²⁹ The NrdI-NrdF complex assembly in *Bc* introduces steric clashes in the binding site between α_2 and β_2 in the proposed holocomplex assembly, possibly preventing the suggested holoenzyme complex formation. A structural alignment of the *Bc* NrdI-NrdF structure with the *Ec* $\alpha_2\beta_2$ holoenzyme structure, generated using the original class Ia $\alpha_2\beta_2$ holocomplex coordinates, is shown in Figure 7. The two aligned dimeric class Ia and Ib R2 structures share a structural homology with an RMSD of 2.6 Å. These findings could possibly indicate the role of a different holocomplex interaction for the class Ib RNRs, which, contrary to the class Ia RNRs, require an additional binding partner, NrdI, for Mn^{III}-Y• cofactor assembly. However, recent studies of *Ec* RNR support the active prokaryotic form of the enzyme with an $\alpha_2\beta_2$ stoichiometry.^{15,44} Conversely, another likely possibility supporting the $\alpha_2\beta_2$ holoenzyme structure by Uhlin and Eklund is that the activation of the Mn^{III}-Y• cofactor occurs in an initial stage prior to R1-R2 interaction in the $\alpha_2\beta_2$ complex. This would result in NrdI dissociation prior to $\alpha_2\beta_2$ holoenzyme formation, thereby preventing structural clashes between the respective binding partners. The structural requirement of NrdI dissociation prior to NrdE binding to NrdF could be supported by, as well as further explain, previous

activity and binding studies in *Ec*, *Bc*, and *Ba*. In *Ec*, a tight association between NrdI and NrdF has been reported,¹⁸ and if NrdI needs to dissociate before NrdE can bind, this could explain the observed lower RNR specific activity of Fe-NrdF-NrdE in the presence of NrdI, resulting in an inhibitory effect, compared to a 4-fold higher specific activity in the absence of NrdI.¹⁸ In contrast, in the case of *Bacillus* species, where the interaction between NrdF and NrdI has been shown to be weak,^{22,27} NrdI does not inhibit Fe^{III}-Y• cofactor generation (in *Ba* and *Bc*)²⁸ or RNR enzymatic activity (in *Ba*²⁷ and *Bc*²⁸), indicating that the weaker NrdI-NrdF association in *Ba* and *Bc* makes NrdF more accessible for NrdE binding. Additionally, the removal of NrdI after activation of Mn-NrdF by NrdI does not increase specific activity in *Ba* and *Bc* or influence the binding of NrdH-thioredoxin to NrdE.²⁷ However, this type of investigation has not been reported for the *Ec* Mn-containing RNR, which might result in higher *in vitro* specific activity proceeding from NrdI removal, as a result of NrdI's tight association with NrdF. The $\alpha_2\beta_2$ holoenzyme model by Uhlin and Eklund could then be valid also for class Ib. Whether the differences between *Ec* and *Bacillus* species could be related to the presence of the additional class Ia RNR in *Ec* should be further investigated. The conserved NrdI binding to NrdF could be of great importance in the development of antimicrobial drugs, depending on the organisms degree of NrdI-NrdF affinity. Moreover, an alteration in the NrdF interface responsible for binding of NrdI as well as NrdE could strongly affect active class Ib RNR activation and holoenzyme assembly. An overlay of *Bc* NrdI-NrdF with the *St* R1-R2 crystallographic complex from Uppsten et al.⁴⁵ also results in some clashes (Supplementary Figure S7A). In contrast, an overlay of the *Bc* NrdI-NrdF structure and the inactive $\alpha_2\beta_4$ *Ec* structure⁴⁶ gives no structural clashes between NrdI and NrdB (Supplementary Figure S7B). Moreover, additional studies for investigation of class Ib RNR interactions and active holoenzyme formation are still required.

Conclusion. The *Bc* NrdI-NrdF complex structure presented in this paper strongly resembles the previously solved NrdI-NrdF complex from *Ec*,²⁵ showing only small variations in NrdI binding to NrdF in class Ib RNRs. The flexibility in key coordinating residues of the dimetal sites in *Bc* NrdI-NrdF and NrdF structures supports the suggestion that different active site geometries can serve as starting points for metallocofactor activation. However, Glu161 (*Bc* numbering) seems to be a key residue in distinguishing between the Fe and Mn activated structures. The higher tendency of Glu161 for a μ -1,3 coordination in Mn structures, as now seen in both *Ec* and *Bc*, in contrast to the bidentate coordination seen in Fe structures, opens up for a water network through the proposed and highly conserved hydrophilic channel leading to the FMN site in NrdI. The channel and water network is blocked in the *Bc* NrdI-Fe₂-NrdF and Fe₂-NrdF structures through the bidentate coordination of Glu161 to metal site 2. The high degree of amino acid sequence conservation of core residues in the NrdI-NrdF interface supports similar NrdI-NrdF recognition in all class Ib RNRs, as indicated by the same general binding location in the crystal structures of NrdI-NrdF complexes in *Bc*, *Ec*,²⁵ and the modeled *Bs* NrdI-NrdF complex.³³ Since binding of NrdI to NrdF also occurs for Fe₂-NrdF, not requiring NrdI for activation, the presence of Mn is not a requirement for NrdI binding. This is supported by the *Bc* NrdI-NrdF complex structure, crystallized with an Fe₂ site contrary to the *Ec* NrdI-Mn^{II}-NrdF crystal structure, which is

the Mn^{II}-containing active complex. Also, NrdI-NrdF binding seems to be conserved regardless of the structure of the metal coordination site, where different carboxylate conformations are observed for different crystal structures. Steric clashes introduced by NrdI in the NrdI-NrdF-NrdE formation presented in this study could indicate a requirement for NrdI to dissociate before NrdE can bind to NrdF; however, further investigation of the mechanism of class Ib active holoenzyme formation is required.

METHODS

Cloning, Expression, and Purification of *Bc* NrdF and NrdI. *Bc* ATCC 14579 NrdF (BC1355) and NrdI (BC1353) were expressed and purified as described previously.^{23,38} In brief, genes were cloned into the pET-22b plasmid (Novagen) prior to transformation into competent *Ec* BL21 (DE3) Gold cells (Stratagene). Cells containing the pET-22b-NrdF or -NrdI were grown in Terrific Broth medium containing 100 μ g/mL ampicillin. Protein expression was induced by adding isopropyl β -D-1-thiogalactopyranoside to a final concentration of 0.8 mM, and the culture was incubated for 12–16 h at 20 °C with vigorous shaking before harvesting. The frozen cell paste was lysed using an X-press,⁴⁷ dissolved in 100 mM Tris-HCl, pH 7.5, 10 mM EDTA, and cleared from nucleic acids by streptomycin sulfate (2.5%) precipitation. Proteins were precipitated with 60% ammonium sulfate (0.43 mg/mL), dissolved in 50 mM Tris-HCl, pH 7.5, and desalted using a HiTrap Desalting column (GE Healthcare). Desalted protein was applied to a HiTrap HP Q column (GE Healthcare), and the proteins were separated with a 0–0.5 M KCl gradient. As a final polishing step, the proteins were purified on a Superdex 200 column (GE Healthcare).

Crystallization. All initial crystallization screening was performed with an Orx6 crystallization robot (Douglas Instruments Ltd.).

Crystallization of the *Bc* NrdI-NrdF Complex. For the NrdI-NrdF complex, NrdF (monomer) and NrdI (both in 50 mM Tris-HCl, pH 7.5) were mixed in an equimolar amount. Bright yellow crystals (20 mg/mL total protein) were obtained using the sitting drop vapor diffusion method at RT with 10% (w/v) PEG 8000, 0.2 M magnesium chloride, and 0.1 M Tris, pH 7.0 (JCSG-plus Screen, Molecular Dimensions Ltd.). Crystals were briefly soaked in cryoprotectant solution (25% glycerol, 10% (w/v) PEG 8000, 0.2 M magnesium chloride, and 0.1 M Tris, pH 7.0) and flash frozen in liquid nitrogen (NrdI-NrdF-1). Yellow crystals (5 mg/mL total protein) were also obtained using the same method with 2 M sodium chloride and 0.1 M sodium citrate, pH 6.0 (ProPlex Screen, Molecular Dimensions Ltd.), soaked in cryoprotectant solution (25% PEG 400, 2 M sodium chloride, and 0.1 M sodium citrate, pH 6.0) and flash frozen in liquid nitrogen (NrdI-NrdF-2). The NrdI-NrdF crystals were not soaked in metal solutions before collecting X-ray data; however, the medium used for expression of the genes naturally contains traces of iron.

Crystallization of *Bc* NrdFs. Fe₂-NrdF and Mn^{II}-NrdF crystals (8 mg/mL monomer) were obtained with 0.2 M Mg-formate, 20% (w/v) PEG 3350, and 0.1 M HEPES, pH 7.5 (optimized from the JCSG-plus Screen, Molecular Dimensions Ltd.) and soaked for 20 min in cryoprotectant solution containing the mother liquor mixed with 25% PEG 400 and Fe(NH₄)₂(SO₄)₂/sulfuric acid or MnCl₂, respectively. Also, two apo-NrdF structures have been solved from crystals obtained with 0.04 M H₃PO₄, 16% PEG 8000, and 20% glycerol (apo-NrdF-1), and with 0.2 M Mg-formate pH 5.9 and 20% PEG 3350 (apo-NrdF-2) (JCSG-plus Screen, Molecular Dimensions Ltd.), both soaked in cryoprotectant solution containing the mother liquor including 30% glycerol. Finally, all NrdF crystals were flash frozen in liquid nitrogen.

Data Collection and Refinement. Crystallographic data sets were collected at beamlines ID29 and ID14-1 at the European Synchrotron Radiation Facility (ESRF), Grenoble, France and at PXII-X10SA at the Swiss Light Source (SLS) at Paul Scherrer Institut, Villigen, Switzerland. The crystallographic data for NrdI-NrdF-1, as well as Fe₂-NrdF and Mn^{II}-NrdF, were collected at ID29 (ESRF), the apo-NrdF-1 and apo-NrdF-2 at ID14-1 (ESRF), and the NrdI-NrdF-2

at X10SA (SLS). Data sets were processed with MOSFLM⁴⁸ and scaled and merged using SCALA or AIMLESS,^{49,50} and the space group was confirmed with POINTLESS through the CCP4 software suite.⁵¹ The structures were solved by molecular replacement using PHASER.⁵² A homologue model of *Bc* apo-NrdF modeled with SWISS-MODEL^{53,54} from the *Ca* apo-R2 structure (PDB id: 3DHZ)⁴² was used as a search model in PHASER to solve the *Bc* apo-NrdF-1 structure. The *Bc* apo-NrdF-1 was then used as a search model to solve the structure of apo-NrdF-2, Fe₂-NrdF, and Mn^{II}-NrdF. The NrdI-NrdF-1 structure was solved with the coordinates of *Bc* apo-NrdF-1 and *Bc* NrdI (PDB id: 2X2O) as the starting models. Refinement for all structures was done using restrained refinement in REFMAC,⁵⁵ and model building was performed with COOT⁵⁶ in multiple cycles. For the *Bc* NrdF structures, medium NCS restraints were introduced. For some of the structures, full occupancy of the metal sites gave negative density in the difference maps, and for these structures the metal content was reduced. NrdI-NrdF-1 has been refined with 90% Fe, NrdI-NrdF-2 with 50% Fe, Mn^{II}-NrdF with one site 90% while the remaining 100% Mn, and Fe₂-NrdF with 100% Fe with high B-factors. For the apo structures, one of the metal sites 1 in apo-NrdF-1 and two metal sites 1 in apo-NrdF-2 have been modeled with 25% occupancy of Fe. The absorbed X-ray doses of the different crystals during crystallographic data collection have been calculated with the program RADDOSE.^{57,58} All structure figures were prepared using PyMOL.⁵⁹ All backbone root-mean-square deviation (RMSD) values were calculated using PDBeFold (<http://www.ebi.ac.uk>). The final data collection and refinement statistics are listed in Table 1 and Supplementary Table S1. The hydrophilic complex channel lining the *Bc* NrdI-NrdF interface was calculated with HOLLOW⁶⁰ using a 1.4 Å probe radius. As a comparison, a corresponding channel was also calculated for the *Ec* NrdI-NrdF structure.²⁵

Single-Crystal Light Absorption Spectroscopy. Light absorption spectroscopy was carried out on single crystals (frozen as described above) of *Bc* NrdI and *Bc* NrdI-NrdF. The experiments were performed at beamline X10SA and SLSpectroLAB at SLS. Spectra were recorded with an on-axis built microspectrophotometer system with an Andor 303i Czerny–Turner spectrograph and a Newton electron multiplying CCD (Andor Technology).⁶¹

■ ASSOCIATED CONTENT

Supporting Information

Supplementary table and figures. This material is available free of charge via the Internet at <http://pubs.acs.org>.

Accession Codes

The coordinates and structure factors (codes 4BMO, 4BMP, 4BMQ, 4BMR, 4BMT, and 4BMU) have been deposited in the Protein Data Bank through EMBL-EBI (<http://www.pdbe.org>) and are listed in Table 1 and Supplementary Table S1.

■ AUTHOR INFORMATION

Corresponding Author

*E-mail: h.p.hersleth@ibv.uio.no.

Notes

The authors declare no competing financial interest.

■ ACKNOWLEDGMENTS

We thank B. Dalhus for access to crystallization screening at the Regional Core Facility for Structural Biology and Bioinformatics at the South-Eastern Norway Regional Health Authority (Grants no. 2009100 and 2011040). We gratefully acknowledge the Swiss-Light-Source SLS (20111245) for providing beam time with online microspectrophotometry and help from the team at X10SA and G. Pompidor for assistance with the on-axis online microspectrophotometer. We gratefully acknowledge the European Synchrotron Radiation Facility ESRF (MX10156) for providing beam time, and the team at ID29 and ID14-1 for

their assistance. The coordinates for the *E. coli* class Ia $\alpha\beta_2$ holoenzyme structure were kindly provided by U. Uhlin, Uppsala University, Uppsala, Sweden. We acknowledge financial support from the Norwegian Research Council through projects 214239/F20 and 218412/F50 (K.K.A.), MLS^{UIO} program for Molecular Life Science research at the University of Oslo through the PX-Oslo X-ray core facilities and the Norwegian Cancer Society 539012 (K.K.A.) and CMST COST Action CM1003 and financial support for synchrotron travel from the Norwegian Research Council through projects 138370/V30 and 216625/F50 (K.K.A.) and from the European Community's Seventh Framework Programme (FP7/2007-2013) under BioStruct-X (grant agreement No. 283570) on project 1760 (K.K.A./H.P.H.).

■ ABBREVIATIONS

RNR, ribonucleotide reductase; *Bc*, *Bacillus cereus*; *Ec*, *Escherichia coli*; *Mt*, *Mycobacterium tuberculosis*; *Ca*, *Corynebacterium ammoniagenes*; *Ba*, *Bacillus anthracis*; *St*, *Salmonella typhimurium*; FMN, flavin mononucleotide cofactor; ESRF, European Synchrotron Research Facility; SLS, Swiss-Light-Source; RMSD, root-mean-square deviation

■ REFERENCES

- (1) Nordlund, N., and Reichard, P. (2006) Ribonucleotide reductases. *Annu. Rev. Biochem.* 75, 681–706.
- (2) Tomter, A. B., Zoppellaro, G., Andersen, N. H., Hersleth, H. P., Hammerstad, M., Rohr, A. K., Sandvik, G. K., Strand, K. R., Nilsson, G. E., Bell, C. B., Barra, A. L., Blasco, E., Le Pape, L., Solomon, E. I., and Andersson, K. K. (2013) Ribonucleotide reductase class I with different radical generating clusters. *Coord. Chem. Rev.* 257, 3–26.
- (3) Andersson, K. K., Ed. (2008) *Ribonucleotide Reductase*, Nova Science Publishers, Inc., Hauppauge, NY.
- (4) Cotruvo, J. A., and Stubbe, J. (2011) Class I ribonucleotide reductases: Metallocofactor assembly and repair in vitro and in vivo. *Annu. Rev. Biochem.* 80, 733–767.
- (5) Tomter, A. B., Zoppellaro, G., Schmitzberger, F., Andersen, N. H., Barra, A. L., Engman, H., Nordlund, P., and Andersson, K. K. (2011) HF-EPR, Raman, UV/VIS light spectroscopy, and DFT studies of the ribonucleotide reductase R2 tyrosyl radical from Epstein-Barr virus. *PLoS One* 6, e25022.
- (6) Kolberg, M., Strand, K. R., Graff, P., and Andersson, K. K. (2004) Structure, function, and mechanism of ribonucleotide reductases. *Biochim. Biophys. Acta, Proteins Proteomics* 1699, 1–34.
- (7) Atkin, C. L., Thelander, L., Reichard, P., and Lang, G. (1973) Iron and free-radical in ribonucleotide reductase - exchange of iron and mossbauer-spectroscopy of protein-b2 subunit of *Escherichia-coli* enzyme. *J. Biol. Chem.* 248, 7464–7472.
- (8) Jiang, W., Yun, D., Saleh, L., Barr, E. W., Xing, G., Hoffart, L. M., Maslak, M. A., Krebs, C., and Bollinger, J. M. (2007) A manganese-(IV)/iron(III) cofactor in *Chlamydia trachomatis* ribonucleotide reductase. *Science* 316, 1188–1191.
- (9) Høgbom, M., Stenmark, P., Voevodskaya, N., McClarty, G., Graslund, A., and Nordlund, P. (2004) The radical site in chlamydial ribonucleotide reductase defines a new R2 subclass. *Science* 305, 245–248.
- (10) Roshick, C., Iliffe-Lee, E. R., and McClarty, G. (2000) Cloning and characterization of ribonucleotide reductase from *Chlamydia trachomatis*. *J. Biol. Chem.* 275, 38111–38119.
- (11) Voevodskaya, N., Lenzian, F., Ehrenberg, A., and Graslund, A. (2007) High catalytic activity achieved with a mixed manganese-iron site in protein R2 of *Chlamydia* ribonucleotide reductase. *FEBS Lett.* 581, 3351–3355.
- (12) Lundin, D., Torrents, E., Poole, A. M., and Sjöberg, B. M. (2009) RNRdb, a curated database of the universal enzyme family

ribonucleotide reductase, reveals a high level of misannotation in sequences deposited to Genbank. *BMC Genomics* 10, 589.

(13) Eriksson, M., Jordan, A., and Eklund, H. (1998) Structure of *Salmonella typhimurium* nrdF ribonucleotide reductase in its oxidized and reduced forms. *Biochemistry* 37, 13359–13369.

(14) Uhlin, U., and Eklund, H. (1994) Structure of ribonucleotide reductase protein R1. *Nature* 370, 533–539.

(15) Logan, D. T. (2011) Closing the circle on ribonucleotide reductases. *Nat. Struct. Mol. Biol.* 18, 251–253.

(16) Jordan, A., Pontis, E., Atta, M., Krook, M., Gibert, I., Barbe, J., and Reichard, P. (1994) A 2nd class-I ribonucleotide reductase in enterobacteriaceae - characterization of the *Salmonella typhimurium* enzyme. *Proc. Natl. Acad. Sci. U.S.A.* 91, 12892–12896.

(17) Huque, Y., Fieschi, F., Torrents, E., Gibert, I., Eliasson, R., Reichard, P., Sahlin, M., and Sjöberg, B. M. (2000) The active form of the R2F protein of class Ib ribonucleotide reductase from *Corynebacterium ammoniagenes* is a diferric protein. *J. Biol. Chem.* 275, 25365–25371.

(18) Cotruvo, J. A., and Stubbe, J. (2010) An active dimanganese(III)-tyrosyl radical cofactor in *Escherichia coli* class Ib ribonucleotide reductase. *Biochemistry* 49, 1297–1309.

(19) Cox, N., Ogata, H., Stolle, P., Reijser, E., Auling, G., and Lubitz, W. (2010) A tyrosyl-dimanganese coupled spin system is the native metalloradical cofactor of the R2F subunit of the ribonucleotide reductase of *Corynebacterium ammoniagenes*. *J. Am. Chem. Soc.* 132, 11197–11213.

(20) Tomter, A. B., Zoppellaro, G., Bell, C. B., Barra, A. L., Andersen, N. H., Solomon, E. I., and Andersson, K. K. (2012) Spectroscopic studies of the iron and manganese reconstituted tyrosyl radical in *Bacillus cereus* ribonucleotide reductase R2 protein. *PLoS One* 7, e33436.

(21) Cotruvo, J. A., and Stubbe, J. (2008) NrdI, a flavodoxin involved in maintenance of the diferric-tyrosyl radical cofactor in *Escherichia coli* class Ib ribonucleotide reductase. *Proc. Natl. Acad. Sci. U.S.A.* 105, 14383–14388.

(22) Johansson, R., Torrents, E., Lundin, D., Sprenger, J., Sahlin, M., Sjöberg, B. M., and Logan, D. T. (2010) High-resolution crystal structures of the flavoprotein NrdI in oxidized and reduced states - an unusual flavodoxin. *FEBS J.* 277, 4265–4277.

(23) Rohr, A. K., Hersleth, H. P., and Andersson, K. K. (2010) Tracking flavin conformations in protein crystal structures with Raman spectroscopy and QM/MM calculations. *Angew. Chem., Int. Ed.* 49, 2324–2327.

(24) Cotruvo, J. A., and Stubbe, J. (2011) *Escherichia coli* class Ib ribonucleotide reductase contains a dimanganese(III)-tyrosyl radical cofactor in vivo. *Biochemistry* 50, 1672–1681.

(25) Boal, A. K., Cotruvo, J. A., Stubbe, J., and Rosenzweig, A. C. (2010) Structural basis for activation of class Ib ribonucleotide reductase. *Science* 329, 1526–1530.

(26) Cotruvo, J. A., Stich, T. A., Britt, D. R., and Stubbe, J. (2013) Mechanism of assembly of the dimanganese-tyrosyl radical cofactor of class Ib ribonucleotide reductase: Enzymatic generation of superoxide is required for tyrosine oxidation via a Mn(III)/Mn(IV) intermediate. *J. Am. Chem. Soc.* 135, 4027–4039.

(27) Crona, M., Torrents, E., Rohr, A. K., Hofer, A., Furrer, E., Tomter, A. B., Andersson, K. K., Sahlin, M., and Sjöberg, B. M. (2011) NrdH-Redoxin protein mediates high enzyme activity in manganese-reconstituted ribonucleotide reductase from *Bacillus anthracis*. *J. Biol. Chem.* 286, 33053–33060.

(28) Tomter, A. B. (2010) Spectroscopic Studies of the Ribonucleotide Reductase R2-subunit from Mammals, Virus, and Bacteria, In *Faculty of Mathematics and Natural Sciences*, University of Oslo, Oslo, Norway.

(29) Zhang, Y., and Stubbe, J. (2011) *Bacillus subtilis* class Ib ribonucleotide reductase is a dimanganese(III)-tyrosyl radical enzyme. *Biochemistry* 50, 5615–5623.

(30) Hogbom, M., Huque, Y., Sjöberg, B. M., and Nordlund, P. (2002) Crystal structure of the di-iron/radical protein of ribonucleo-

tide reductase from *Corynebacterium ammoniagenes*. *Biochemistry* 41, 1381–1389.

(31) Solomon, E. I., Brunold, T. C., Davis, M. I., Kemsley, J. N., Lee, S. K., Lehnert, N., Neese, F., Skulan, A. J., Yang, Y. S., and Zhou, J. (2000) Geometric and electronic structure/function correlations in non-heme iron enzymes. *Chem. Rev.* 100, 235–349.

(32) Uppsten, M., Davis, J., Rubin, H., and Uhlin, U. (2004) Crystal structure of the biologically active form of class Ib ribonucleotide reductase small subunit from *Mycobacterium tuberculosis*. *FEBS Lett.* 569, 117–122.

(33) Boal, A. K., Cotruvo, J. A., Stubbe, J., and Rosenzweig, A. C. (2012) The dimanganese(II) site of *Bacillus subtilis* class Ib ribonucleotide reductase. *Biochemistry* 51, 3861–3871.

(34) Henderson, R. (1990) Cryoprotection of protein crystals against radiation-damage in electron and x-ray diffraction. *Proc. R. Soc. London, Ser. B* 241, 6–8.

(35) Hersleth, H.-P., and Andersson, K. K. (2011) How different oxidation states of crystalline myoglobin are influenced by X-rays. *Biochim. Biophys. Acta, Proteins Proteomics* 1814, 785–796.

(36) Griese, J. J., and Hogbom, M. (2012) X-ray reduction correlates with soaking accessibility as judged from four non-crystallographically related diiron sites. *Metallomics* 4, 894–898.

(37) Sigfridsson, K. G. V., Chernev, P., Leidel, N., Popovic-Bijelic, A., Graslund, A., and Haumann, M. (2013) Rapid X-ray photoreduction of dimetal-oxygen cofactors in ribonucleotide reductase. *J. Biol. Chem.* 288, 9648–9661.

(38) Tomter, A. B., Bell, C. B., Rohr, A. K., Andersson, K. K., and Solomon, E. I. (2008) Circular dichroism and magnetic circular dichroism studies of the ferrous site of the class Ib ribonucleotide reductase from *Bacillus cereus*: Comparison to the class Ia enzymes. *Biochemistry* 47, 11300–11309.

(39) Strand, K. R., Karlsen, S., Kolberg, M., Rohr, A. K., Gorbitz, C. H., and Andersson, K. K. (2004) Crystal structural studies of changes in the native dinuclear iron center of ribonucleotide reductase protein R2 from mouse. *J. Biol. Chem.* 279, 46794–46801.

(40) Ubbink, M. (2012) Dynamics in transient complexes of redox proteins. *Biochem. Soc. Trans.* 40, 415–418.

(41) Nordlund, P., and Eklund, H. (1993) Structure and function of the *Escherichia coli* ribonucleotide reductase protein R2. *J. Mol. Biol.* 232, 123–164.

(42) Smith, P., Zhou, B. S., Ho, N., Yuan, Y. C., Su, L., Tsai, S. C., and Yen, Y. (2009) 2.6 Ångstrom X-ray crystal structure of human p53R2, a p53-inducible ribonucleotide reductase. *Biochemistry* 48, 11134–11141.

(43) Wilmot, C. M., Sjogren, T., Carlsson, G. H., Berglund, G. I., and Hajdu, J. (2002) Defining redox state of X-ray crystal structures by single-crystal ultraviolet-visible microspectrophotometry. *Methods Enzymol.* 353, 301–318.

(44) Rofougaran, R., Crona, M., Vodnala, M., Sjöberg, B. M., and Hofer, A. (2008) Oligomerization status directs overall activity regulation of the *Escherichia coli* class Ia ribonucleotide reductase. *J. Biol. Chem.* 283, 35310–35318.

(45) Uppsten, M., Farnegardh, M., Domkin, V., and Uhlin, U. (2006) The first holocomplex structure of ribonucleotide reductase gives new insight into its mechanism of action. *J. Mol. Biol.* 359, 365–377.

(46) Ando, N., Brignole, E. J., Zimanyi, C. M., Funk, M. A., Yokoyama, K., Asturias, F. J., Stubbe, J., and Drennan, C. L. (2011) Structural interconversions modulate activity of *Escherichia coli* ribonucleotide reductase. *Proc. Natl. Acad. Sci. U.S.A.* 108, 21046–21051.

(47) Magnusson, K. E., and Edebo, L. (1976) Influence of cell concentration, temperature, and pressure performance on flow characteristics and disintegration in freeze-pressing of *Saccharomyces cerevisiae* with X-press. *Biotechnol. Bioeng.* 18, 865–883.

(48) Powell, H. R. (1999) The Rossmann Fourier autoindexing algorithm in MOSFLM. *Acta Crystallogr., Sect. D: Biol. Crystallogr.* 55, 1690–1695.

(49) Evans, P. (2006) Scaling and assessment of data quality. *Acta Crystallogr., Sect. D: Biol. Crystallogr.* 62, 72–82.

(50) Evans, P. R. (2011) An introduction to data reduction: space-group determination, scaling and intensity statistics. *Acta Crystallogr., Sect. D: Biol. Crystallogr.* 67, 282–292.

(51) Winn, M. D., Ballard, C. C., Cowtan, K. D., Dodson, E. J., Emsley, P., Evans, P. R., Keegan, R. M., Krissinel, E. B., Leslie, A. G. W., McCoy, A., McNicholas, S. J., Murshudov, G. N., Pannu, N. S., Potterton, E. A., Powell, H. R., Read, R. J., Vagin, A., and Wilson, K. S. (2011) Overview of the CCP4 suite and current developments. *Acta Crystallogr., Sect. D: Biol. Crystallogr.* 67, 235–242.

(52) McCoy, A. J., Grosse-Kunstleve, R. W., Storoni, L. C., and Read, R. J. (2005) Likelihood-enhanced fast translation functions. *Acta Crystallogr., Sect. D: Biol. Crystallogr.* 61, 458–464.

(53) Arnold, K., Bordoli, L., Kopp, J., and Schwede, T. (2006) The SWISS-MODEL workspace: a web-based environment for protein structure homology modelling. *Bioinformatics* 22, 195–201.

(54) Kiefer, F., Arnold, K., Kunzli, M., Bordoli, L., and Schwede, T. (2009) The SWISS-MODEL Repository and associated resources. *Nucleic Acids Res.* 37, D387–D392.

(55) Murshudov, G. N., Vagin, A. A., and Dodson, E. J. (1997) Refinement of macromolecular structures by the maximum-likelihood method. *Acta Crystallogr., Sect. D: Biol. Crystallogr.* 53, 240–255.

(56) Emsley, P., and Cowtan, K. (2004) Coot: model-building tools for molecular graphics. *Acta Crystallogr., Sect. D: Biol. Crystallogr.* 60, 2126–2132.

(57) Murray, J. W., Garman, E. F., and Ravelli, R. B. G. (2004) X-ray absorption by macromolecular crystals: the effects of wavelength and crystal composition on absorbed dose. *J. Appl. Crystallogr.* 37, 513–522.

(58) Paithankar, K. S., Owen, R. L., and Garman, E. F. (2009) Absorbed dose calculations for macromolecular crystals: improvements to RADDPOSE. *J. Synchrotron Radiat.* 16, 152–162.

(59) Delano, W. L. (2002) *The PyMOL Molecular Graphics System*, DeLano Scientific, San Carlos, CA.

(60) Ho, B. K., and Gruswitz, F. (2008) HOLLOW: Generating accurate representations of channel and interior surfaces in molecular structures. *BMC Struct. Biol.* 8, 49.

(61) Owen, R. L., Pearson, A. R., Meents, A., Boehler, P., Thominet, V., and Schulze-Briese, C. (2009) A new on-axis multimode spectrometer for the macromolecular crystallography beamlines of the Swiss Light Source. *J. Synchrotron Radiat.* 16, 173–182.

Supporting Information for

Crystal Structure of *Bacillus cereus* Class Ib Ribonucleotide Reductase Di-iron NrdF in Complex with NrdI

Marta Hammerstad, Hans-Petter Hersleth, Ane B. Tomter, Åsmund K. Røhr,
and K. Kristoffer Andersson

Department of Biosciences, University of Oslo, P.O.Box 1066 Blindern, NO-0316 Oslo,
Norway

TABLE S1. Data Collection and Refinement Statistics

	<i>Bc apo-NrdF-1</i>	<i>Bc apo-NrdF-2</i>
Crystal data		
Space group	C2	P2 ₁
<i>a, b, c</i> (Å)	121.0/68.2/87.1	69.1/53.9/91.2
α, β, γ (°)	90.0/106.0/90.0	900/110.9/90.0
Crystal size (μm^3)	50×50×100	20×50×50
Data collection		
X-ray source	ESRF ID14-1	ESRF ID14-1
Wavelength (Å)	0.9334	0.9334
Flux (photons/sec)	12·10 ⁹	12·10 ⁹
Beam size (μm^2)	100×100	100×100
Total exposure (sec)	1950	1924
Absorbed X-ray dose (MGy)	0.74	0.72
Resolution range (Å)	34.2-2.2	34.3-2.0
Temperature (K)	100	100
Completeness (%) ^a	99.4/99.9	83.983.3
Redundancy ^a	3.3/3.3	2.3/2.3
<i>I</i> / <i>sd(I)</i> ^a	11.1/3.5	5.7/2.1
<i>R</i> _{Sym} ^{ab}	9.8/41.9	12.9/46.8
Refinement statistics		
<i>R</i> _{Work} (%) ^c	17.6	20.8
<i>R</i> _{Free} (%) ^d	24.3	26.0
Model content		
Amino acids	587	575

Fe ions (occupancy)	1 (25%)	2 (25%)
Water molecules	176	145
Molecules per asu	2	2
Solvent content (%)	49.3	46.4
Unmodelled residues	301-322 (Monomer1), 288-322 (Monomer2)	288-322 (Monomer1), 289-322 (Monomer2)
Volume not occupied by model (%)	39.8	35.7
Model analysis		
Mean overall isotropic <i>B</i> -factor (Å ²)	25.6	16.4
Ramachandran plot: ration in most favoured/other allowed regions (%)	95.3/4.7	96.8/3-2
Estimated overall co-ordinate error based on R work/ maximum likelihood (Å)	0.25/0.15	0.26/0.15
Rmsd bonds (Å) / angles (°)	0.018/2.006	0.015/1.78
PDB code	4BMQ	4BMR

^a The value before the backlash is for all data, and the value after the backlash is for the data in the highest resolution shell

$$^b R_{\text{Sym}} = \frac{\sum |I - \langle I \rangle|}{\sum I}$$

$$^c R_{\text{Work}} = \frac{\sum (|F_{\text{obs}} - F_{\text{calc}}|)}{\sum |F_{\text{obs}}|}$$

^d R_{Free} is the R_{Work} calculated on the 5% reflections excluded for refinement

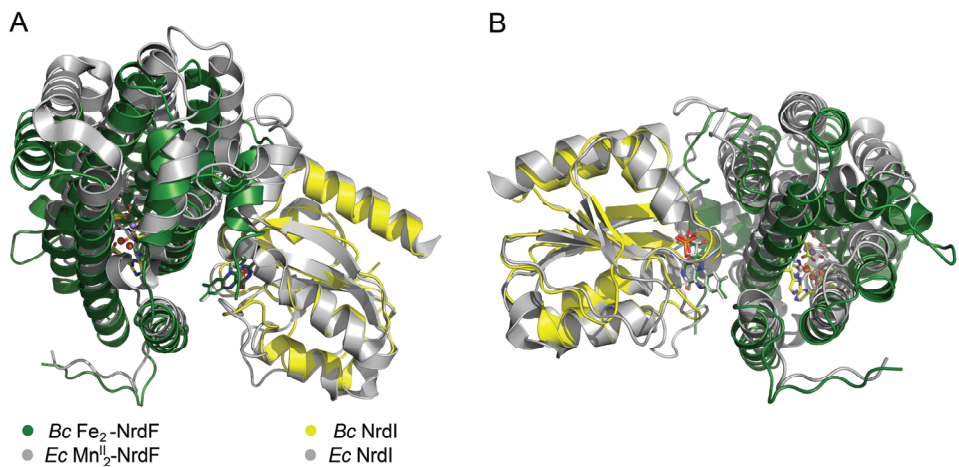


FIGURE S1. Overlay of *Bc* and *Ec* NrdI-NrdF crystal structures, based on structural alignment of the NrdIs. The overlays are shown in different orientations (A and B). A small rotation is observed for the NrdF subunit for the *Bc* structure as compared to the *Ec* structure (PDBid:3N39)¹, when the two NrdI subunits are kept aligned, indicating a rotational difference in the NrdI-NrdF binding in the two crystal structures.

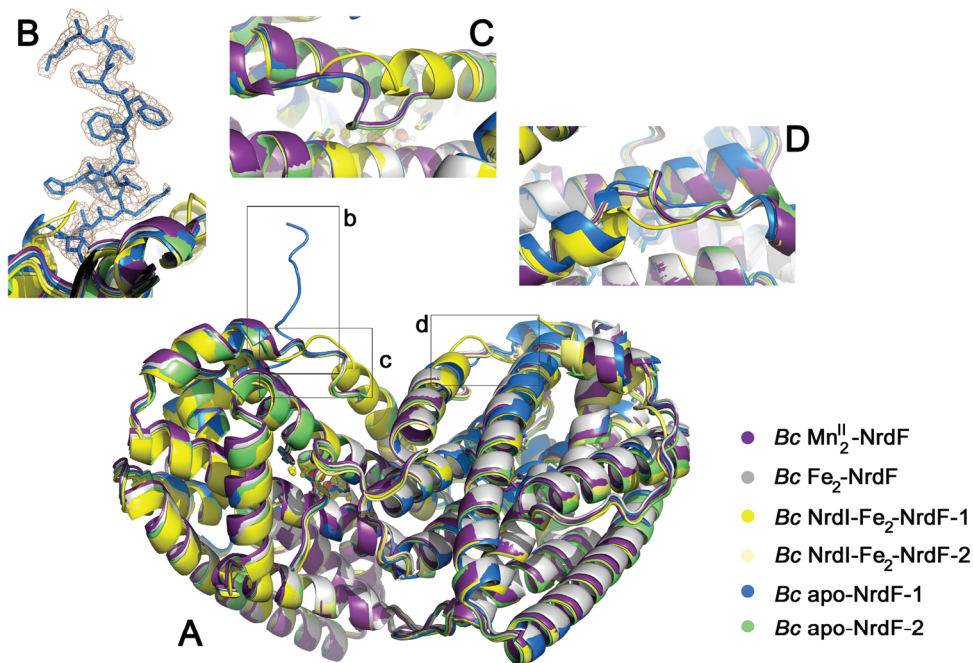


FIGURE S2. The overall crystal structures of *Bc* NrdFs. (A) Overlay of all NrdF structures. (B) 13 additional residues of the flexible C-terminal in monomer A of apo-NrdF-1 are visible in the electron density map, due to different crystal packing. (C) and (D) displays the crystal surface corresponding to residues 25-30, where NrdI-Fe₂-NrdF-1 shows greater helical conformation compared to the other NrdF structures. The same helical conformation is also observed in monomer B of apo-NrdF-1 (D).

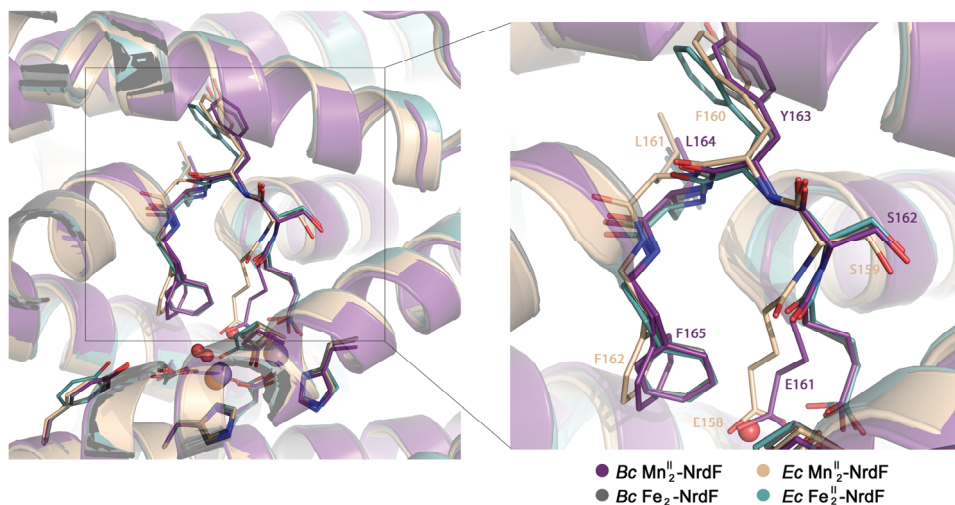


FIGURE S3. Loop alteration in the di-metal cluster vicinity in NrdF. Possible limitation in movement from bidentate to μ -1,3 coordination of Glu 161 (*Bc* numbering) in the di-manganese soaked *Bc* Mn^{II}-NrdF crystal structure, compared to co-crystallized *Ec* Mn^{II}-NrdF crystal structure of NrdF (PDBid:3N37)¹, due to the restricted loop flexibility.

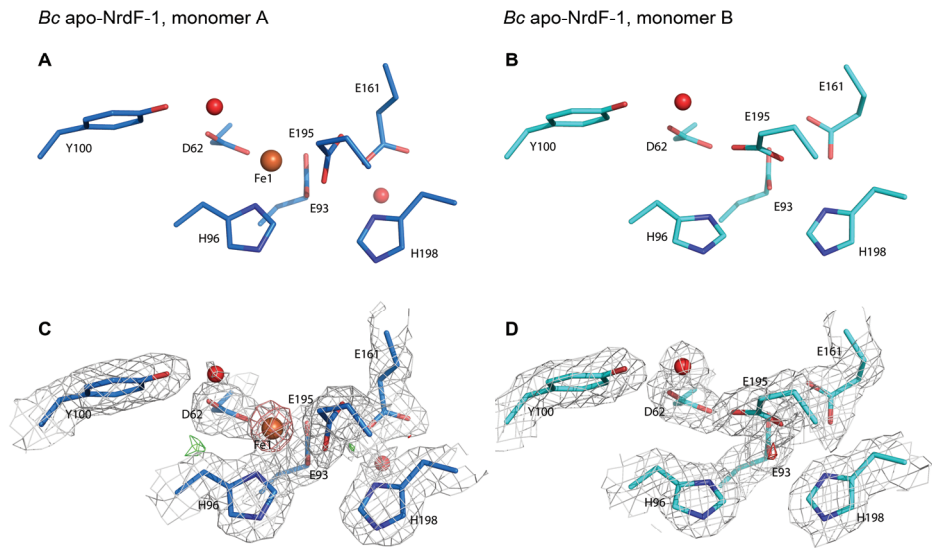


FIGURE S4. Active site environment in the *Bc* apo-NrdF-1 structure. (A) and (C) shows monomer A, while (B) and (D) shows monomer B. Amino acids are represented as sticks and colored by atom type. In monomer A, metal site 1 is modeled with 25% iron occupancy, whereas no metal occupancy is observed for the second metal site (A and C). No metal occupancy is observed in monomer B (B and D). The $2F_o - F_c$ electron density maps (grey) are contoured at 1σ , the $F_o - F_c$ map is shown as green mesh (3σ) and red mesh (-3σ), while the omit map (salmon) surrounding the Fe ions is contoured at 6σ .

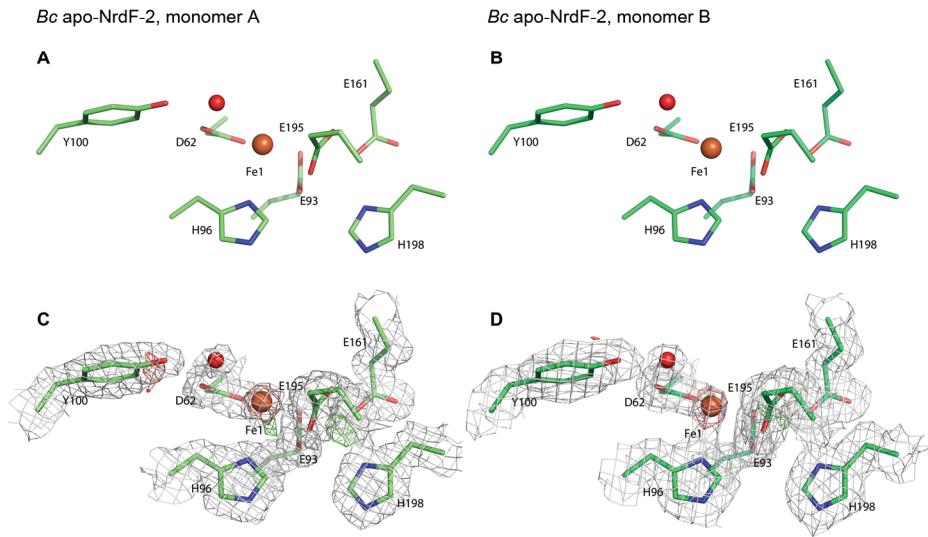


FIGURE S5. Active site environment in the *Bc* apo-NrdF-2 structure. (A) and (C) shows monomer A, while (B) and (D) shows monomer B. Amino acids are represented as sticks and colored by atom type. Metal site 1 in both monomers A (A and C) and B (B and D) have been modeled with 25% iron occupancy. The $2F_o - F_c$ electron density maps (grey) are contoured at 1σ , the $F_o - F_c$ map is shown as green mesh (3σ) and red mesh (-3σ), while the omit map (salmon) surrounding the Fe ions is contoured at 6σ .

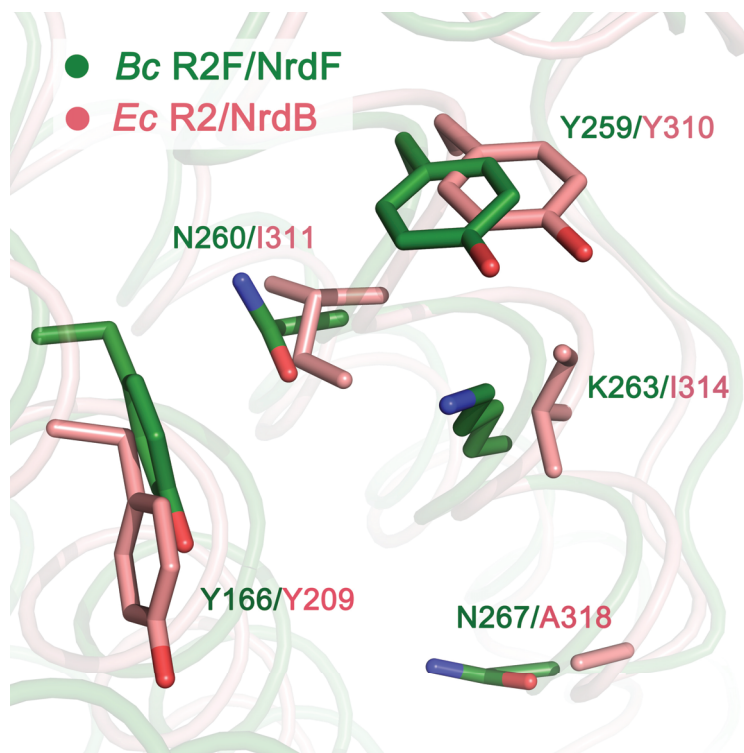


Fig. S6. Residues on the surface of the class Ib *Bc* R2F/NrdF (from NrdI-NrdF) and class Ia *Ec* R2/NrdB (PDBid:1RIB)², showing differences in the core residues shown to be involved in the conserved hydrogen bonding network in the NrdI-NrdF core interface in the class Ib RNR.

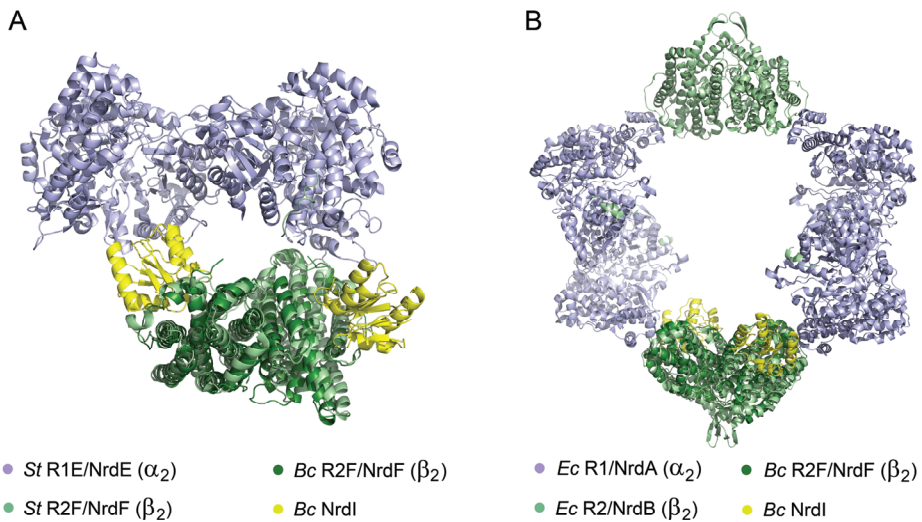


FIGURE S7. The *Bc* NrdI-Fe₂-NrdF complex overlaid with different RNR complexes. (A) The *Bc* NrdI-Fe₂-NrdF overlaid with *St* class Ib crystallographic R1-R2 holoenzyme complex (PDBid:2BQ1)³, and (B) with the *Ec* class Ia $\alpha_4\beta_4$ ring-like structure (PDBid:3UUS)^{4,5}.

REFERENCES

- (1) Boal, A. K., Cotruvo, J. A., Stubbe, J., and Rosenzweig, A. C. (2010) Structural Basis for Activation of Class Ib Ribonucleotide Reductase, *Science* 329, 1526-1530.
- (2) Nordlund, P., and Eklund, H. (1993) Structure and function of the *Escherichia-coli* ribonucleotide reductase protein R2, *J. Mol. Biol.* 232, 123-164.
- (3) Uppsten, M., Farnegardh, M., Domkin, V., and Uhlin, U. (2006) The first holocomplex structure of ribonucleotide reductase gives new insight into its mechanism of action, *J. Mol. Biol.* 359, 365-377.
- (4) Ando, N., Brignole, E. J., Zimanyi, C. M., Funk, M. A., Yokoyama, K., Asturias, F. J., Stubbe, J., and Drennan, C. L. (2011) Structural interconversions modulate activity of *Escherichia coli* ribonucleotide reductase, *Proc. Natl. Acad. Sci. U. S. A.* 108, 21046-21051.
- (5) Hofer, A., Crona, M., Logan, D. T., and Sjöberg, B. M. (2012) DNA building blocks: keeping control of manufacture, *Crit. Rev. Biochem. Mol. Biol.* 47, 50-63.

Tuning of Thioredoxin Redox Properties by Intramolecular Hydrogen Bonds

Åsmund Kjendseth Røhr*, Marta Hammerstad, K. Kristoffer Andersson

Department of Biosciences, University of Oslo, Oslo, Norway

Abstract

Thioredoxin-like proteins contain a characteristic C-x-x-C active site motif and are involved in a large number of biological processes ranging from electron transfer, cellular redox level maintenance, and regulation of cellular processes. The mechanism for deprotonation of the buried C-terminal active site cysteine in thioredoxin, necessary for dissociation of the mixed-disulfide intermediate that occurs under thiol/disulfide mediated electron transfer, is not well understood for all thioredoxin superfamily members. Here we have characterized a 8.7 kD thioredoxin (BC3987) from *Bacillus cereus* that unlike the typical thioredoxin appears to use the conserved Thr8 side chain near the unusual C-P-P-C active site to increase enzymatic activity by forming a hydrogen bond to the buried cysteine. Our hypothesis is based on biochemical assays and thiolate pK_a titrations where the wild type and T8A mutant are compared, phylogenetic analysis of related thioredoxins, and QM/MM calculations with the BC3987 crystal structure as a precursor for modeling of reduced active sites. We suggest that our model applies to other thioredoxin subclasses with similar active site arrangements.

Citation: Røhr ÅK, Hammerstad M, Andersson KK (2013) Tuning of Thioredoxin Redox Properties by Intramolecular Hydrogen Bonds. PLoS ONE 8(7): e69411. doi:10.1371/journal.pone.0069411

Editor: Freddie Salsbury Jr, Wake Forest University, United States of America

Received: May 2, 2013; **Accepted:** June 7, 2013; **Published:** July 23, 2013

Copyright: © 2013 Røhr et al. This is an open-access article distributed under the terms of the Creative Commons Attribution License, which permits unrestricted use, distribution, and reproduction in any medium, provided the original author and source are credited.

Funding: This research was supported by the Steering Board for Molecular Life Sciences at the University of Oslo (EMBLIO), the Norwegian Research Council (grants 177661V30, 138370V30, 214239/F20, 218412/F50, synchrotron related research in the Oslo region, SYGOR), and 539012 Norwegian Cancer Society. The funders had no role in study design, data collection and analysis, decision to publish, or preparation of the manuscript.

Competing Interests: The authors have declared that no competing interests exist.

* E-mail: a.k.rohr@ibv.uio.no

Introduction

Thioredoxin (Trx) and glutaredoxin (Grx) are small ubiquitous proteins acting as cysteine disulfide oxidoreductases in the cell and belong to the thioredoxin superfamily [1–3]. Within this family several classes of proteins have been characterized [4]. They are involved in enzymatic reactions as hydrogen donors [5,6], in redox signaling [7], protein folding [8], and in the defence against oxidative stress [9]. In general, the Trx-like proteins are reduced by NAD(P)H dependent thioredoxin reductases (TrxR) and they usually have a C-G-P-C active site motif. Grx-like proteins typically contain a C-P-Y-C motif and are reduced by the tripeptide glutathione formed by NADPH utilizing glutathione reductases.

The fundamental mechanism for electron transfer from Trx to its substrate was proposed by Kallis and Holmgren in 1980 [10]. As a result of the lowered pK_a value they observed for the N-terminal cysteine thiol (–SH) in the *Escherichia coli* Trx C-G-P-C motif, it was suggested that this thiolate (–S[–]) could perform the initial nucleophilic attack on the substrate disulfide bond. To make the second nucleophilic attack, which dissociates the mixed disulfide intermediate, it was stated that a deprotonation of the buried C-terminal cysteine is necessary. However, the details of this reaction were not discussed. In the following years a number of studies have been focused on the active site thiols and the mechanism behind the proton abstraction from the C-terminal cysteine. It has been suggested that the helix macrodipole [11] or microdipoles [12] are major determinants of Trx cysteine pK_a values, however, these explanations have been challenged in later studies [13]. The largest contributions to shifts in pK_a values are

believed to be intra-protein charge-charge interactions [14], desolvation effects [15], and hydrogen bonding to the deprotonated thiol [16]. A recent study points at the latter effect as the most important [17]. The thiolate form of the N-terminal nucleophilic cysteine positioned at the end of an α -helix, as in Trx, is suggested to be stabilized by intra-protein hydrogen bonding to protein backbone amide protons resulting in a lowered pK_a value [18]. Most studies indicate that the buried C-terminal cysteine pK_a value is around or higher than ~ 8 [10,19–21], thus an explanation for the proton abstraction for this residue is required. A mechanism involving the highly conserved Asp26 and a water molecule functioning as an acid/base catalyst for the buried cysteine has been proposed for *E. coli* and *Acetobacter acetii* Trx [22,23], however, this mechanism is still debated [24,25].

Interestingly, other sub-classes of the Trx superfamily with Trx functionality do not have conserved acidic amino acids analogous to the *E. coli* Trx Asp26. Examples are NrdH-redoxins that reduce the active site of the catalytic subunit NrdE of the bacterial class Ib ribonucleotide reductase (RNR) [26–28] and *Clostridium pasteurianum* Cp9-type thioredoxins that reduce peroxiredoxins (Prx) [29].

The small thioredoxin BC3987 from *Bacillus cereus* having a significant amino acid sequence similarity with both NrdH and Cp9-redoxins can reduce class Ib RNR in both *B. cereus* and *B. anthracis* [30]. However, the most efficient and likely *in vivo* class Ib RNR reductant in those species is TrxA [31].

Here, we discuss how intramolecular hydrogen bonds can affect deprotonation of the active site cysteines. Substituting the conserved Thr8 that is close to the active site with Ala has altered the hydrogen bond network and the effect of this has been

characterized. We have also performed a phylogenetic analysis comparing the amino acid sequence of BC3987 to homologs collected from a range of bacterial species to elucidate which amino acid(s) that contribute to the perturbation of the C-terminal buried cysteine pK_a value. The crystal structure of oxidized BC3987 was solved and we have related the results from the phylogenetic analysis to structural features, enabling us to map parts of the protein involved in hydrogen bonds near the active site. Finally, because no structure of reduced BC3987 was obtained, we have modeled the reduced active site using quantum mechanical/molecular mechanical (QM/MM) calculations and rationalized the experimentally observed and unusually low pK_a value of the C-terminal buried cysteine through hydrogen bonding to the conserved Thr8 residue. Based on these results, we suggest a general reaction mechanism for the BC3987-like category of thioredoxins.

Experimental

Cloning, Mutagenesis, Expression, and Purification of BC3987

Genomic DNA was isolated from *Bacillus cereus* ATCC 14579 using the DNEasy kit from Qiagen. The coding sequence of BC3987 including restriction sites for *Xba*I and *Hind*III was amplified by PCR using the forward primer 5'-CCCTCTA-GAAATAATTTTGTTTAACTTTAAGAAGGAGATATACATATGAAAAAAATGAGGTTTAT-3' and backward primer 5'-AGGAAGCTTAAAAGTTATTCCTATATTGAGTAGTTG-3'. The gene was cloned into the pET-22b plasmid (Novagen) and transformed into competent BL21 (DE3) Gold cells (Stratagene). The T8A mutation of BC3987 was generated with the primer 5'-GAAAAAAATGAGGTTTATGCACAACCC-GATTGTCCGCC-3' using the QuikChange Site-Directed Mutagenesis Kit from Stratagene. A 5 mL overnight culture of BC3987 expressing cells was diluted 1:200 in 1 litre Terrific Broth medium containing 100 µg/mL ampicillin and grown until O.D._{600 nm} = 0.7–0.8 at 37°C. The cultures were cooled on ice until the temperature reached 15°C and then induced by adding IPTG to a final concentration of 1 mM and the left for 15–16 hours at 20°C in a shaker before harvesting.

Approximately 30 grams of bacteria containing BC3987 was lysed utilizing an X-press [32] and dissolved in 100 mL 100 mM Tris/HCl pH 7.5 containing 10 mM EDTA before centrifugation. DNA was precipitated by adding streptomycin sulfate to a final concentration of 2.5% (w/v). BC3987 was precipitated with 60% ammonium sulfate (0.43 mg/mL). Precipitated protein was dissolved in 50 mM Tris/HCl pH 7.5 and desalted using a HiTrap Desalting column (GE Healthcare). The desalted protein solution was applied to a 1 mL Resource Q anion exchange column (GE Healthcare) and the BC3987 was eluted using a 20 mL 0–400 mM KCl, 50 mM Tris/HCl pH 7.5, gradient. As a final polishing step the protein was purified using a Superdex 200 column (GE Healthcare).

Protein Analysis and Concentration Determination

The homogeneity of the proteins was analyzed using a Superdex 200 gel filtration column and by SDS gel electrophoresis utilizing the PhastSystem (GE Healthcare) equipped with an 8–25% gradient gel. Protein purity was estimated to >95% by visual inspection of gels. The extinction coefficient of BC3987 was determined using the Edelhoch method [33], yielding a value of ε_{BC3987}, 280 nm = 8200 M⁻¹cm⁻¹.

Insulin Reduction Assay

The thioredoxin catalyzed reduction of insulin by dithiothreitol (DTT) probes the efficiency of Trx - insulin reduction mechanism. First, both proteins were incubated with 10 mM DTT for 30 minutes and then passed through a HiTrap Desalting column equilibrated with 100 mM potassium phosphate buffer pH 6.5, 2 mM EDTA. The experiments was carried out in 96-well microtiter plates containing 160 µM insulin, 100 mM potassium phosphate buffer pH 6.5, 2 mM EDTA, 1 mM DTT, and 10 µM wt or T8A BC3987 [34]. A Tecan Sunrise plate reader was used to monitor light scattering at 580 nm turbid solution of reduced insulin.

Estimation of Active Site Cysteine pK_a Values

To estimate the pK_a values of the active site cysteines the absorbance of the thiolate anion at 240 nm was followed during a pH titration [35–37]. To prepare the reduced wt and T8A mutant BC3987 protein and their corresponding oxidized references, the proteins were incubated with 200 mM DTT or 100 mM diamide for 1 hour, respectively. Excess DTT and diamide was removed using a HiTrap Desalting column (GE Healthcare) equilibrated with a polybuffer with pH 9.3 consisting of 1 mM of each sodium phosphate, sodium citrate, sodium borate, and 0.1 mM EDTA. Spectra of 10–25 µM oxidized and reduced BC3987 was recorded with a HP 8452 diode array spectrophotometer between 200 and 600 nm and corrected for the absorbance difference between the two cuvettes, base line drift, and finally the 240 nm absorbance values were normalized against the 280 nm values. The pH was varied from 9.3 to 2.8 by adding 2–4 µl of 25 mM HCl and measured using a PHM240 pH meter (Radiometer Analytical) equipped with a PHM 4000-8 pH electrode. The equation $\epsilon_{240 \text{ nm}} = A_0 + A_1/(1+10^{x-pK_{a1}}) + A_2/(1+10^{x-pK_{a2}})$ was used to estimate the pK_a values by fitting the curves in Figure 1.

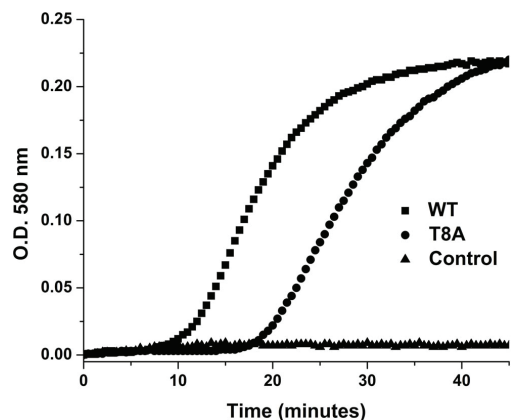


Figure 1. Estimation of active site cysteines pK_a values in wild type and mutant BC3987. The pK_a values of the active site cysteines in BC3987 were estimated by pH titration resulting in pK_a values 5.1 and 7.2 for the wild type and 7.2 for the T8A mutant. A cuvette containing 25 µM reduced protein in 1 mM polybuffer pH 9.3 was added 2 µL aliquots of 25 mM HCl and the change in thiolate absorption at 240 nm were followed with a UV-vis spectrometer. doi:10.1371/journal.pone.0069411.g001

Phylogenetic Analysis

The NrdH amino acid sequences collected from different bacterial divisions were obtained from the Integrated Microbial Genomes (IMG) website [38]. All the NrdH-redoxin amino acid sequences contain the C-[IMV]-Q-C motif and are located in a class Ib RNR operon. Sequences homologous to the Cp9-redoxin found in the anaerobe *C. pasteurianum*, often annotated as YruB proteins after its initial discovery [39], encoding proteins in the range of 75–80 amino acids were downloaded from the UniProt Knowledgebase [40]. Multiple sequence alignment was performed by MAFFT [41] before manual editing using GeneDoc 2.7 (Nicholas and Nicholas, NRBSC). Columns containing gaps and amino acids in the ranges 1–6 and 80–87 in the alignment (Figure S1) were excluded from the phylogenetic analysis. The program Treefinder [42] was used to estimate the substitution model and reconstruct a bootstrapped phylogenetic tree with 1000 replicates at a 50% consensus level utilizing the Maximum Likelihood (ML) algorithm. A second bootstrapped phylogenetic analysis was performed using the Neighbour Joining algorithm included in ClustalX 2.0 [43] using 1000 replicates.

Crystallization of BC3987

Plate formed crystals were obtained with the Index screen (Hampton Research, CA, USA) condition 55, at room temperature. BC3987 (18 mg/mL) in 15 mM Tris/HCl pH 7.5 was mixed 1:1 with reservoir solution (0.1 M HEPES pH 7.5, 50 mM MgCl₂, and 30% (w/v) polyethylene glycol monomethyl ether 550). Crystals of approximately 400 × 400 × 30 μm³ appeared after 1–2 days. Crystals of mutant BC3987 were obtained at the same conditions as the wild type. So far, crystals with reduced active sites motif have not been obtained when soaking with reductants as DTT and sodium dithionite.

X-ray Data Collection

Data were collected at the Swiss-Norwegian Beam Line (SNBL, BM01 A) and ID29 at the European Synchrotron Radiation Facility (ESRF), Grenoble, France at 110 K. The protein crystals were flash frozen after 30 seconds incubation in a cryo solution consisting of PEG 400 and reservoir solution in a 1:6 ratio. The crystals belong to the monoclinic P2₁ space group and have two protein molecules in the asymmetric unit. Data were integrated with iMOSFLM [44] before scaling and merging with SCALA [45].

Structure Determination and Refinement

The program PHASER [45,46] was used to solve the structure of the wild type protein by molecular replacement using a polylalanine search model generated from the *Corynebacterium ammoniagenes* NrdH protein structure [47], PDB ID 1R7H, which has 32% amino acid sequence identity with BC3987. Two rounds of simulated annealing with CNS [48] were followed by several cycles of model building using COOT [49], ARP/wARP [50], and structure refinement in REFMAC5 [51]. The mutant BC3987 crystal structures were solved using the wild type structure as start model. The figures were prepared with PyMOL (W. L. DeLano (2002) PyMOL, DeLano Scientific, San Carlos, CA). The atomic coordinates and structure factors have been deposited in the Protein Data Bank, Research Collaboratory for Structural Bioinformatics, Rutgers University, New Brunswick, NJ.

QM/MM Calculations Modeling the Reduced Structure

In order to model the reduced active site of BC3987 two-layer ONIOM [52] calculations were performed. The ONIOM

procedure allows part of the protein to be treated by quantum mechanical (QM) methods (the high level layer) while a force field based on classical mechanics (MM) is used to describe the rest of the protein (the low level layer). All calculations were executed through the Biportal (www.biportal.uio.no) using Gaussian 03, Revision D.02 [53], at TITAN, the computing facility at the University of Oslo. The crystal structure of BC3987 was used as a starting point for modeling the reduced active site. All water molecules were deleted from the structure and hydrogen atoms were added using *GaussView 4.1* (Gaussian, Inc.). The protonated structure was then solvated by adding a 6 Å layer of TIP3P water molecules using the Amber tools 1.2 package [54] and subjected to geometry optimization. In this model preparation step, the coordinates of protein hydrogen atoms and water molecules were geometry optimized using the Amber force field as implemented in Gaussian 03 while keeping the non-hydrogen protein atoms frozen.

In the resulting structure the dihedral angles of Cys12 and Cys15 defined by the atoms N-C_α-C_β-S_γ were changed by 9° and 46°, respectively, increasing the distance between the two S_γ atoms from 2.14 to 3.63 Å. The geometry optimized version of this altered structure is from now on referred to as **Model I**. The precursor of **Model II** has an additional modification, the dihedral angle N-C_α-C_β-O_γ of Thr8 was changed from 68.9 to 160°, making it resemble the Thr rotamer observed in *E. coli* NrdH (PDBid:1H75) [55] and *C. ammoniagenes* NrdH (PDBid:1R7H) [47].

Both models were geometry optimized at the ONIOM(R-B3LYP/6-31+G(d,p):UFF) level using the charge equilibrium (QE:q) method [56] to assign atomic partial charges. During these calculations, both Cys12 and Cys15 were in their thiolate forms. The high level layer included Tyr7(C) – Gln9(C_α), the Cys12 side chain, Pro14(C) – Cys15 C_α, including Cys15 H_{C_α} and side chain, and the Thr53 side chain. All atoms in the high level layer were allowed to move while the coordinates of protein atoms in the low level layer, except Cys12 H_{C_α}, C_α, C, and O and Cys15 C and O, were kept frozen during geometry optimization. The water molecules within a radius of 15 Å of the Cys12 S_γ-atom were also allowed to move.

Results

Characterization of the C-P-P-C Active Site Cysteine pK_a Values

Different subclasses of the thioredoxin superfamily have nucleophilic cysteine pK_a values that correspond to their biological function. Thus, this is an important parameter when classifying new member of this superfamily.

When estimating the pK_a values of the active site cysteines in wild type BC3987 and the T8A mutant, DTT reduced samples were compared with diamide oxidized references. A plot of the thiolate extinction coefficient values plotted against the measured pH is shown in Figure 1. Interestingly, it was observed that the extinction coefficient difference at 240 nm ($\Delta\epsilon_{240\text{ nm}}$) due to the thiolate anion was 7–8000 M⁻¹cm⁻¹. This was a surprising result as an expected $\Delta\epsilon_{240\text{ nm}}$ value of about 3500–4000 M⁻¹cm⁻¹ is typical for a single thiolate [57–59]. One possible explanation for this observation is that both cysteines in the reduced C-P-P-C active site have lowered pK_a values. The pH-titration curves for wild type and T8A BC3987 in Figure 1 are similar in the pH interval 6.5–9, indicating that the nucleophilic Cys12 pK_a value is not affected by the T8A mutation. However, in the pH range 6.5–3 there are clear differences. First, the T8A mutant is not stable below pH 5.4 and precipitates. Second, the wild type curve has a

shoulder between pH 4 and 6.5, indicating a titratable thiolate with a lowered $\Delta\epsilon_{240\text{ nm}}$. A lowered $\Delta\epsilon_{240\text{ nm}}$ for the buried Cys15 can be rationalized because the absorbance maximum of thiolates depends on the polarity of the solution, shifting to lower wavelengths with decreasing polarity. Following the reasoning above, the wild type BC3987 has two titratable thiolates with pK_a values 5.1 and 7.2 while the T8A mutant has one thiolate with a pK_a value of 7.2 and a second thiolate that behave different from the wild type.

BC3987 Wild Type and the T8A Mutant Reduction of Insulin Disulfides

In the insulin reduction assay, thioredoxin catalyze the reduction of insulin by DTT and the light scattering of reduced insulin is measured. As shown in Figure 2, the control reaction with insulin and DTT is very slow compared to the wild type and T8A mutant BC3987 catalyzed reactions. The efficiency of thioredoxin insulin reduction is measured in this assay, and from the curves in Figure 2 it can be concluded that the wild type BC3987 has a different reactivity towards the substrate compared to the T8A mutant. The lag-time before any precipitated insulin is observed is much longer for the T8A mutant, and the slope of the curve after the lag-period is slightly steeper for the wild type enzyme.

Phylogenetic Analysis

The BC3987 homologs within the *B. cereus* group have 28–32% sequence identity to NrdH-redoxins and 37% sequence identity to the *Clostridium novyi* Cp9-redoxin homolog. Thus, it was of interest to compare these three groups that all belong to the thioredoxin superfamily. The analysis was performed using the method of Maximum Likelihood with a WAG [60] substitution model, based on the AICc criterion [61,62] with optimized frequencies, proposed by the Treefinder program. In the phylogenetic tree shown in Figure 3, a node separates the three groups at a 94% consensus level. The tip-to-tip distances between the node and the three groups, *Bacillus cereus* group BC3987 homologs (Blue), Cp9

homologs (Green), and NrdH-redoxins (Red) are 0.47, 0.44, and 0.50 substitutions per site, respectively.

A multiple amino acid sequence alignment of the *B. cereus* group BC3987 homologs, NrdH-redoxins, and Cp9 homologs included in the phylogenetic analysis shows that several residues are highly conserved for all classes in addition to the cysteines in the C-x-x-C motif (Figure S1). Using the amino acid numbering from BC3987 the Pro54, Gly65, and Phe66 are conserved for all the sequences included in the alignment. In addition, a N-terminal [IV]-X-[ILV]-[YF]-[ST] motif ranging from residue 4 to 8 and a [LI] residue at position 71 seems to be conserved within all classes. The active site motif (Figure 2, right side) has a larger variation in the Cp9 homologous proteins (C-[PGI]-[PYWQ]-C) than the NrdH-redoxins (C-[VMI]-Q-C), however, the Grx-like C-P-[YW]-C motif seems to be the most common within the Cp9 group. BC3987 and Cp9 homologous sequences have an insert at position 44 that is a Leu or Met residue that is not present in the NrdH proteins (Figure S1). The other *B. cereus* group BC3987 homologs also have this insert, supporting the co-classification with Cp9. From these results we suggest that the *Bacillus* genus BC3987 homologs, Cp9 homologs, and NrdH-redoxins form three evolutionary separated groups.

However, due to the occurrence of the same amino acid insertion and the higher sequence identity observed for the *Bacillus* genus BC3987 homolog group and the Cp9 homologs one might expect a closer structural, and perhaps functional, relationship for these two groups compared to the NrdH-redoxins.

Identification of Conserved Amino Acids Preceding the C-x-x-C Site in Thioredoxin-like Proteins

In general the local environment of the active site cysteines is considered to be very important with regard to reactivity and redox potential of Trx. Within the 6 amino acids preceding the C-x-x-C motif there are often highly conserved Asp, Thr, and Ser residues that have been shown to affect the activity of the enzyme or are suggested to do so. These residues are located on a β -strand that folds back on the active site, thus the amino acid side chains in position 2, 4, and 6 can point towards the buried cysteine. All proteins in the IMG database having less than 160 amino acids and containing either x(6)-C-G-P-C (Trxs), x(6)-C-P-[FYW]-C (Grxs), x(6)-C-[VIM]-Q-C (NrdH-redoxins), or x(6)-C-P-P-C motifs (PROSITE syntax used to describe motifs) and being annotated as either Trxs, Grxs, or NrdH-redoxins, have been analyzed with focus on the [DE]-x-[ST]-x(3) motif preceding the active site (Table 1).

Quality of the BC3987 Crystal Structure

The BC3987 wild type and T8A mutant structures were refined to 1.4 and 1.18 Å, respectively. In the wild type structure residues 1–76 and 3–75 are observed in chain A and B, respectively. Chain A shows the overall highest quality with residues 1–76 visible in the electron density map, while residues Lys35, Lys36, Phe66, Glu69, and Gln72 in chain B lack density at a few side chain atoms. In the T8A mutant structure, all residues 1–78 are visible in the electron density map of the corresponding high quality chain. In the other chain, residues 3–76 are observed, with lacking density at the side chain atoms of Asn76. Refinement and validation statistics are presented in Table 2.

Overall Structure of BC3987

Like *E. coli* and *C. ammoniagenes* NrdH the BC3987 have a $\alpha/\beta/\alpha$ Trx fold typical for all members of the Thioredoxin superfamily. The structure has a C $_{\alpha}$ RMSD value of 1.26 Å with the *E. coli*

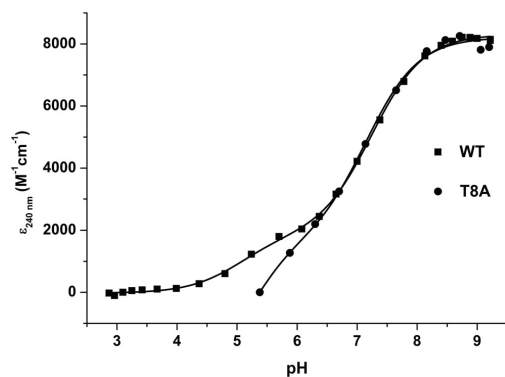


Figure 2. Insulin reduction by wild type and mutant BC3987. In the insulin reduction assay, the rate of insulin disulfide reduction by DTT is enhanced using 10 μM thioredoxin as a catalyst. The wild type BC3987 thioredoxin (■) is more efficient than the T8A mutant (●). The control experiment without thioredoxin shows that the uncatalyzed reaction with DTT is very slow (▲). The concentration of insulin and DTT used in the assay was 160 μM and 1 mM, respectively. The turbidity of the assay solution was monitored at 580 nm (light scattering). doi:10.1371/journal.pone.0069411.g002

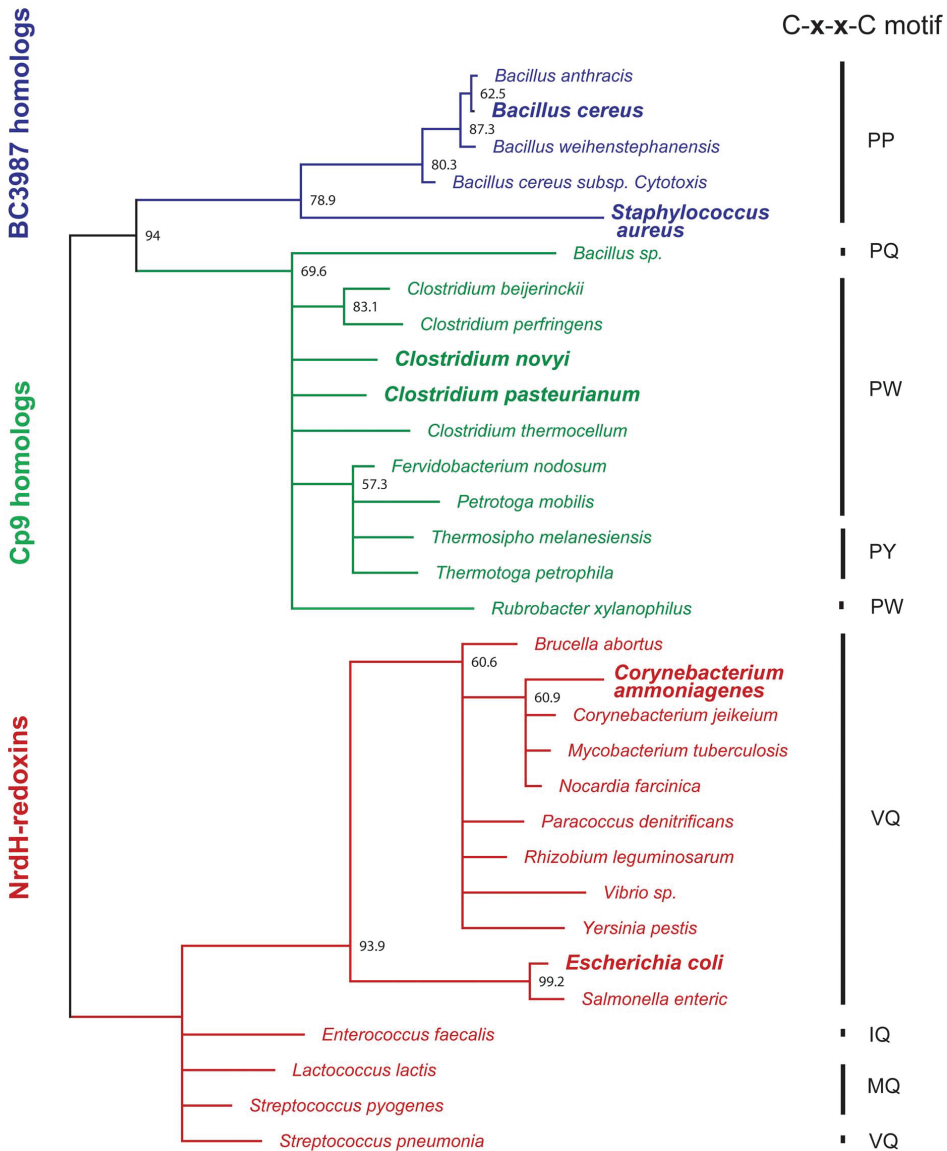


Figure 3. Phylogenetic analysis of thioredoxins similar to BC3987. Bootstrap values obtained at a 50% consensus level using the Maximum Likelihood algorithm with 1000 replicates are shown at the branches of the tree. The evolutionary distances from the node separating the three clusters BC3987 homologs (in blue), Cp9 homologs (in green), and NrdH-redoxins (in red) are 0.47, 0.44, and 0.50 substitutions per site, respectively. Among the BC3987 homologs the active sites always have the -C-P-P-C- motif while the classical glutaredoxin active site motif -C-P-[YW]-C- is prevalent for the Cp9-like proteins. For the NrdH-redoxins, all encoded in a *nrdHIEF* operon, the predominant active site motif is -C-V-Q-C-. Alignment shown in Figure S1 (same color coding). doi:10.1371/journal.pone.0069411.g003

NrdH (PDBid:1H75). Due to the insert of one Leu amino acid at position 44 in the BC3987 protein, the α 2 helix is positioned slightly closer to the β -sheet layer compared to *E. coli* NrdH. The

amino acid insert not found in NrdH-redoxins (Leu44) points into the cavity on the BC3987 surface that resembles the binding site for TrxR described by Lennon *et al.* [63].

Table 1. Categorization of active site motifs in thioredoxin-like proteins (% of sequences)^a.

Active site motif ^b	x-x amino acids			
	Thioredoxin	Glutaredoxin	NrdH	Other
	G-P	P-[FYW]	[VIM]-Q	P-P
x(6)-C-x-x-C	61.1	25.2	8.5	5.2
x(2)-[ST]-x(3)-C-x-x-C	3.0	15.1	8.5	2.7 (2.2 T, 0.5 S)
[DE]-x(5)-C-x-x-C	56.5	0	0	1.3
[DE]x[ST]-x(3)-C-x-x-C	1.5	0	0	0.3

^aAnalysis of 2627 sequences. All sequences between 60 and 160 amino acids in the Integrated Microbial Genomes database (<http://img.jgi.doe.gov>) containing a x(6)-C-x-x-C motif were downloaded. Sequences that were not annotated or did not have a Pfam classification as a member of the thioredoxin superfamily were deleted prior to the analysis.

^bPROSITE syntax (http://au.expasy.org/tools/scanprosite/scanprosite-doc.html#pattern_syntax) is used to describe the amino acid motifs preceding the N-terminal active site Cys.

doi:10.1371/journal.pone.0069411.t001

The C-P-P-C Active Site Motif

The BC3987 protein has a C-P-P-C active site motif that differs from what is typically observed for Trxs and Grxs. Additionally, the residues Thr8 and Thr53 in the vicinity of the disulfide bridge are possible hydrogen bond partners for the buried C-terminal cysteine (Figure 4A). Contrary to what is seen in the NrdH-redoxins from *E. coli* and *C. ammoniagenes* crystal structures the Thr8 residue in BC3987 has a rotamer where the hydroxyl group

is pointing away from the buried Cys15 S_γ-atom. This orientation of Thr8 is stabilized by a hydrogen bond to a water molecule (HOH34). The proline residues apply restrictions on the protein backbone, making a rigid frame for the active site cysteines. Both proline residues in the BC3987 active site have the trans-conformation with ω -angles of 177° and 176° for the Pro13 and Pro14, respectively. These values fall within the ω -angle standard deviation observed for trans-proline residues with the UP-pucker

Table 2. Crystal data, data collection, and refinement statistics.

Crystal data		
	Wild type	T8A mutant
Space group	P2 ₁	
Crystal parameters	a = 24.7, b = 98.9, c = 25.1	a = 24.4, b = 99.1, c = 25.2
	$\alpha = 90, \beta = 91.8, \gamma = 90$	$\alpha = 90, \beta = 91.6, \gamma = 90$
Data collection		
X-ray source	ESRF, ID29	ESRF, ID29
Resolution (Å) ^a	33–1.4 (1.48–1.4)	24.8–1.18 (1.25–1.18)
Wavelength (Å)	0.975948	0.976273
Temperature (K)	100	100
Completeness (%) ^a	94.3 (93.8)	84.9 (83.1)
Redundancy (%) ^a	2.6 (2.6)	3.1 (3.0)
I/ σ (I) ^a	15.0 (6.1)	13.1 (4.9)
R _{sym} (%) ^b	0.03 (0.11)	0.04 (0.18)
Refinement statistics		
R _{cryst} (%) ^c	18.8	14.4
R _{free} (%) ^d	20.5	19.7
Mean overall isotropic B-factor (Å ²)	19.9	20.8
Ramachandran plot: ration in most favored/other allowed regions (%)		
RMS deviation from standard bond lengths (Å)/angles (°)	0.026/2.44	0.026/2.40
Added waters	98	88
PDB code	3ZUJ	3ZIT

^aValues for outer shell in parenthesis.

^bR_{sym} = $\sum |I - \langle I \rangle| / \sum I$.

^cR_{cryst} = $\sum (|F_{obs}| - |F_{calc}|) / \sum |F_{obs}|$.

^dR_{free} is the R_{cryst} value calculated on the 5% reflections excluded for refinement.

doi:10.1371/journal.pone.0069411.t002

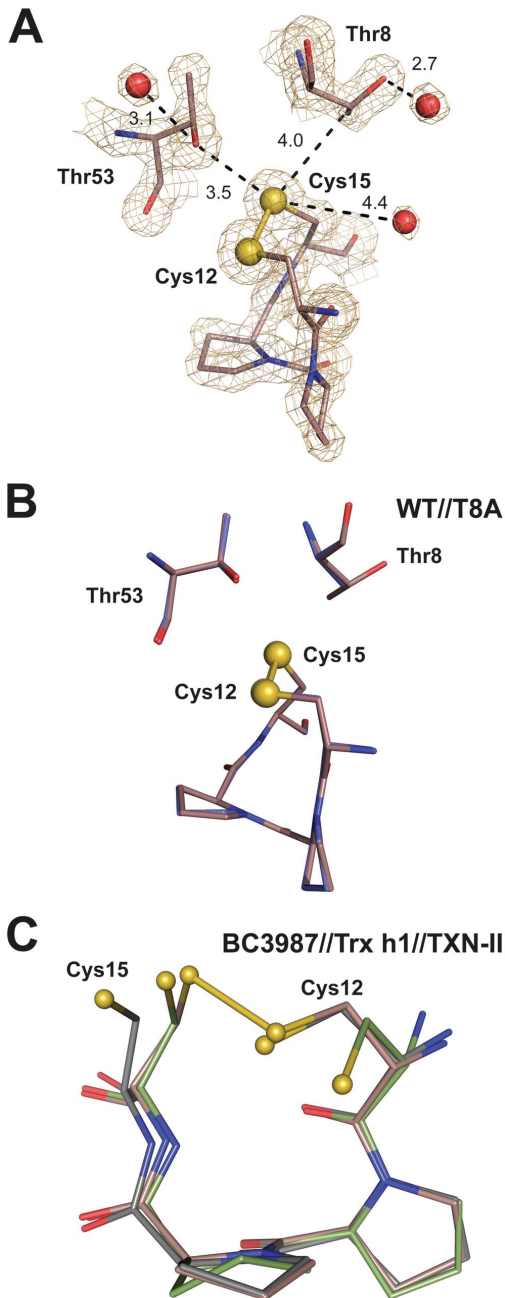


Figure 4. Structure of BC3987 active site. (A) The active site and immediate surroundings in BC3987. Thr8 and Thr53 can possibly form hydrogen bonds to the S_γ-atom of Cys15 upon reduction of the disulfide bridge. The $[2F_o - F_c]$ map is contoured at 1.5σ . (B) The wild

type (in brown) and T8A (in blue) crystal structures have CPPC active sites that superimpose with a RMS value of 0.053 Å. This verifies that the mutation does not disturb the CPPC active site. (C) Comparison of C-P-P-C motifs in oxidized BC3987 (in brown), reduced Tryparedoxin, TXN-II, (in green), and reduced Trx h1 (in grey). From this superimposition, it is suggested that the cysteine side chains and not the backbone undergo the largest structural rearrangement upon reduction of the active site.
doi:10.1371/journal.pone.0069411.g004

[64], indicating that the motif probably is structurally relaxed. The crystal structure of the T8A mutant resembles the wild type structure and the C-P-P-C motifs in these structures superimpose with a RMSD value of 0.053 (Figure 4B). A superimposition of the oxidized C-P-P-C motif in BC3987 and the corresponding reduced C-P-P-C motifs found in Tryparedoxin-II (TXN-II) from *Crithidia fasciculata* (PDBid:1FG4) and Poplar Trx h1 (PDBid:1TI3, model 3) is shown in Figure 4C. The RMS values calculated for all C-P-P-C atoms except Cys-C_β/S_γ are 0.32 and 0.22 Å with Tryparedoxin II and Trx h1, respectively, indicating that the disulfide redox state does not influence the active site conformation notably.

QM/MM Modeling of the Reduced Active Site Motif

Based on the results from the Cys pK_a titration experiments and the different Thr rotamers observed in the crystal structures of BC3987 and the NrdH-redoxins one might speculate that the conserved Thr8 could contribute to lower the buried cysteine pK_a value through hydrogen bonding. In the structure it is apparent that the Gln9 amide proton is within hydrogen bonding distance to the S_γ-atom of Cys15, however, a Thr8 with a rotamer as observed in *E. coli* and *C. ammoniagenes* NrdH-redoxins could also act as a hydrogen bond donor to this atom. Additionally, it was of interest to examine if the variable Thr53 could form a hydrogen bond to the buried cysteine thiolate when BC3987 was in the reduced form.

To be able to investigate the effects of Thr8 and Thr53, a QM/MM modeling approach including the whole protein was chosen. The largest part of the protein (the low layer, cartoon representation in Figure 5A) was modeled by a classical force field, while hybrid density functional theory was used to describe the active site and its immediate surroundings (the high layer, ball-and-stick representation in Figure 5A). Geometrical restraints were applied on the active site to mimic the limited conformational difference between red-ox states observed in Tryparedoxin-II and Poplar Trx h1 (Figure 4C). From the two models of the reduced active site, Model I with Thr8 having the rotamer observed in the BC3987 crystal structure (Figure 5B) and Model II where the conformation of Thr8 resemble the corresponding Thr residue in NrdH-redoxins (Figure 5C), there are several differences. Hydrogen bonding distances within the active site in Model I and II have been summarized in Table 3. Additionally, the pK_a values of the cysteines in both geometry optimized structures were estimated using the program PROPKA 2.0 [17], and the perturbations caused by the individual hydrogen bonds are also shown in Table 3.

In both models the nucleophilic Cys12 side chain is hydrogen bonded to the Cys15 amide proton, rationalizing the perturbed pK_a value of this thiol. It is also clear that the amide proton of Gln9 can form a hydrogen bond to the buried Cys15 thiolate in both Model I and II. A limited perturbation of the variable Thr53 residue on the Cys12 pK_a value is predicted, the effect being similar in magnitude for both models. Indeed, an additional hydrogen bond from Thr8 to the buried cysteine thiolate can be observed in Model II (Figure 5C), resulting in calculated pK_a

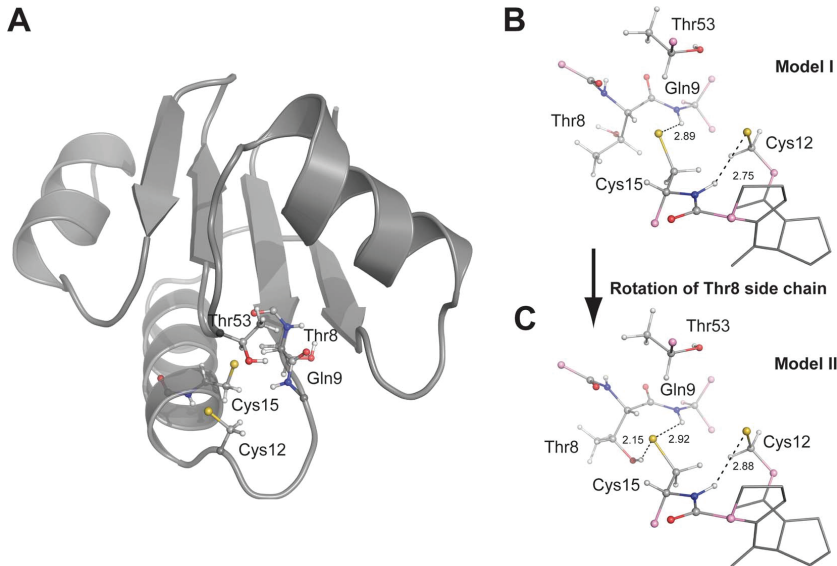


Figure 5. QM/MM models of the BC3987 active site. (A) QM/MM geometry optimized structure of BC3987 showing the quantum mechanical and molecular mechanics regions in ball-and-stick and cartoon representation, respectively. (B) Active site (Model I) where the Thr8 residue has the rotamer observed in the crystal structure. The Cys12 side chain is hydrogen bonded to the Cys15 amide proton. The Gln9 amide proton is a possible hydrogen bond donor to the buried Cys15 thiolate. (C) In this structure (Model II) the Thr8 side chain was rotated to resemble the rotamer observed in *E. coli* and *C. ammoniagenes* NrdH-redoxins prior to geometry optimization. The Thr8 hydroxyl group and Gln9 amide proton appear to form hydrogen bonds to the buried Cys15 side chain while the Cys12 side chain is hydrogen bonded to the Cys15 amide proton. The link atoms connecting the MM and QM layer in B and C are colored pink.
doi:10.1371/journal.pone.0069411.g005

values of 7.1 and 6.5 for Cys12 and Cys15, respectively. The corresponding values for Model I are 7.1 and 8.0, indicating that Model II is most compatible with experimental observations and supporting the hypothesis that Thr8 is involved in the stabilization of the Cys15 thiolate. With respect to computed energies, the high layer B3LYP energy is 8.7 kcal/mol lower for Model II compared to Model I, however, the total ONIOM energy for Model II is 11.8 kcal/mol higher than for Model I. This indicates that effects

from the protein low layer disfavor Model II compared to Model I, while the active site electronic structure in Model II is stabilized by the hydrogen bond between Thr8 and Cys15.

Discussion

The thioredoxin BC3987 found in *B. cereus* ATCC 14579 is conserved among all the members of the *B. cereus* group, including

Table 3. Hydrogen bond distances^a to active site thiolates and their estimated perturbation ΔpK_a^b on the pK_a values.

Donor atom		Thr53-O _γ	Thr8- O _γ	Gln9-N _{amide}	Cys15-N _{amide}	Estimated pK _a
Model I	Cys12	4.38 Å	–	–	3.70 Å	7.1
		–0.19 ^b	–	–	–1.74 ^b	
	Cys15	4.20 Å	–	3.68 Å	–	8.0
		–0.49 ^b	–	–1.07 ^b	–	
Model II	Cys12	4.41 Å	–	5.26 Å	3.80 Å	7.1
		–0.14 ^b	–	–0.08 ^b	–1.70 ^b	
	Cys15	–	3.09 Å	3.71 Å	–	6.4
		–	–1.60 ^b	–1.66 ^b	–	
Experiment	Cys12					7.2
	Cys15					5.1

^aHydrogen bonding distances obtained from the geometry optimized structures Model I and Model II.

^bThe perturbation of the thiolate pK_a values due to hydrogen bonding were calculated using the program PROPKA 2.0 (<http://propka.ki.ku.dk/>).

doi:10.1371/journal.pone.0069411.t003

B. anthracis, *B. mycoides*, *B. pseudomycoides*, *B. thuringiensis* and *B. weihenstephanensis*. It has been shown that BC3987 can function as an electron donor to class Ib RNR [30]. However, subsequent studies using the corresponding enzymes from *B. anthracis* showed that the BC3987 homolog is 6–7 times less effective than Trx1 in reducing RNR and that Trx1 is 60 fold abundant compared to the BC3987 homolog [31]. Thus, it is most likely that Trx1 is the *in vivo* electron donor to class Ib RNR in both *B. anthracis* and *B. cereus*.

The protein showing the highest amino acid identity (37%) to BC3987 does not belong to a member of the *Bacillus* genus, but is a small Trx (NT01CX_2375) found in the anaerobe *C. novyi*. This protein has 58% sequence identity with the *C. pasteurianum* thioredoxin Cp9 that is encoded in an operon between a NADH dependent TrxR and a Prx (Figure 6A), functioning as an electron transporter between these two proteins [29]. The NT01CX_2375 gene is found in an identical operon structure as Cp9 with flanking TrxR and Prx. These three proteins have been found to be present at relatively high levels in *C. novyi* spores [65]. *B. cereus* ATCC 14579 has a gene (BC2114) encoding a protein that has 54% sequence identity to the *C. novyi* Prx, however, this gene is not collocated with any TrxR or Trx genes. Thus, one possible substrate for BC3987 is the putative Prx BC2114. Aside, it should be mentioned that several non-bacterial Prxs with ~50% sequence identity to BC2114 have been characterized, and that some of them are reduced by redoxins with C-P-P-C active site motifs as found in BC3987 [66,67].

In order to relate BC3987 to the Cp9-redoxins found in *C. pasteurianum/novyi* and NrdH-redoxins, a phylogenetic analysis of a collection of sequences representing these proteins were carried out. The tree shown in Figure 2 indicates that the BC3987 homologs found among the members in the *Bacillus cereus* group form a separate cluster from the NrdH-redoxins and the proteins homologous to the *C. pasteurianum/novyi* Cp9 thioredoxin. A

A. *C. pasteurianum* (and *novyi*) Peroxiredoxin operon



B. Typical class Ib RNR *nrdHIEF* operon



C. *B. cereus* group class Ib RNR *nrdIEF* operon

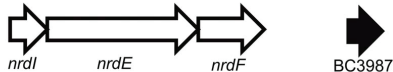


Figure 6. Overview of operon organization of Cp9-redoxins, NrdH-redoxins, and BC3987. (A) The gene encoding the Cp9-redoxin is located between a thioredoxin reductase (cp34) and a peroxiredoxin (cp20). (B) The classical class Ib RNR operon where the NrdH-redoxin is found in front of the genes encoding the flavodoxin-like protein NrdI, the catalytic subunit NrdE and the radical/metal cofactor containing NrdF protein. (C) The organization of class Ib RNR genes in the *Bacillus cereus* group where the putative NrdH-redoxin (BC3987) is located elsewhere in the genome. doi:10.1371/journal.pone.0069411.g006

slightly shorter evolutionary distance is observed between the clusters represented by BC3987 and the *C. pasteurianum/novyi* Cp9 compared to that formed by NrdH-redoxins. The amino acid deletion at position 44 in the NrdH-redoxins was not taken into account while performing the phylogenetic analysis, thus, this deletion increase the evolutionary distance of the NrdH-redoxins to the other two groups further. The role of BC3987 as a part of Prx-mediated defense against reactive oxygen species in *B. cereus* is currently investigated in our laboratory.

The only two cysteine residues in the protein are found in the active site, and the observation that the change in the molar extinction coefficient $\Delta\epsilon_{240\text{ nm}}$ was about twice of the expected value for one thiol/thiolate pair indicate that both active site cysteines have lowered pK_a values. Similar observations have been made for the *B. subtilis* thiol-disulfide oxidoreductases ResA and StoA where a water molecule bound to a Glu residue can hydrogen bond to the C-terminal buried cysteine and lower its pK_a value [68,69]. The mechanism for lowered thiol pK_a values in C-x-x-C active sites involved in redox chemistry is discussed below.

In Figure 3 it is shown that the C-x-x-C motifs among established and putative Trxs have substantial variation. The typical Trx active site motif is C-G-P-C as seen in Table 1 where a large number of thioredoxin superfamily members have been analyzed and compared, also including the six amino acids preceding the C-x-x-C motif.

About 92% of the typical Trxs included in the survey have an acidic Asp or Glu residue in the sixth position preceding the C-G-P-C motif, and it has been proposed that this residue acts as a general acid/base catalyst for proton transfer during reduction and oxidation of the disulfide bridge [22]. For *E. coli* Trx, this residue, which is located 5.6 Å away from the buried C-terminal active site cysteine, has been demonstrated to be essential for catalytic efficiency [21]. It has also been suggested that a Ser or Thr residue four residues in front of the C-x-x-C motif, [ST]-x(3)-C-x(2)-C, influence Trx activity by interacting directly with the previously discussed Asp residue [70] or the buried Cys residue [71]. Yet, less than 5% of the C-G-P-C type Trxs included in our survey has a Ser or Thr residue in this position (Table 1), indicating that such an arrangement is not a general feature for this type of Trxs. None of the Grxs or NrdH-redoxins have an Asp or Glu in the sixth position. However, the [ST]-x(3)-C-x(2)-C motif is observed in 60 and 99.5% of Grxs and NrdH-redoxins (Table 1), respectively. As we have shown in this work, mutation of the Thr8 residue in the fourth position preceding the C-P-P-C motif decrease the catalytic efficiency of the enzyme (Figure 2).

In the structures of the oxidized NrdH-redoxins from *E. coli* and *C. ammoniagenes* the hydroxyl O-atom of the Thr residue in T-x(3)-C-V-Q-C motif is oriented towards the buried Cys-S_γ with distances of 3.4 and 3.8 Å, both being potential hydrogen bonding partners with the cysteine thiol/thiolate when the active sites are in their reduced states.

In BC3987, which has a ⁶V-Y-T-Q-P-D-C-P-P-C¹⁵ motif, Thr8 is a potential hydrogen bond donor to Cys15-S_γ. However, in the BC3987 crystal structure the side chain of this residue is hydrogen bonded to a water molecule resulting in a rotamer where the Thr hydroxyl group points away from the buried Cys15 as shown in Figure 3A, different from what observed in the *E. coli* and *C. ammoniagenes* NrdH-redoxins. Considering the similarity of the Thr8 environment with those of Thr7 in the *E. coli* and *C. ammoniagenes* NrdH-redoxins, a low energy barrier between the two rotamers seems likely. In addition, the Thr53 residue, not conserved within the NrdH and Cp9-redoxin families, was found in the vicinity of the active site. Thus, there are two potential

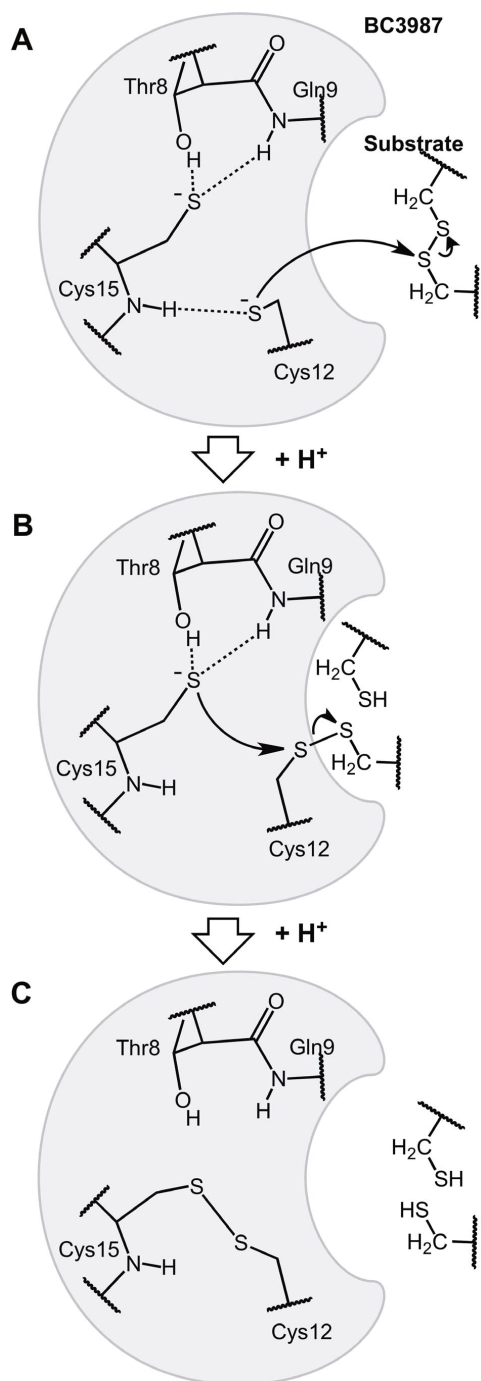


Figure 7. A possible substrate reduction reaction mechanism for BC3987 based on Model II involving two active site thiolates. (A) The reaction is initiated by a nucleophilic attack on the substrate disulfide bridge by the Cys12 thiolate and a mixed disulfide intermediate is formed. (B) The buried Cys15 S_γ-atom that is stabilized in its thiolate form by hydrogen bonding to Thr8 and Gln9 perform a second nucleophilic attack on the Cys12 S_γ-atom. (C) The reduced substrate is released and the two active site cysteines in BC3987 form a disulfide bridge.

doi:10.1371/journal.pone.0069411.g007

hydrogen bond donors to the Cys15 S_γ-atom in addition to the Gln9 amide protein.

The modeling studies of the reduced active site provided information on its possible hydrogen bond arrangements. Two models were examined using QM/MM calculations, one where Thr8 had the rotamer present in the BC3987 crystal structure (Model I, Figure 5B) and one where the Thr8 side chain had been rotated to resemble the conformation found in *E. coli* and *C. ammoniagenes* NrdH-redoxins (Model II, Figure 5C). The experimentally observed lowered pK_a values for the buried cysteine thiol, can be explained through hydrogen bonding from the Gln9 amide protein and the Thr8 side chain. Showing that the *E. coli* and *C. ammoniagenes* NrdH-redoxin Thr8 rotamer is capable to form a hydrogen bond to the buried cysteine has important implications for all Trxs having the [ST]-x(3)-C-x-x-C motif. Such an interaction can result in a stabilization of the buried cysteine thiolate in the active site at physiological pH values, making a simple reaction mechanism like the one presented in Figure 7 plausible. In this mechanism, the initial nucleophilic attack is carried out by the solvent exposed Cys12 that is stabilized in its deprotonated thiolate form due to hydrogen bonding to the Cys15 amide protein (Figure 7A). This primary activation of the nucleophilic cysteine could be general to all Trxs. To break the resulting mixed disulfide intermediate the buried Cys15 needs to be deprotonated to perform the second nucleophilic attack. We suggest that Cys15 is already in its deprotonated form, stabilized by hydrogen bonding to Thr8 and Gln9 (Figure 7B). Thus, this mechanism offers an elegant explanation of the deprotonation of the buried cysteine in Trxs that lack an analog to the Asp26 residue in *E. coli* Trx.

In summary it has been shown that BC3987 appears to be a closer relative to Trxs that reduce peroxiredoxins than NrdH-redoxins that provide electrons to the catalytic subunit of class Ib ribonucleotide reductases. The observation that the reduced form of BC3987 seems to possess two cysteine residues in the active site with lowered pK_a values have been explained through intra-protein hydrogen bonding patterns. Disturbing the hydrogen bonding networks by removing a highly conserved Thr residue near the buried Cys resulted in decreased efficiency for the BC3987 thioredoxin.

Supporting Information

Figure S1 Multiple alignment of amino acid sequences of NrdH-redoxins (in red), Cp9/NT01CX_2375 homologs (in green), and BC3987 homologs (in blue). The columns containing the conserved Thr/Ser residues in position 8, and the gaps in the NrdH-redoxin sequences in position 44, are marked with arrows and with orange background. (PDF)

Acknowledgments

We would like to thank Dr. Hans-Peter Hersleth and Dr. Camilla Oppegård for valuable discussions. We are also grateful to Professor

53. Frisch MJ, Trucks GW, Schlegel HB, Scuseria GE, Robb MA, et al. (2004) Gaussian 03 D0.2. Gaussian, Inc.
54. Wang JM, Wang W, Kollman PA, Case DA (2006) Automatic atom type and bond type perception in molecular mechanical calculations. *JMolGraphics Modell* 25: 247–260.
55. Stehr M, Schneider G, Aslund F, Holmgren A, Lindqvist Y (2001) Structural basis for the thioredoxin-like activity profile of the glutaredoxin-like NrdH-redoxin from *Escherichia coli*. *Journal of Biological Chemistry* 276: 35836–35841.
56. Rappe AK, Goddard WA (1991) Charge Equilibration for Molecular-Dynamics Simulations. *Journal of Physical Chemistry* 95: 3358–3363.
57. Benesch RE, Lardy HA, Benesch R (1955) The Sulfhydryl Groups of Crystalline Proteins. I. Some Albumins, Enzymes, and Hemoglobins. *Journal of Biological Chemistry* 216: 663–676.
58. Polgar L (1974) Spectrophotometric Determination of Mercaptide Ion, An Activated Form of Sh-Group in Thiol Enzymes. *Febs Letters* 38: 187–190.
59. Witt AC, Lakshminarasimhan M, Remington BC, Hasim S, Pozharski E, et al. (2008) Cysteine pK_a depression by a protonated glutamic acid in human DJ-1. *Biochemistry* 47: 7430–7440.
60. Whelan S, Goldman N (2001) A general empirical model of protein evolution derived from multiple protein families using a maximum-likelihood approach. *Molecular Biology and Evolution* 18: 691–699.
61. Hurvich CM, Tsai CL (1989) Regression and Time-Series Model Selection in Small Samples. *Biometrika* 76: 297–307.
62. Sugiura N (1978) Further Analysis of Data by Akaike's Information Criterion and Finite Corrections. *CommunStatA-Theor* 7: 13–26.
63. Lennon BW, Williams CH, Ludwig ML (2000) Twists in catalysis: Alternating conformations of *Escherichia coli* thioredoxin reductase. *Science* 289: 1190–1194.
64. Ho BK, Coutsiaris EA, Seok C, Dill KA (2005) The flexibility in the proline ring couples to the protein backbone. *Protein Science* 14: 1011–1018.
65. Bettgeowda C, Huang X, Lin J, Cheong I, Kohli M, et al. (2006) The genome and transcriptomes of the anti-tumor agent *Clostridium novyi-NT*. *Nature Biotechnology* 24: 1573–1580.
66. Navrot N, Collin V, Gualberto J, Gelhaye E, Hirasawa M, et al. (2006) Plant glutathione peroxidases are functional peroxiredoxins distributed in several subcellular compartments and regulated during biotic and abiotic stresses. *Plant Physiology* 142: 1364–1379.
67. Nogoceke E, Gommel DU, Kiess M, Kalisz HM, Flohe L (1997) A unique cascade of oxidoreductases catalyses trypanothione-mediated peroxide metabolism in *Crithidia fasciculata*. *Biological Chemistry* 378: 827–836.
68. Lewin A, Crow A, Hodson CTC, Hederstedt L, Le Brun NE (2008) Effects of substitutions in the CXXC active-site motif of the extracytoplasmic thioredoxin ResA. *Biochemical Journal* 414: 81–91.
69. Crow A, Liu YM, Moller MC, Le Brun NE, Hederstedt L (2009) Structure and Functional Properties of *Bacillus subtilis* Endospore Biogenesis Factor StoA. *Journal of Biological Chemistry* 284: 10056–10066.
70. Qin J, Clore GM, Gronenborn AM (1996) Ionization equilibria for side-chain carboxyl groups in oxidized and reduced human thioredoxin and in the complex with its target peptide from the transcription factor NF kappa B. *Biochemistry* 35: 7–13.
71. Rickard GA, Berges J, Houce-Levin C, Rauk A (2008) Ab initio and QM/MM study of electron addition on the disulfide bond in thioredoxin. *Journal of Physical Chemistry B* 112: 5774–5787.

Figure S1

Tuning of Thioredoxin Redox Properties by Intramolecular Hydrogen Bonds

Åsmund Kjendseth Røhr, Marta Hammerstad, and K. Kristoffer Andersson

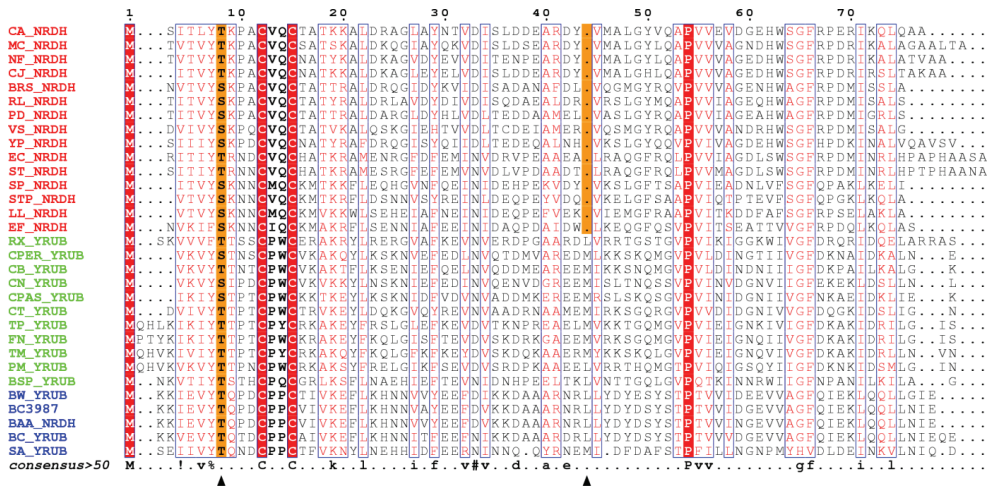


Figure S1. Multiple alignment of amino acid sequences of NrdH-redoxins (in red), Cp9/NT01CX_2375 homologs (in green), and BC3987 homologs (in blue). The columns containing the conserved Thr/ Ser residues in position 8, and the gaps in the NrdH-redoxin sequences in position 44, are marked with arrows and with orange background.

The corresponding species and accession numbers of the sequence names are as follows: CA_NRDH; *Corynebacterium ammoniagenes* (O69271), MC_NRDH; *Mycobacterium tuberculosis* (NP_217569), NF_NRDH; *Nocardia farcinica* (YP_120522), CJ_NRDH; *Corynebacterium jeikeium* (YP_250251), BRS_NRDH; *Brucella abortus* (YP_001932759), RL_NRDH; *Rhizobium leguminosarum* (YP_769836), PD_NRDH; *Paracoccus denitrificans* (YP_001607868), VS_NRDH; *Vibrio sp.* (ZP_01066345), YP_NRDH; *Yersinia pestis* (YP_001873486), EC_NRDH; *Escherichia coli* (ZP_03083809), ST_NRDH; *Salmonella enteric* (YP_002115761), SP_NRDH; *Streptococcus pyogenes* (NP_269480), STP_NRDH; *Streptococcus pneumoniae* (YP_002037786), LL_NRDH; *Lactococcus lactis* (YP_001032827), EF_NRDH; *Enterococcus faecalis* (NP_814257), RX_YRUB; *Rubrobacter xylanophilus* (YP_644383), CPER_YRUB; *Clostridium perfringens* (ZP_02953769), CB_YRUB; *Clostridium beijerinckii* (YP_001307271), CN_YRUB(NT01CX_2375); *Clostridium novyi* (YP_878448), CPAS_YRUB; *Clostridium pasteurianum* (P23171), CT_YRUB; *Clostridium thermocellum* (YP_001036667), TP_YRUB; *Thermotoga petrophila* (YP_001245300), FN_YRUB; *Fervidobacterium nodosum* (YP_001410364), TM_YRUB; *Thermosiphon melaniensis* (YP_001305804), PM_YRUB; *Petrotoga mobilis* (YP_001568453), BSP_YRUB; *Bacillus sp.* (ZP_01860678), BW_YRUB; *Bacillus weihenstephanensis* (YP_001646612), BC3987; *Bacillus cereus* (NP_833706), BAA_NRDH; *Bacillus anthracis* (YP_030147), BC_YRUB; *Bacillus cereus* subsp. *Cytotoxicus* (YP_001375918), SA_YRUB; *Staphylococcus aureus* (YP_185957).

Correction: Tuning of Thioredoxin Redox Properties by Intramolecular Hydrogen Bonds

Åsmund Kjendseth Røhr, Marta Hammerstad, K. Kristoffer Andersson

Published: August 06, 2013 • DOI: [10.1371/annotation/2e2b21bd-bbf7-4a4b-a9cf-194b693e02bf](https://doi.org/10.1371/annotation/2e2b21bd-bbf7-4a4b-a9cf-194b693e02bf)

Figures 1 and 2 were accidentally switched. The image appearing as Figure 1 belongs with the title and legend for Figure 2, and the image appearing as Figure 2 belongs with the title and legend for Figure 1. The titles and legends are in correct order.

